2005

INVESTIGATION of CURRENT TRANSPORT IN ITO/CdTe/polymer/Al DEVICES USING NANO-STRUCTURED CdTe

Vignesh Ramachandran
University of Kentucky, vignesh4u@yahoo.com

Recommended Citation

Ramachandran, Vignesh, "INVESTIGATION of CURRENT TRANSPORT IN ITO/CdTe/polymer/Al DEVICES USING NANO-STRUCTURED CdTe" (2005). *University of Kentucky Master's Theses*. 255.
https://uknowledge.uky.edu/gradschool_theses/255

ABSTRACT OF THESIS

INVESTIGATION of CURRENT TRANSPORT IN ITO/CdTe/polymer/Al DEVICES USING NANO-STRUCTURED CdTe

In this thesis, photo luminescent diodes with the device structure of ITO/PEI/(CdTe/PDDA)*n/Al were fabricated using the method of layer-by-layer self assembly. The film thicknesses were varied from 150 nm to 380 nm. The films were characterized through X-ray diffraction (XRD), optical absorption and photoluminescence (PL) measurements. The XRD results on the film indicated a cubic crystalline structure (111) for the nano-CdTe particles. The band gap of the nano-particles were evaluated to be 2.1 eV in solution and 2 eV in films, which was further confirmed by the PL measurements as the solution exhibited a yellow luminescence while the film exhibited orange luminescence. The J vs. V curves revealed that the diodes exhibited rectifying behavior in both the forward and reverse biasing. Two models of current transport, one based on a Schottky mechanism and the other based on a tunneling mechanism were developed and were compared with the experimental values. The tunneling model developed could simulate the experimental currents up to four orders of magnitude. The tunneling mechanism of charge transport was further proved by the capacitance vs. voltage curves, which were identical to that of ITO/MEH-PPV/Al devices, where tunneling mechanism was the dominant method of charge transport.

KEYWORDS: CdTe, Charge Transport, Zener, Diodes, Tunneling, Nano-particles

Vignesh Ramachandran
February 9 2005

INVESTIGATION of CURRENT TRANSPORT IN ITO/CdTe/polymer/Al DEVICES USING NANO-STRUCTURED CdTe

By

Vignesh Ramachandran

Dr. Vijay P. Singh
(Director of Thesis)

Dr. Yu Ming Zhang
(Director of Graduate Studies)

February 9, 2005

RULES FOR THE USE OF THESES

Name	Date

THESIS

Vignesh Ramachandran

The Graduate School

University of Kentucky

2005

INVESTIGATION of CURRENT TRANSPORT IN ITO/CdTe/polymer/Al DEVICES USING NANO-STRUCTURED CdTe

---

THESIS

A thesis submitted in partial fulfillment of the requirements for the degree of
Master of Science in the College of Engineering
at the University of Kentucky

By

Vignesh Ramachandran

Lexington, Kentucky

Director: Dr. Vijay P. Singh, Professor and Chair

Electrical and Computer Engineering

2005

MASTER'S THESIS RELEASE

I authorize the University of Kentucky Libraries
to reproduce this thesis in
whole or in part for purposes of research.

Signed: ________________________________

Date: ________________________________

ACKNOWLEDGEMENTS

Thanks are due to a number of people who have provided invaluable help in my three year journey through the graduate school. First of all, my sincere thanks and heartfelt gratitude to my academic advisor and thesis director Dr. Vijay P. Singh for his guidance and support through out my thesis work. I am really thankful to him for continually supporting my work and providing a stimulating environment to learn science. I would like to extend my thanks to Dr. Janet K. Lumpp and Dr. Arthur V. Radun for serving on my thesis committee and providing me with invaluable comments and suggestions for improving this thesis. The contributions from the post docs, Dr. Alberto Aguilera for modeling the device and Dr. Suresh S. Rajaputra for material characterization, have been a major factor in completion of this thesis. I would also extend my gratitude and appreciation for all the student members of Dr. Singh's group, who have contributed to my thesis in one way or the other.

I am greatly indebted to the invaluable and timely help provided by Dr. Nicholas A. Kotov of University of Michigan, Ann-Arbor, who provided me with the nano-CdTe particles, without which this thesis wouldn't have come into existence. Last but not the least; I would like to express my deepest gratitude and thanks to my parents for their support and belief in me all these years.

TABLE OF CONTENTS

ACKNOWLEDGEMENTS iii
List of Tables vii
List of Figures viii
List of Files xi
1. Introduction 1
2. Theory 3
  2.1 Semiconductor Nano-crystals or Quantum Dots 3
  2.2 Quantum Confinement 3
  2.3 Capped and Uncapped Nano-particles 6
  2.4 Layer-by-Layer Assembly of Nano-particles: An Introduction 8
  2.5 Advantages of the L-B-L Techniques 11
  2.6 Metal Semiconductor Interface 11
  2.7 Energy Band Diagram of a Schottky Barrier 12
3. Experimental 15
  3.1 Device Fabrication 15
    3.1 a. Device Structure 15
    3.1 b. Substrate Cleaning 16
    3.1 c. Fabrication of CdTe nano-crystals 17
    3.1 d. Fabrication of nano-crystalline CdTe films 18
    3.1 e. Back Side Etching 19
    3.1 f Deposition of aluminum contacts 20
  3.2 X-Ray Diffraction (XRD) 21
  3.3 Optical Absorption and Photoluminescence 22
  3.4 I-V Measurement Setup 24
  3.5 Capacitance Measurements 24
4. Material and Optical Characterization 25
  4.1 XRD 25
  4.2 Thickness Characterization 27
  Table 4.1 Effect of number of bilayers on thickness of the film 27
  4.3 Optical Characterization 28

4.31 Optical Absorption of nano-CdTe II solution 28
4.32 Optical absorption of (CdTe/PDDA) films 30
4.33 Variation in absorbance with thickness of the film.. 31
4.34 Determination of Band Gap from absorption characteristics of solution 32
4.35 Determination of Band Gap from absorption characteristics of films 34
4.36 Photoluminescence Measurement.. 36
4.36 a. Analysis of Phosphorescence from the film and solution 36
4.36 b. Measurement of PL spectrum 38
5. Electrical Characterization 40
5.1 J-V Characteristics 40
5.11 Device Structure ITO/ CdTe I / Al.. 40
5.12 Device Structure ITO/PEI/(CdTe I /PDDA)*10/Al.. 41
5.13 Effect of concentration of the organic polycations on the J-V curves of Uncapped CdTe thin film devices. 42
5.14 Effect of number of bilayers on Uncapped CdTe thin film devices. 43
5.2 J-V Analysis for thiol Capped CdTe Devices 45
5.21 Forward Current Analysis of thiol capped devices 45
5.22 Effect of Number of Bilayers on Forward Current 46
5.23 Effect of Time on Forward Current 48
5.24 Effect of UV light on Forward Current... 49
5.25 Reverse Current Analysis of thiol capped devices.. 50
5.26 Effect of number of bilayers for reverse current.. 51
5.27 Effect of UV Light on Reverse Current 53
5.3 Modeling the electron transport mechanism in the device 54
5.31 A Schottky Model for current – voltage mechanism 54
5.32 Calculation of Barrier Potential from the Schottky Model...................................... 61
5.33 Validity of the Schottky model 62
5.34 Energy Band Diagram based on the Schottky model 63
5.35 Limitations of the Schottky Model 64
5.36 A new Model based on “Tunneling” mechanism 65
5.37 Verifying Tunneling in the device 66
5.38 Simulating the current density using the tunneling model....................................... 69

5.39 Tunneling Model -Validity 76
5.40 Energy Band Diagram based on the Tunneling model 76
5.41 Analysis of Capacitance vs. Frequency 78
5.42 Analysis of Capacitance vs. Voltage.. 80
6. Conclusions.. 83
References:... 85
Vita.. 91

List of Tables

Table 4.1 Effect of number of bilayers on thickness of the film………………………. (28)

List of Figures

Figure 2. 1: Quantum Confinement, Graphic representation of bulk material (3 degrees of freedom), a 2D Quantum well (2 degrees of freedom), a 1D Quantum wire (1 degree of freedom), and a 0D quantum dot (0 degrees of freedom). Also included is the corresponding density of states for each system. 5

Figure 2. 2 Uncapped Nano-particle 6

Figure 2. 3 Capped Nano-particle (Here the blue color is CdTe and Purple color is thiol) 7

Figure 2. 4 Schematic Representation of LBL deposition cycle 1 and 3 – deposition of oppositely charged species from their aqueous solutions, 2 and 4- rinsing with DI water, 5 – repetition of dipping cycle. 8

Figure 2. 5 Schematic representation of the electrostatic LBL assembly for nano-particles and nano-platelets [16]. 10

Figure 2. 6 Band diagram of metal and n-type semiconductor before contact. 12

Figure 2. 7 Band Diagram of a metal-semiconductor after contact (at equilibrium). 13

Figure 3. 1 First Device Structure: ITO/CdTe I/ Al 15

Figure 3. 2 Device Structure ITO/PEI/(CdTe II/ PDDA)*2/Al 16

Figure 3. 3 Principal sketch of the structure of the CdTe particles (not scaled) for film preparation. 17

Figure 3. 4 A simple setup for the Layer-by-Layer method of deposition 19

Figure 3. 5 Absorption of photons with hυ>E_g 22

Figure 3. 6 Block diagram of the UV-Vis Spectrophotometer 23

Figure 3. 7 Excitation and recombination mechanisms in PL with a trap level for electrons. 23

Figure 3. 8 Circuit Diagram for the I-V measurements 24

Figure 4. 1 X-Ray diffraction patterns on a 12 bilayer film of (CdTe II and PDDA) 25

Figure 4. 2 X-Ray diffraction patterns on a 23 bilayer film of (CdTe II and PDDA) 26

Figure 4. 3 Effect of thickness on the number of bilayers 27

Figure 4. 4 Optical absorption for thiol capped CdTe solution 28

Figure 4. 5 Absorption characteristics as a function of Energy 29

Figure 4. 6 Absorption of a film with 12 bilayers of CdTe/PDDA 30

Figure 4. 7 Absorption characteristics as a function of Energy 31

Figure 4. 8 Absorbance of films with thickness of 92 nm, 130 nm, and 180 nm respectively32

Figure 4. 9 Calculation of band gap from solution 34

Figure 4. 10 Determination of Band gap using Tauc's Law 36

Figure 4. 11 Phosphorescence of (a.) film (b.) solution under the influence of a 365nm light source. 37

Figure 4. 12 Wavelength and frequency spectrum of visible light 38

Figure 4. 13 PL spectrum of CdTe solution for an excitation wavelength of 1. 365 nm and 2. 412 nm. 39

Figure 5. 1 J-V curves for the device structure ITO/CdTe I/Al 40

Figure 5. 2 J-V curves for the device structure ITO/PEI/(CdTe I /PDDA)*10/Al 42

Figure 5. 3 J-V curves for the device structure ITO/PEI/(CdTe I /PDDA)*10/Al, when the concentration of the organic polycations were reduced to 1 mg/ml. 43

Figure 5. 4 J-V curves for the device structure ITO/PEI/(CdTe I /PDDA)*15/Al 44

Figure 5. 5 J-V curves for the device structure ITO/PEI/(CdTe II /PDDA)*12/Al 45

Figure 5. 6 J-V curves for 12, 9 and 23 bilayer devices 46

Figure 5. 7 Current Density vs. Electric Field for 23, 12 and 9 bilayer devices 47

Figure 5. 8 Effect of time on Current Density (J in mA/cm^2) for a 12 bilayer device 48

Figure 5. 9 Effect of UV light on forward current 49

Figure 5. 10 Reverse current characteristics of ITO/PEI/(CdTe II /PDDA)*9/Al 50

Figure 5. 11 Effect of bilayers on reverse current as function of voltage, where 1 represents a device with 9 bilayers of CdTe and PDDA, 2 with 12 bilayers of CdTe and PDDA and 3 with 23 bilayers of CdTe and PDDA 51

Figure 5. 12 Effect of bilayers on reverse current as function of electric field, where 1 represents a device with 9 bilayers, 2 with 12 bilayers and 3 with 23 bilayers 52

Figure 5. 13 Effect of UV light on reverse current 53

Figure 5. 14 ln(J) vs. V for device with 12 bilayers 56

Figure 5. 15 Simulated & Experimental Current for a 12 bilayer device 58

Figure 5. 16 ln (J) vs. V for Reverse current 59

Figure 5. 17 Simulated and Experimental current density for Reverse bias........................... 60

Figure 5. 18 Back-to-Back Schottky diodes with shunt resistances 62

Figure 5. 19 (a) Energy band diagram of Al and CdTeII before contact, (b) after contact at equilibrium 63

Figure 5. 20 Verifying F-N tunneling mechanism for forward current 67

Figure 5. 21 Verifying F-N tunneling mechanism for reverse current 68

Figure 5. 22 Simulated and experimental forward current density, 1.Experimental current density 2.Tunneling component of simulated current and 3. Tunneling and resistive component of simulated current.. 70

Figure 5. 23 Simulated and experimental reverse current, 1. Experimental current density 2. Tunneling component of simulated current, and 3. Tunneling and resistive component of simulated current 72

Figure 5. 24 Simulated and experimental forward current density, 1. Experimental current density and 2. Tunneling + Schottky component of simulated current 74

Figure 5. 25 Simulated and experimental reverse current density... 75

Figure 5.26 Back-to-back Zener diodes with shunt resistances……………………………...77

Figure 5. 27 Energy band diagram for forward voltage – tunneling model 77

Figure 5. 28 Variation of 1. Capacitance as a function of frequency and.............................. 78

Figure 5. 29 Capacitance as a function of frequency, 1. Experimental Capacitance and 2. Simulated Capacitance.. 79

Figure 5. 30 Conductance as a function of frequency 1. Experimental and 2. Simulated...... 80

Figure 5. 31 Measured Capacitance as a function of voltage 81

Figure 5. 32 Conductance vs. voltage at 1. 1kHz and 2. 100kHz... 82

List of Files

Thesis_Vignesh.pdf……………………………………………………………….1.7MB

1. Introduction

Fabricating ultra thin films using a nano-semiconductor and organic polymer through simple techniques like spin-coating [1], Langmuir-Blodgett [2] and self-assembly [3] have acquired great interests over the last few years, primarily due to the simplicity of fabrication and the high quantum yield of the devices. The simplest method among the above mentioned methods is fabrication of diodes using the “Layer-by-Layer” (LBL) method of self assembly, which became popular through the work of G.Decher [9]. A number of semiconductor nano-particles namely cadmium selenide (CdSe), cadmium telluride (CdTe) and cadmium Sulfide (CdS) are being extensively used in display devices because of their optoelectronic properties. The availability of appropriate polyelectrolytes has opened the door to the construction of a new class of display devices including a multicolor pixel voltage-controllable light-emitting diode [4].

Currently light emitting diodes have been fabricated using nano-particles of CdTe [4], CdSe [2] along with organic polymers like poly (p-phenylenevinylene) (PPV) [4], polyvinylcarbazole (PVK) [2], polyethylenimine (PEI), polydiallyldimethyl ammonium chloride (PDDA). Though a number of light emitting diodes were fabricated using nano-particles and the organic polymers, the mechanism of charge transport in these complex devices are still not clearly understood. So the investigation of current transport in one such device (ITO/PEI/(CdTe/PDDA)*n/Al) has been undertaken in this thesis work.

In this thesis CdTe/polymer photo luminescent thin film diodes were fabricates using the LBL technique and they were characterized through optical absorption and photo luminescent measurements. Two kinds of CdTe nano-particle namely capped and uncapped CdTe were used and their performance with respect to current and photoluminescence (PL) were compared. From the absorption and PL measurements, the band gap of the nano-particles in films and solution were evaluated. To better understand the charge transport mechanism in the device, effect of the number of bilayers, time, UV light on the forward and reverse currents were analyzed in detail. From the analysis on the forward and reverse current, two mathematical models, one based on schottky mechanism and the other based on tunneling mechanism was developed. The two models were compared with the actual measured values of current and a possible energy band diagram was developed. Then to further understand the device, impedance measurements as a function of frequency and voltage were also done and were studied in detail.

This document is divided into 6 chapters. The basic concepts of nanotechnology and schottky diodes are discussed in chapter 2. In Chapter 3 the fabrication methods and the characterization procedures are explained. Results are split into two chapters for convenience. Chapters 4 deals with the optical and material characterization while chapter 5 deals with electrical characterization. The conclusions are presented in chapter 6 and references are included at the end of the final chapter.

2. Theory

2.1 Semiconductor Nano-crystals or Quantum Dots

Semiconductor nano-crystals, otherwise known as Quantum Dots represent a class of materials intermediate between the molecular and bulk forms of matter [5]. When the dimensions of the material are smaller than the characteristic length of an electron - hole pair (the bulk exciton Bohr radius) the material exhibits quantum confinement of the electron and hole in all three dimensions. As a result the nano-crystals have discrete molecular like energy levels and the spacing between these levels increases as the particle size decreases.

The separation between the valence band maximum, or highest occupied molecular orbital (HOMO), and the conduction band minimum, or the lowest unoccupied molecular orbital (LUMO) decreases as the nano-crystal increase in size. This could be attributed to the fact that as the particles become larger, an increase in the delocalization of the electron and hole takes place and ultimately reaching the bulk energy separation (band gap energy for a bulk material) at relatively large sizes.

2.2 Quantum Confinement

Quantum confined systems can be defined as those systems in which one or more dimensions have been made intentionally small compared to the length-scale of the material. Quantum confined semiconductor structures have been well studied and the transition from classical to quantum mechanical regime can be clearly understood. For instance when a semiconductor is illuminated by a light of sufficient energy, an electron can be excited from the valence band into the conduction band, leaving behind a positively charged hole. In quantum confined semiconductors this electron–hole pair also referred to as an exciton, is physically confined into a region that is smaller than its characteristics length scale (i.e. the

Bohr exciton diameter). Depending on the geometry of the structure the exciton can be confined in one, two or all three dimensions (quantum wells, quantum wires and quantum dots respectively). Two dimensional quantum wells are structures that are extended in two dimensions, while the third dimension remains small (like a disk). When an electron-hole pair is excited, it feels a free lattice potential within the plane of the quantum well, but sees a quantum confined "particle in a box" potential in the third dimension. Along the confined direction, only certain wavelengths are allowed, so the energy levels in this dimension are quantized. Consequently quantum wells have a distinctly different density of states than what is found in the bulk material.

This is illustrated in figure 2.1 where the "density of states vs. energy" is plotted for quantum wells, wires and dots. Density of states can be defined as the number of available states per unit energy per unit volume.

Quantum dots, the zero dimensional analogues of quantum wells, are the ultimate examples of quantum confinement systems. In these structures, the electron and hole see a "particle in a box" potential in all three dimensions. Theoretical studies reveal that quantum confinement in all three dimensions leads to a collapse of the bulk band structure into discrete, atomic like states [Figure 2.1]. As a result the quantum dots are also referred to as "artificial atoms". [6]

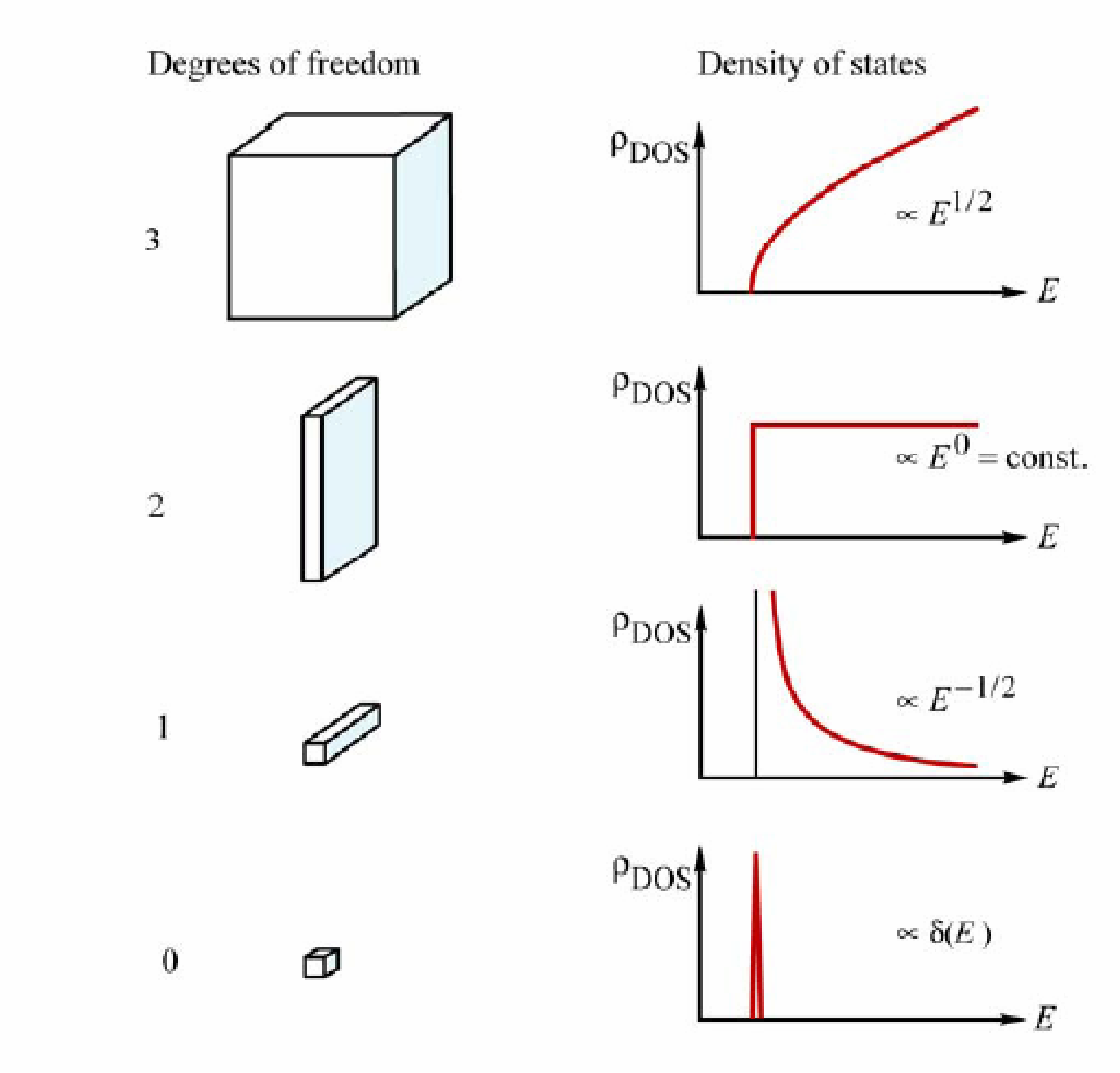

Figure 2. 1: Quantum Confinement, Graphic representation of bulk material (3 degrees of freedom), a 2D Quantum well (2 degrees of freedom), a 1D Quantum wire (1 degree of freedom), and a 0D quantum dot (0 degrees of freedom). Also included is the corresponding density of states for each system.

2.3 Capped and Uncapped Nano-particles

Having seen the basics of nano-particles, it is essential to note the various kinds of nano-particles that are being used for the fabrication of thin films. Basically the nano-particles can be classified into two types, namely “uncapped” and “capped” nano-particles. [7]

1.) Uncapped Nano-particles: These are the nano-particles which are used as synthesized without any structural modification. They exhibit all the properties of a nano-particle including that of Quantum confinement. In general the uncapped nano-particles [Figure 2.2] do not have any surface charge associated with them. In some applications the surfaces of the nano-particle are modified so that the nano-particle has an associated surface charge with them, which is particularly useful in fabrication of light emitting diodes.

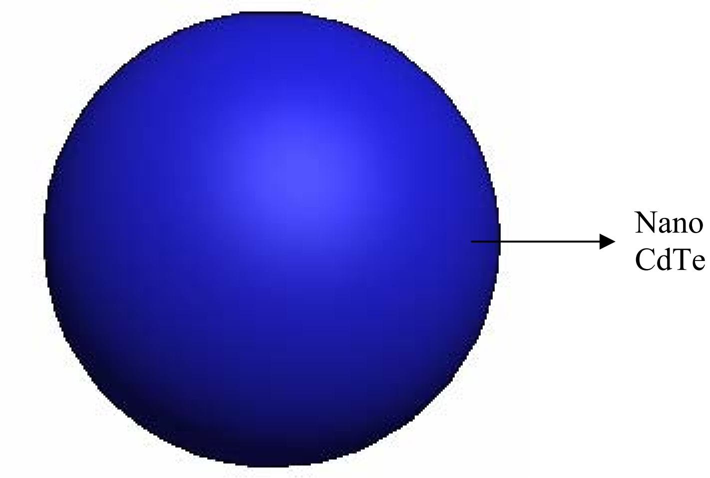

Figure 2. 2 Uncapped Nano-particle

2.) Capped Nano-particle: Controlled electronic passivation of the surface of an uncapped nano-particle by the formation of a core-shell over the nano-particle, leads to the formation of capped nano-particles. The core-shell material is a material with a much larger band gap than the nano-particle. The core-shell material can be another semiconductor material or an organic material. In this thesis the core-shell material used over CdTe is “thiol” [Figure 2.3].

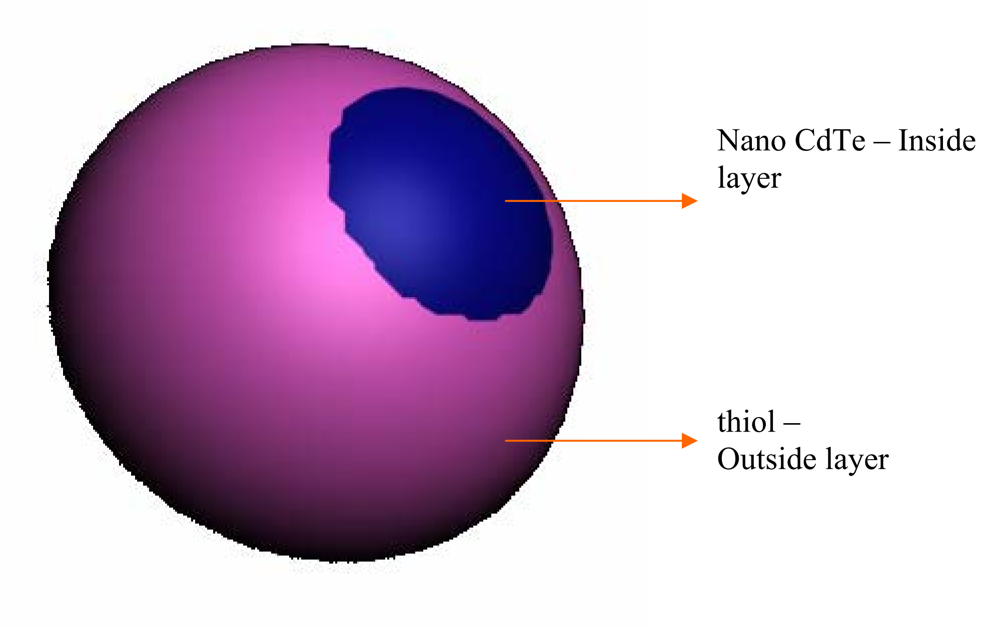

Figure 2. 3 Capped Nano-particle (Here the blue color is CdTe and Purple color is thiol)

The thiol layer over CdTe is formed through chemisorbtion. For the formation of thin films from a nano-particle (NP) and a Polyelectrolyte (PE), surface interactions between the NP and PE are particularly important. So a charged organic group is attached to NP. The hydrocarbon chain (thiol) will result in similar attraction to organic groups in the PE through hydrophobic interactions, while the surface charge will prevent irreversible coagulation of the NP colloid.

2.4 Layer-by-Layer Assembly of Nano-particles: An Introduction

Layer-by-layer (LBL) assembly can be described as the sequential adsorption of positively charged and negatively charged species, A and B, by dipping a substrate alternately into their solutions [8]. Rinsing with water between adsorption steps removes the excess of the previous solution thus leaving a thin layer of charged species on the surface, and thereby preparing the surface for the next adsorption step. This method of fabricating thin films was made popular by the work of Decher et. Al [9]. The substances A and B are chosen preferentially with high molecular weight, as from literature it can be seen that higher the molecular mass, more stable is the LBL growth. In this thesis A refers to CdTe nano-particles while B refers to PDDA a polyelectrolyte.

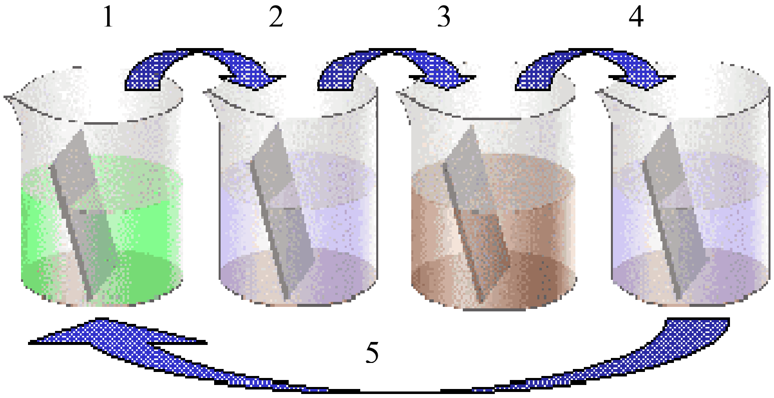

Figure 2. 4 Schematic Representation of LBL deposition cycle 1 and 3 – deposition of oppositely charged species from their aqueous solutions, 2 and 4- rinsing with DI water, 5 – repetition of dipping cycle.

Figure 2.4 shows the representation of the LBL deposition technique. In step 1 a well cleaned substrate like ITO is immersed in an aqueous colloidal solution of a charged species. Usually a charged polyelectrolyte (PDDA for instance has a positive charge at a pH of 6.0) [10] is used for the first step since it can cover a large area of substrate and can form a uniform distribution of charges on the substrate [7]. Once the first layer of deposition is complete, the substrate is rinsed with de-ionized water (DI) to remove the excess unadsorbed molecules [step 2]. Then it is transferred into an aqueous dispersion of an oppositely charged species (in our case nano CdTe has a negative charge) [step 3]. Finally, the substrate is rinsed with DI water [step 4]. This procedure is repeated until a film of desired thickness is obtained [step 5].

Some commonly used polyelectrolytes are PDDA, Polyaniline (PAni) [11], PPV (Polyphenylenevinylene) [12], and PEI (Polyethylenimine) while commonly used nanoparticles for light emitting devices are CdSe (cadmium selenide) [13], CdTe (cadmium telluride) [14] and CdS (cadmium Sulfide) [15]. The LBL principle of obtaining thin films can be used for the deposition of nano-particles as well as nano-platelets. This is illustrated in Figure 2.5. Interpenetration of the nano-particles and the polyelectrolyte are also observed in practice [8].

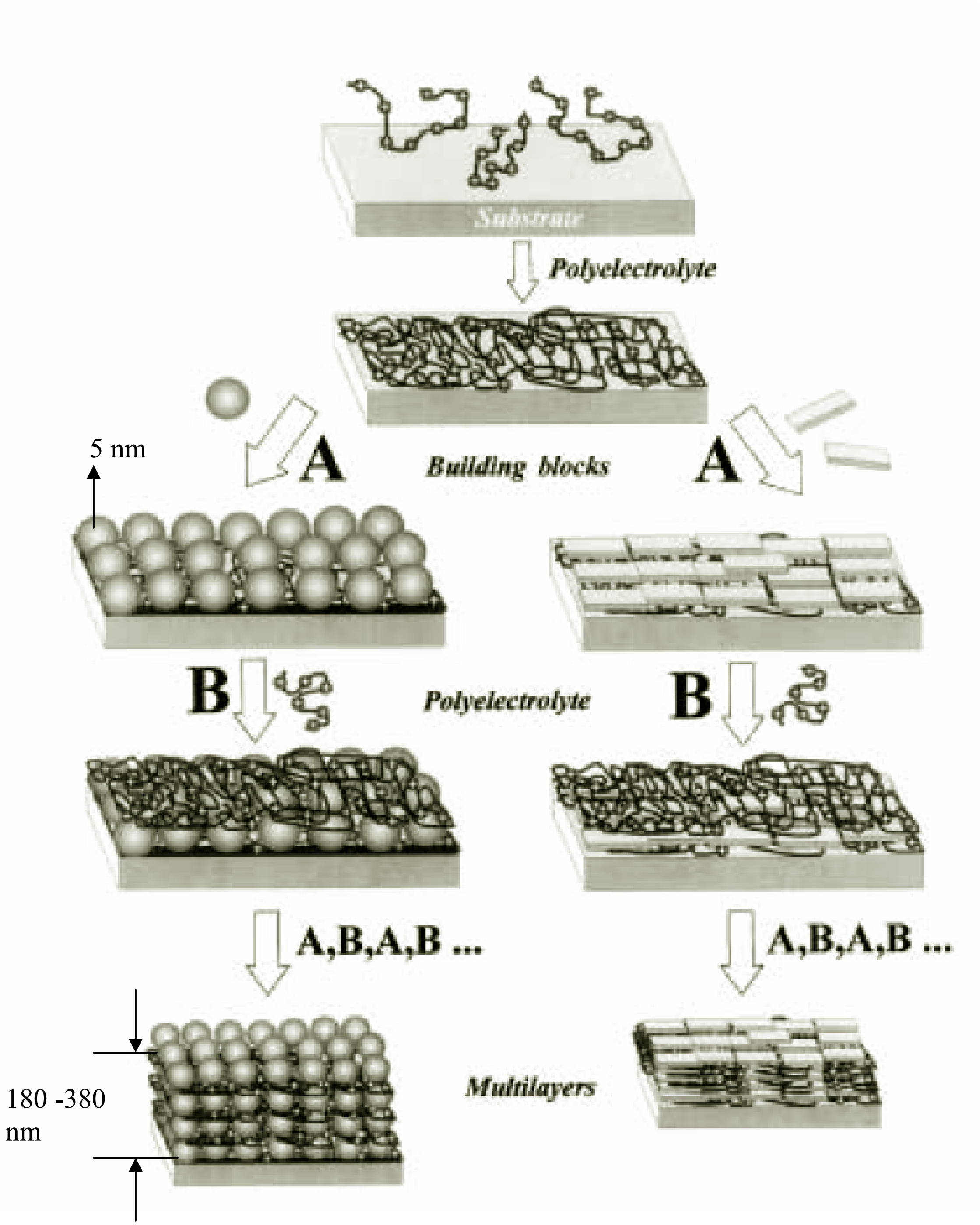

Figure 2. 5 Schematic representation of the electrostatic LBL assembly for nano-particles and nano-platelets [16].

2.5 Advantages of the L-B-L Techniques

Nano-particles (NP) of diameter 1-100 nm can be assembled with polyelectrolytes (PE) using the layer-by-layer (LBL) deposition protocols producing high quality thin films. The LBL assembly method has proven to be a simple and versatile method of multilayer preparation and is widely used for the composition of various complex materials. Since the process occurs in a layer-by-layer mode the control over the structure of the growing film is possible on each deposition step, thereby obtaining films with a high degree of structural organization. This is not achievable by traditional thin film deposition methods, such as sputtering, Langmuir-Blodgett, or spin-coating. Furthermore, self-assembly is economical (as dilute solutions and dispersions are used, and the materials can be recovered) and readily amenable to scaling-up for the fabrication of large-area, defect-free devices on virtually any shape and kind of surface [16].

2.6 Metal Semiconductor Interface

The analysis of a metal-semiconductor interface is essential for the understanding of the device structure that was fabricated. A metal-semiconductor (MS) contact can be classified into two categories namely “ohmic” contact and “rectifying” contact depending on the work function of the metal. If the metal work function (qΦm) is greater than that of the semiconductor (qΦs), then it forms a rectifying contact if the semiconductor is of n-type and an ohmic contact if the semiconductor is of p-type. Similarly, if the metal work function (qΦm) is less than the work function of a semiconductor (qΦs) forms a rectifying contact if the semiconductor is p-type and an ohmic contact if the semiconductor is n-type. The rectifying contacts have been used for various purposes including the fabrication of LEDs and fast switching circuits. Such rectifying contacts are also referred to as Schottky barrier diodes.

In our analysis of the device it was found that n-type CdTe formed rectifying contacts with aluminum (qΦm = 4.1 eV) and ITO (qΦs= 4.6 eV).

2.7 Energy Band Diagram of a Schottky Barrier

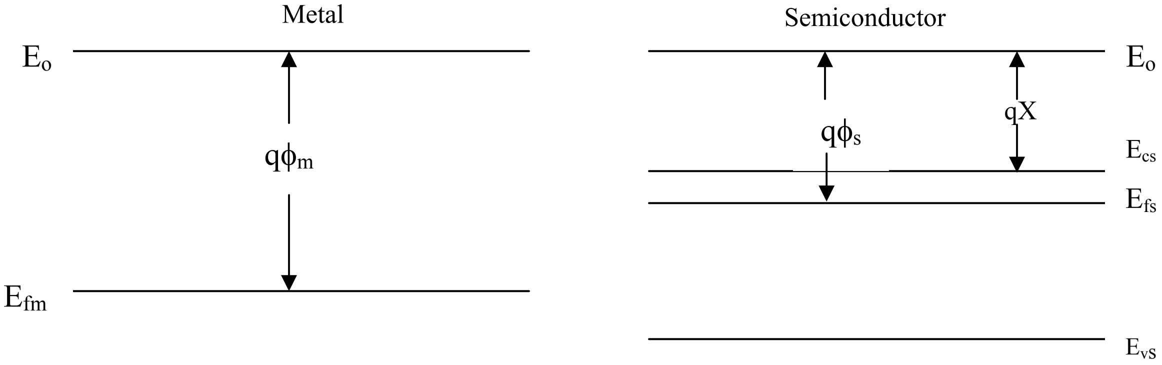

Figure 2. 6 Band diagram of metal and n-type semiconductor before contact.

E_o refers to vacuum potential

Efm the Fermi level for the metal

qΦm the metal work function

qΦs the semiconductor work function

$q\chi$ the electron affinity of semiconductor (measured from vacuum level to semiconductor conduction band edge)

Evs the valence band of the semiconductor

Ecs the conduction band of the semiconductor

Efs the Fermi level of the semiconductor

The figure shows the band gap for an n-type semiconductor and so the Fermi level is placed closed to the conduction band. When the metal and semiconductor are brought into an intimate contact, the electrons would diffuse from the semiconductor to the metal until the Fermi levels of both sides are aligned and the system reaches equilibrium. Now, as a result of this charge transfer, positive charge of width (w) is developed in the semiconductor and this charge is balanced by a sheet charge developed on the metal. This is similar to the depletion layer in the pn junctions [17, 18]. But in the case of Schottky diodes the effective depletion width will be the width of the depletion region in the semiconductor as the width of sheet charge in metal is negligible.

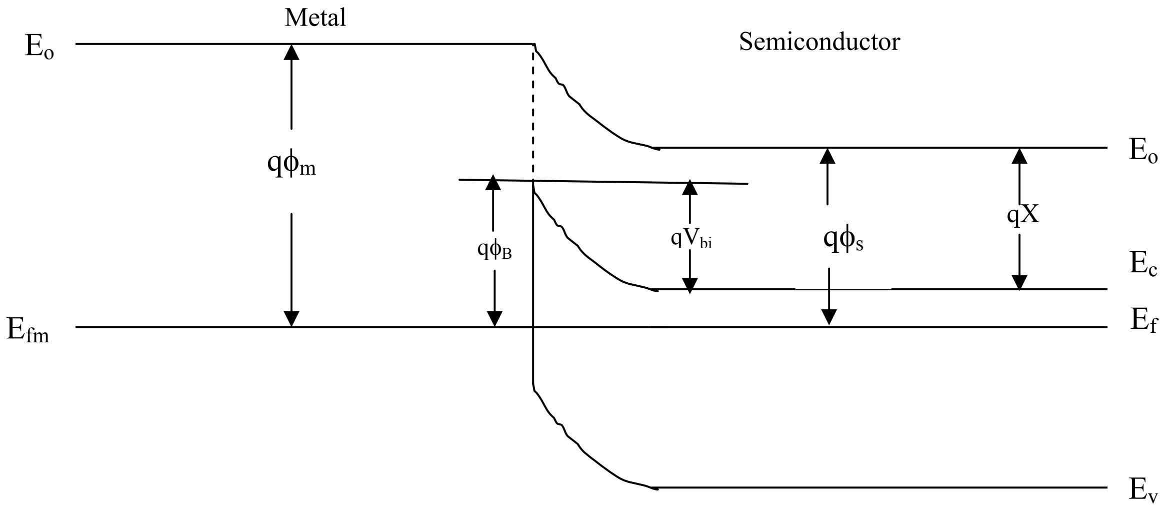

Figure 2. 7 Band Diagram of a metal-semiconductor after contact (at equilibrium).

When the metal and the semiconductor are brought in close contacts, a bending of energy bands takes place at the interface. This is illustrated in Figure 2.4. From Figure 2.3, it can be seen that the Fermi level of the metal (E_{fm}) is at a lower level than the semiconductor (E_{fs}). So, E_{fs} is at a higher potential than E_{fm}.

Efs	Efm	Charge Carriers
+	-	With respect to holes
-	+	With respect to electrons

Table 2.1 Determining the shape of Band - Bending

From table 2.1 E_{fm} is at a higher potential than E_{fs}, with respect to electrons. The flow of charges usually takes place from a higher to a lower potential, implying that the bending of bands will be from a higher to a lower potential (for electrons).

E_{fm}	E_{fs}	
-	+	(for holes)
+	-	(for electrons)

(Direction of band bending)

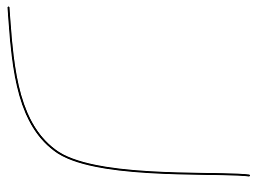

The charge exchange between semiconductor and metal will result in a field at the interface. The quantity qV_{bi} in figure 2.10 indicates the built-in potential and an electron can cross the barrier when it has a potential of V_{bi}. The term $q\phi_B$ represents the barrier height and is equal to $q(\phi_m\text{-}X)$

3. Experimental

3.1 Device Fabrication

3.1 a. Device Structure

Device structures with ITO/CdTe I/Al and ITO/PEI/(CdTe/PDDA)*n/Al were fabricated. The first structure could not be used in the fabrication of diodes as CdTe did not adhere to the ITO substrate, so the organic layers were introduced which increased the adhesion of CdTe to the surface [19, 20]. The two structures are shown below in Figure 3.1 and 3.2 respectively. Indium Tin Oxide (ITO) coated glass substrates were commercially purchased from Delta Technologies, Limited, Stillwater, MN-55082. Glass provides mechanical support to the devices while ITO, a transparent conductor serves as the bottom electrode.

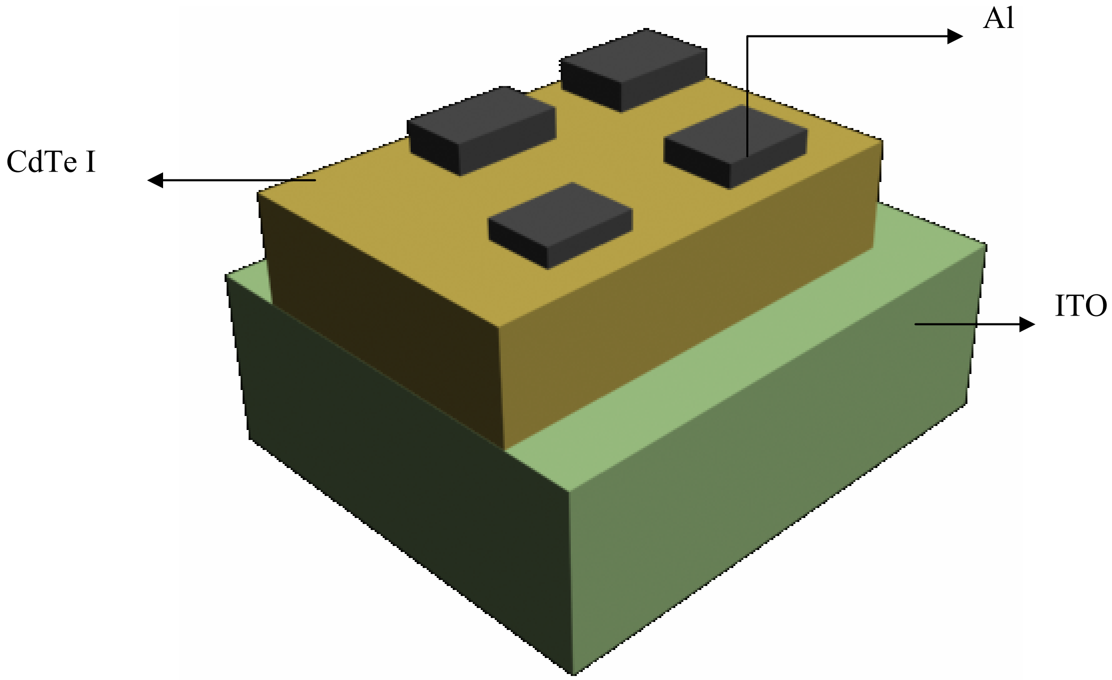

Figure 3. 1 First Device Structure: ITO/CdTe I/ Al

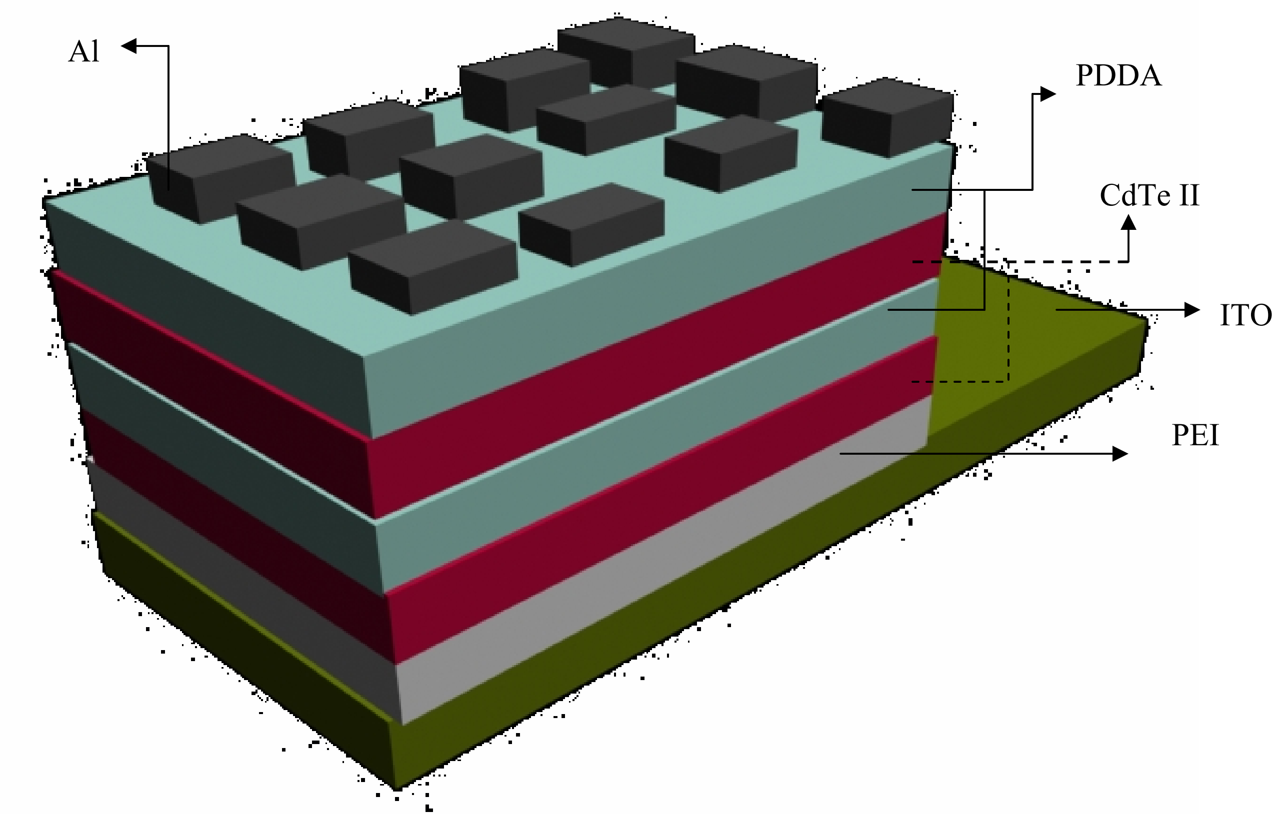

Figure 3. 2 Device Structure ITO/PEI/(CdTe II/ PDDA)*2/Al

The first set of devices were fabricated using uncapped CdTe nano-particles (CdTe I) while the second set of devices were fabricated using thiol-capped CdTe nano-particles referred to as CdTe II here. Fabrication procedures for the device structures mentioned are discussed in detail.

3.1 b. Substrate Cleaning

ITO was the substrate used in the fabrication of all our devices. For the Layer-By-Layer deposition method the ITO substrate had to be cleaned intensively as cleaning the substrate thoroughly makes it devoid of any impurities in the final film and the adsorption of the polyelectrolytes on to the substrate also increases significantly. So ITO was first cleaned twice in ethanol using an ultrasonic agitation system for a period of ten minutes. It was then immersed in a 1:1 mixture of ethanol and sulfuric acid at room temperature for one hour and then rinsed in ultra-pure water. This process leads to a development of a small negative charge on the ITO substrate [21]. Finally the samples were dried with flowing nitrogen.

3.1 c. Fabrication of CdTe nano-crystals

Nanocrystalline CdTe I was obtained from Tuskegee University, Alabama and nano-crystalline CdTe II was obtained from Dr. Kotov, University of Michigan, Ann Arbor.

The thiol capped CdTe particles are prepared in water solution by adding NaHTe solution to $(CdClO_4)_2.6H_2O$ solution saturated with N_2 in the presence of thioglycolic acid (HS–C–COOH). NaHTe is generated from the reaction of NaOH and H_2Te, which is obtained from the addition of Al_2Te_3 to HCl. Particles with a mean size of approximately 5 nm are obtained which consist of a CdTe core covered by a CdS shell due to the binding of the thiol groups to the Cd ions as shown in figure 3.3 [22]. The carboxyl groups of the thiolactic acid provide a negative surface charge density to the CdTe nano-particles.

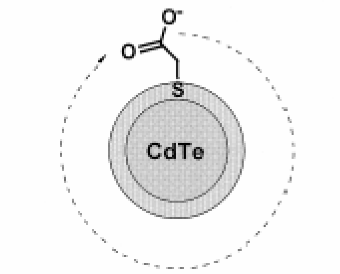

Figure 3. 3 Principal sketch of the structure of the CdTe particles (not scaled) for film preparation.

3.1 d. Fabrication of nano-crystalline CdTe films

The fabrication of CdTe films was based on the principle of layer-by-layer deposition technique discussed earlier in section 2.4. The organic polycations PEI and PDDA were purchased from Aldrich and dissolved in de-ionized water and the concentrations of the organic solutions used were reduced to 1 mg/ml. The molecular weights of the organics used were 750,000 for PEI and 200-350,000 for PDDA respectively. The CdTe II solution obtained from Dr. Kotov had a concentration of 10^{-05} M. It was further reduced to 10^{-07} M by diluting it with de-ionized water.

From the work of Rogach et al [23], it was found that the luminescence of the films improved when the solutions used for the deposition used were slightly acidic (i.e. pH ≈ 6.0). Consequently all the solutions used for deposition were maintained at a pH of 6.0 by using less than 100µL of 0.1 N hydrochloric acid.

The substrate after cleaning was dipped in a solution of PEI (pH=6) using the set up given below in figure 3.4. The substrate was left undisturbed for 20 minutes. A monolayer of polyelectrolyte (PEI) is assembled on the oppositely charged substrate (ITO) through ionic bonding, by dipping the substrate in the ionic solution. PEI was first deposited onto ITO substrate instead of PDDA, because of its greater adhesion to ITO. After rinsing this now coated substrate in ultra-pure water to remove the loosely adsorbed molecules, the substrate is then immersed in an oppositely charged CdTe II nano-particle solution to adsorb the next molecular monolayer. The resulting coated substrate is again rinsed in ultra-pure water [22]. Thus, one bilayer (cation/anion i.e. polycation/nano-particles) is synthesized. Then the same process was repeated with PDDA as the organic polycation as PDDA was a stronger polycation and the luminescence properties were enhanced with it [23]. Repeating this process, we get multilayer structures of desirable thickness.

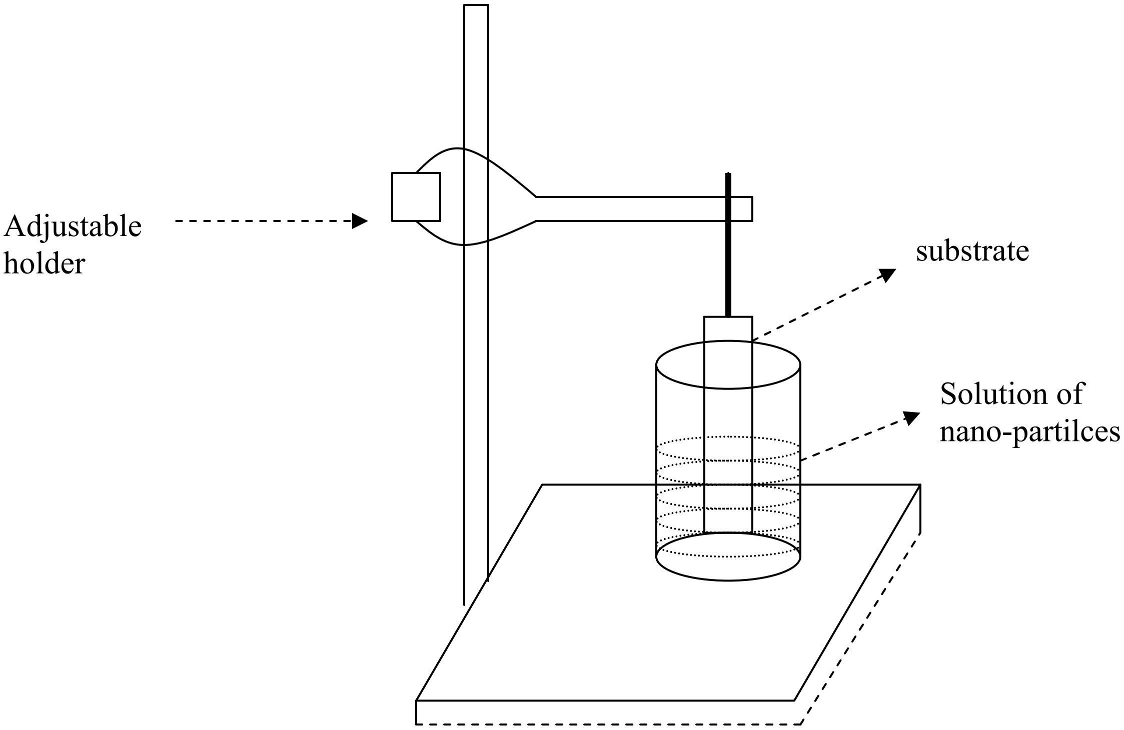

Figure 3. 4 A simple setup for the Layer-by-Layer method of deposition

The layer-by-layer assembly was done using the simple setup given above in figure 3.4. The height of the substrate in the solution could be adjusted by using the adjustable holder. After every deposition the solution was replaced with the corresponding complementary solution by easily removing the substrate from inside the container, by using the adjustable holder. After n steps of deposition, we would have (ITO/PEI/(CdTe/PDDA)*n). In this thesis the number of depositions (n) was varied from 9 to 23, to understand the effects of number of bilayers on photoluminescence and current better.

3.1 e. Back Side Etching

Before the sample is used for further characterization it is essential to remove the nano-particles and CdTe II deposited on the glass side of the device. This is required especially when the films are used for optical characterization. Usually the optical characterization methods involve the exposure of films to light. So the CdTe/PDDA film on glass side had to be etched to avoid undesirable effects while performing the optical measurements. Thus, the CdTe/PDDA deposited on glass is etched using dilute hydrochloric acid. Kimwipes were folded into small pieces and were dipped into dilute HCl using a pair of tweezers. Then the glass side of the substrate was wiped using this Kimwipes. After this step the substrates were cleaned in DI water to remove any HCl remaining on the substrate.

3.1 f Deposition of aluminum contacts

The aluminum contacts were made onto the CdTe films by thermal deposition. Thermal evaporation is one of the physical vapor deposition techniques and essentially involves passing current through the source material in a vacuum chamber. The source material (here aluminum) was placed on a filament made with a material possessing higher melting point than the material to be deposited. The filament used here was made of tungsten and the pressure in the chamber was maintained close to 2×10^{-6} Torr. A maximum current of 9 A was passed through the filament. The target substrates were placed on a disc above the source material. When the high current was passed through the boat, the aluminum foils got vaporized and got deposited onto the substrates. The current was increased in steps of 0.2 A, to prevent breakage of the tungsten filament. For every step of the current increase, the pressure in the chamber raised due to the vapors that developed. Each step of the current increase was done only after the pressure in the chamber got stabilized. In the absence of vacuum the vapors would get deflected and the deposited film would not be uniform, so a higher vacuum in the chamber was required for a uniform film deposition and to avoid oxidation of the source material. The aluminum contacts were made by using a mask made of aluminum foil which had an area of 0.07 cm^2.

3.2 X-Ray Diffraction (XRD)

The interaction of X-rays with a crystalline material results in a diffraction pattern which is usually known as XRD. This pattern is unique to each material and when a mixture of materials is exposed to the X-rays then each produces a pattern of its kind. XRD therefore provides valuable information about the phase, the structure and the composition of the sample under test [24].

Usually in a crystal the X-rays are diffracted by a series of parallel planes. Orientation of these planes is defined with Miller indices h, k and l which are integers. If a, b and c are considered to be axis of the unit cell then h, k and l would cut the axis a, b and c into h, k and l sections respectively. If d is the spacing between the parallel planes then the constructive interference would occur at an angle of incidence θ which satisfies Bragg's law (equation1)

$$2d\sin\theta = n\lambda ----(1)$$

where n= integer and λ= wavelength of the x-rays.

The XRD pattern obtained for a sample shows the peak intensities at 2θ positions corresponding to the d-spacing among the planes in the crystal. This would let us know the indices of the planes and the phase of the material could be estimated by comparing with previously calculated reference. The diffraction patterns of most of the available materials is recorded and standardized. When a material is characterized with XRD, the results are compared with a standard set of data and the material could be identified. In this thesis the thiol capped CdTe was characterized using XRD to determine its phase and crystal structure.

3.3 Optical Absorption and Photoluminescence

Optical absorption is an important technique to calculate the band gap (E_g) energy of a semiconductor. Photons of an appropriate wavelength range are made to be incident on the test sample and the absorption is recorded.

In semiconductors, the valence band contains electrons while the conduction band contains the empty states. When the sample is excited with photons and if the energy of the photon is greater than the energy gap between valence and conduction bands (band gap) then the photon would be absorbed (figure 3.4) [25]. The electron excited to conduction band may initially have energy higher than the other conduction band electrons. Thus the electron looses the excess energy to lattice and reaches the thermal equilibrium. The sample would not absorb any photon with energy less than E_g because it cannot excite electron to the conduction band. For this reason the optical absorption gives a good estimation of the band gap.

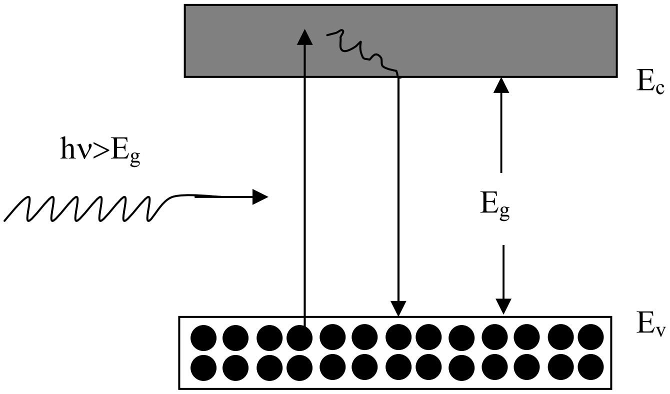

Figure 3. 5 Absorption of photons with $h\upsilon>E_g$

The measurement of the absorption spectrum was done for the CdTe II solution and the CdTe II deposited on ITO coated glass. For the solution pure DI water in a cuvette was taken as a reference while ITO coated glass substrate was used as a reference sample for the CdTe II film. Spectral measurements were done using a dual beam spectrophotometer as shown in the figure 3.6 [26, 27]. In this instrument two beams of equal intensity are passed such that one would go through the sample and the other through the reference substrate. The resulting intensities of both beams are compared over the entire wavelength range and plotted as $k*\log_{10}(I_0/I)$. I_0 was the intensity through the reference sample while I was the intensity through the sample and k was nearly equal to 100.

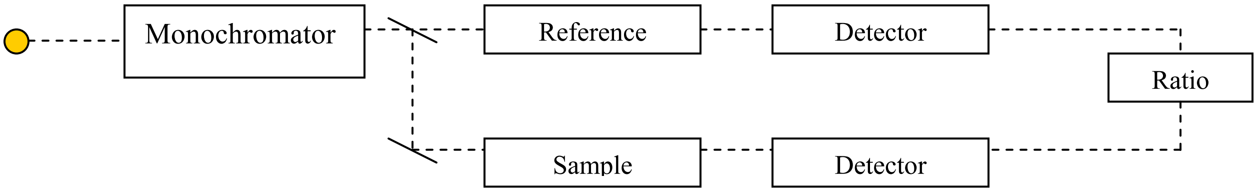

Figure 3. 6 Block diagram of the UV-Vis Spectrophotometer

Photoluminescence is the principle by which light emission from a semiconductor occurs for direct excitation and recombination of electron hole pairs. The recombination of EHPs (electron hole pairs) can occur either by electrons excited to the conduction band or trapped electrons in the trap state (E_t) falling back to its ground state. This process is explained in detail below in figure 3.7.

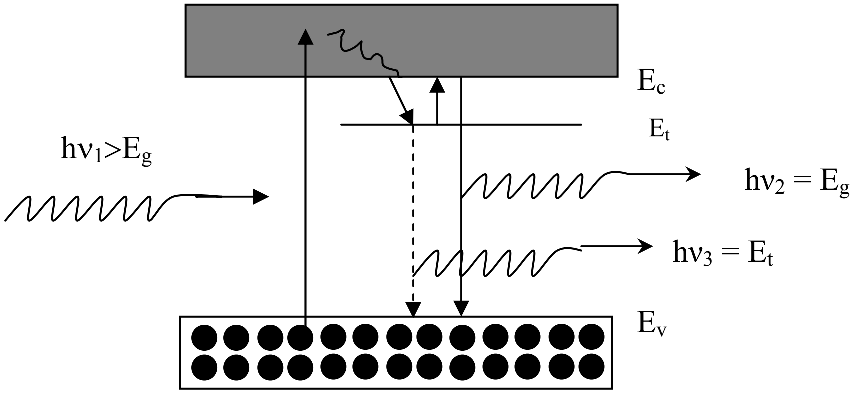

Figure 3. 7 Excitation and recombination mechanisms in PL with a trap level for electrons.

The measurement of photoluminescence spectrum was done by using a SPEX 2 – Fluorometer which was automated by connecting it to a computer through a GPIB port, thus enabling continuous measurement of the PL spectrum. The incident light (λ_1) was varied from 320-420 nm and the emission spectrum (λ_2 and λ_3) was recorded in the range of 450 to 700 nm.

3.4 I-V Measurement Setup

I-V measurements on the devices were performed using two Keithley Digital Multi Meters and a DC power supply. The circuit diagram is depicted in figure 3.8. These instruments were interfaced to a computer and measurements were recorded by a program written in the LabView software. Measurements were made within a voltage range of -10V to +10V at a step interval of 1 second.

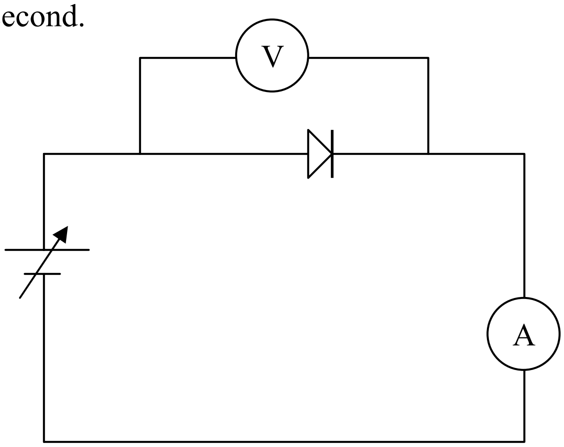

Figure 3. 8 Circuit Diagram for the I-V measurements

3.5 Capacitance Measurements

This setup consists of HP4192A impedance analyzer interfaced to a computer. Software written in LabView recorded the measurement values. The HP4192A has a measuring frequency range of 5 Hz to 13 MHz and a DC bias voltage range of -35 V to +35 V used for measuring capacitance as a function of voltage and frequency.

4. Material and Optical Characterization

4.1 XRD

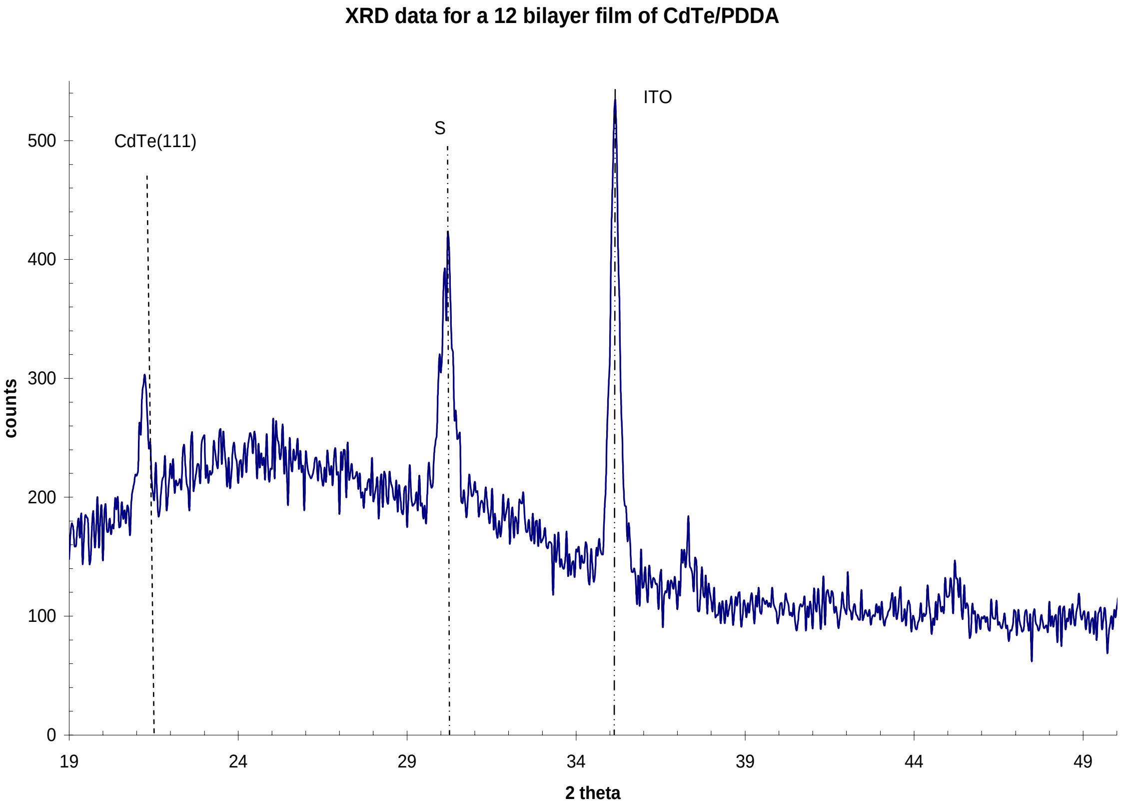

Figure 4. 1 X-Ray diffraction patterns on a 12 bilayer film of (CdTe II and PDDA)

From figure 4.1, it can be seen that the X-ray diffraction pattern of a 12 bilayer film of CdTe II and PDDA shows peaks at 21.5°, 30 °, and 35 °. The peak at 21.5° corresponds to a cubic phase of CdTe (111) [28] while the peak at 30 ° corresponds to sulfur [JCPDS]. The peak at 35 ° was that of ITO which was used as the substrate for the film. The peak for Sulfur is also seen here because of the presence of thiol capping around the CdTe. For verification of this data another film with 23 bilayers was also characterized through X- ray diffraction.

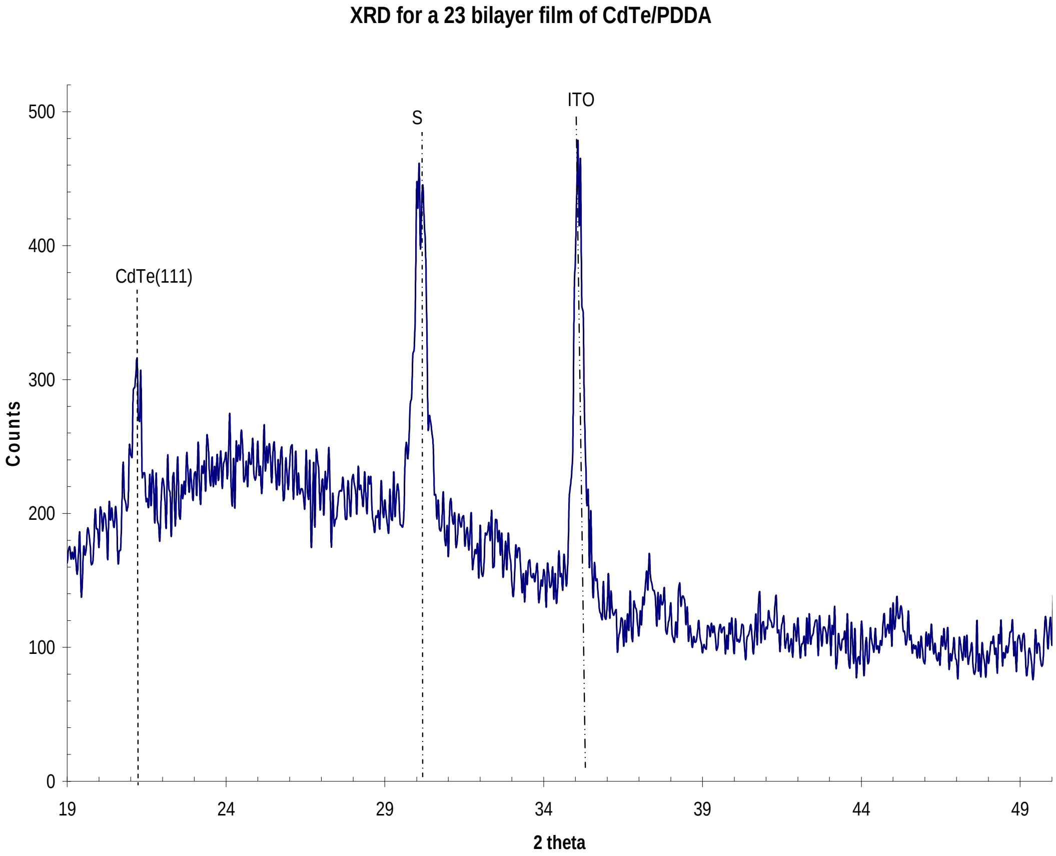

Figure 4. 2 X-Ray diffraction patterns on a 23 bilayer film of (CdTe II and PDDA)

The X-ray diffraction pattern of a 23 bilayer film was almost identical to the 12 bilayer film. The peak positions were at 21.2°, 30 °, and 35 ° respectively, which as in the previous corresponded to CdTe (111), sulfur and ITO respectively. After the structural and material verification of the substance obtained, it was used for the fabrication of devices.

4.2 Thickness Characterization

This section analyses the effect of number of bilayers on the thickness of the film. The thickness measurements of the film were performed using a Dektak profilometer. A number of films with different number of bilayers were fabricated and analyzed. The variation of thickness with respect to the number of bilayers is tabulated in Table 4.1.

Number of Bilayers	Thickness in nm
12	180
15	243
18	304
23	380

Table 4.1 Effect of number of bilayers on thickness of the film

From the table it can be seen that as the number of bilayers increased the thickness of the film also increased.

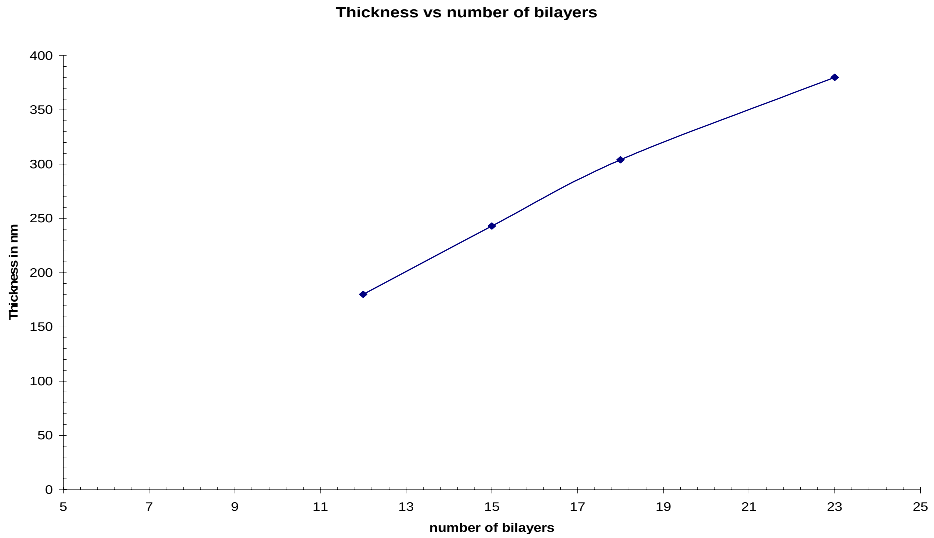

Figure 4. 3 Effect of thickness on the number of bilayers

Figure 4.2 illustrates that the relationship between the thicknesses with the number of bilayers was linear. The measurements were taken a second time to check for repeatability and the deviation in the measurements were negligible. Also other techniques like ellipsometry could not be used to the individual thickness as the combination of CdTe and the polymers formed a composite mixture making it difficult to determine the separate layer thickness.

4.3 Optical Characterization

4.31 Optical Absorption of nano-CdTe II solution

The optical absorption of a solution of CdTe II and a film containing bilayers of CdTe II and PDDA were measured in the wavelength range of 265nm – 900 nm. From the absorption curves the band gap of CdTe II were calculated for the films and the solution. The absorption intensity versus wavelength graphs for the solution and films are shown in Figure 4.4 and 4.6 respectively.

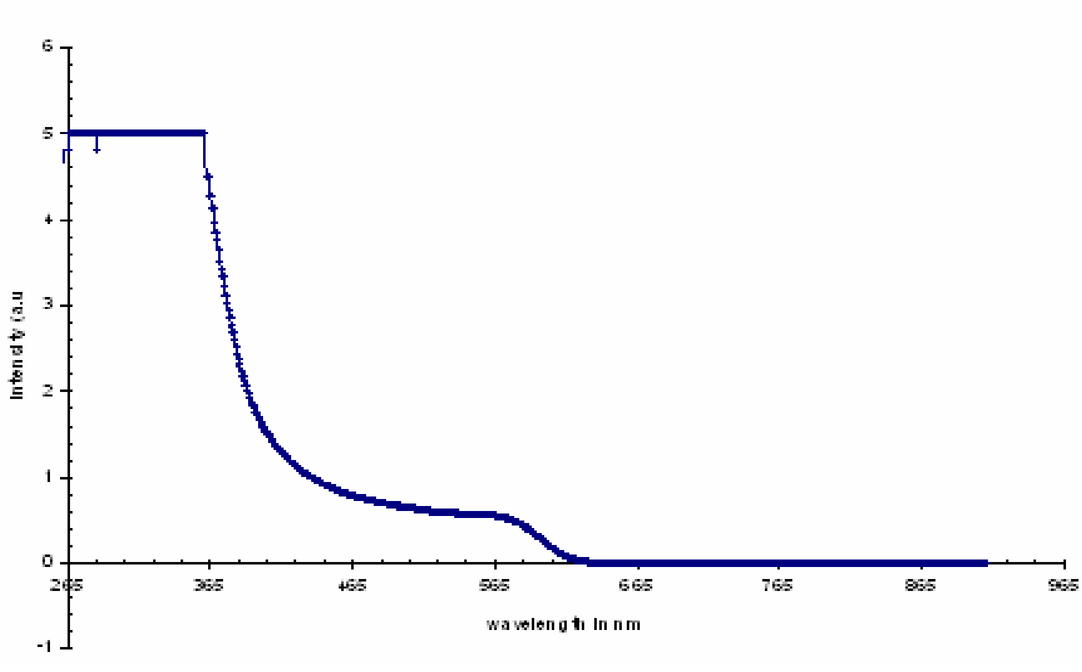

Figure 4. 4 Optical absorption for thiol capped CdTe solution

The absorption characteristics of CdTe II show an edge around 600 nm approximately. The sharp rise in absorption is an indication of the uniformity in particle sizes in solution. In order to better understand the absorption characteristics, the absorbance was plotted as a function of energy ($E_g = hc/\lambda$)) in figure 4.5.

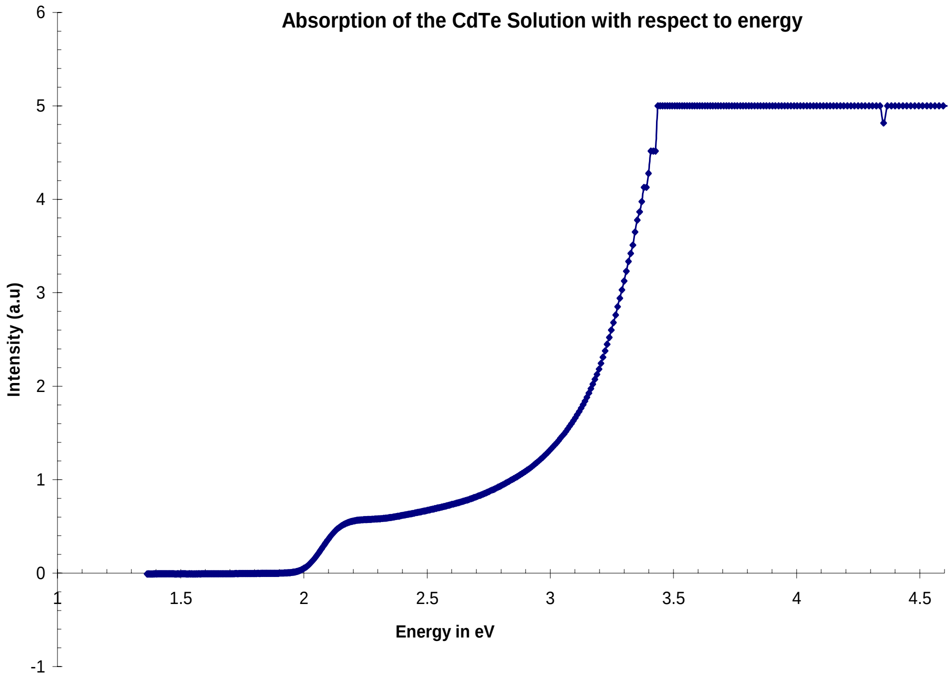

Figure 4. 5 Absorption characteristics as a function of Energy

From the above graph it can be seen that the onset of absorption is around 2.1 eV indicating that the band gap of the material is around 2.1 eV. For bulk CdTe particles the band gap is equal to 1.6 eV [29] while the nano-particles have a much higher band gap which could be attributed to level to level transitions in nano-particles due to the quantum confinement effect. The graphs in figure 4.4, 4.5, 4.6 and 4.7 were plot k x $\log_{10}(I_o/I_t)$, where I_o is the incident light, I_t the transmitted light and k=100.

4.32 Optical absorption of (CdTe/PDDA) films

The optical absorption for films containing different number of bilayers of CdTe and PDDA were done at a wavelength range of 280 – 900 nm. Figure 4.6 shows the optical absorption for a 12 bilayer film. The intensity peak of absorption was lesser than that of the solution indicating that the film absorbed less light than the film.

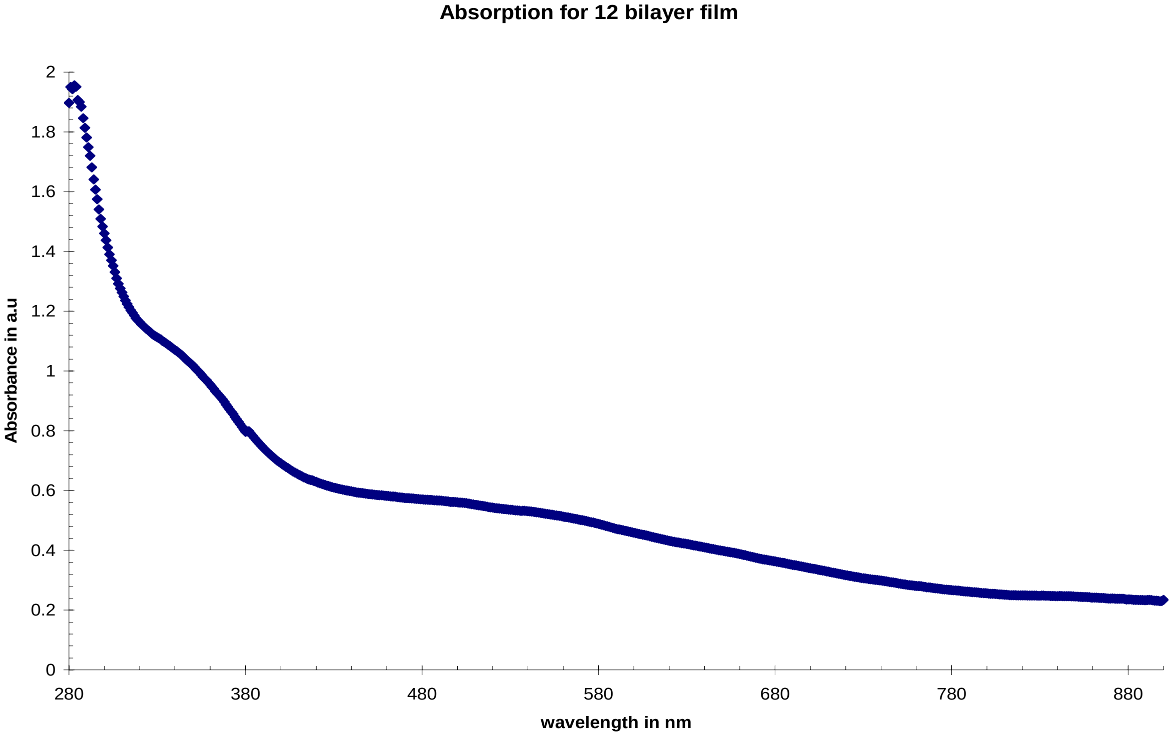

Figure 4. 6 Absorption of a film with 12 bilayers of CdTe/PDDA

The onset of absorption of the 12 bilayer film was not as well defined, unlike the nano-particle solution. This could be attributed to the variation in particle sizes in films which in turn could be due to clustering or agglomeration of nano-particles in films [30].

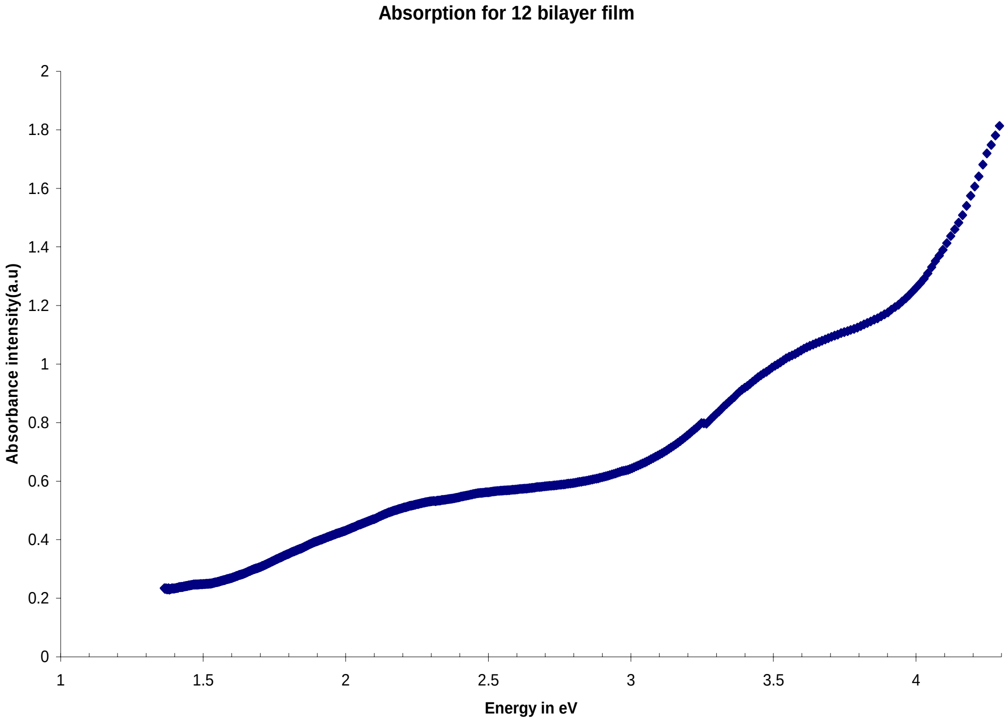

Figure 4. 7 Absorption characteristics as a function of Energy

Even when the absorbance was plotted as a function of energy (figure 4.7), the onset of absorption could not be determined accurately. It can be seen that the onset of absorption was in the range of 1.5 eV to 2 eV indicating that the band gap of nano-particles in the film could vary from 1.5 to 2 eV. In order to determine the average band gap of the nano-particles in film, Tauc's law was used (discussed later in section 4.35).

4.33 Variation in absorbance with thickness of the film

Films of various thickness were made and there absorbance characteristics were studied (figure 4.8). The intensity of absorbance increased as the film thickness increased. Similar characteristics were observed previously by Dr. Kotov [31] for (PDDA/YIG) films.

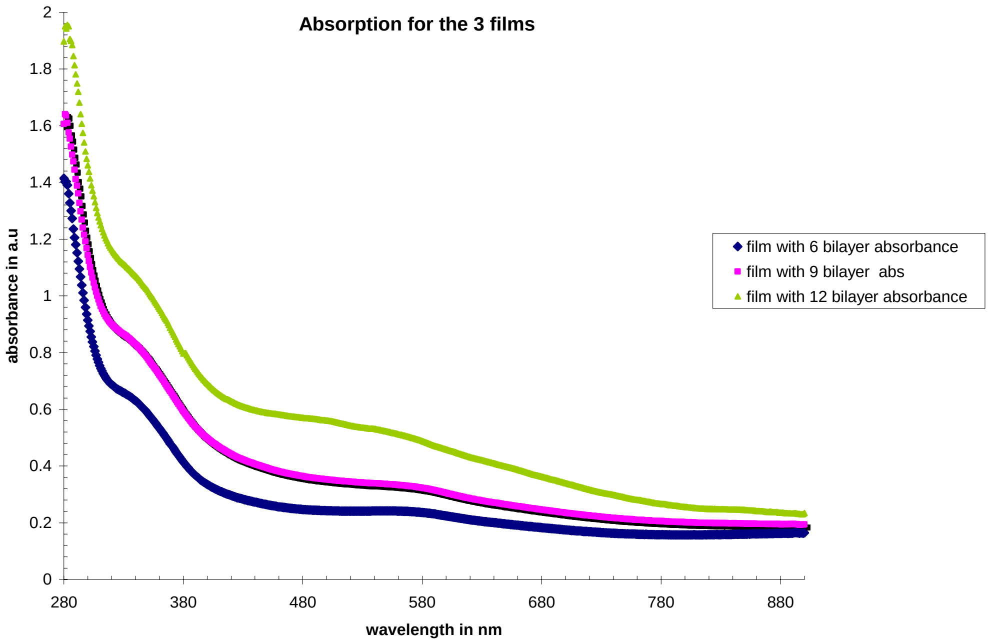

Figure 4. 8 Absorbance of films with thickness of 92 nm, 130 nm, and 180 nm respectively

From the figure above it can be inferred that the absorbance intensity and the onset of absorption increases as the film thickness increases, thus suggesting that as the films became thicker the clustering of particles also increased. The increase in clustering of nano-particles would in turn increase the average particle size and thus cause a decrease in its band gap or an increase in the absorption wavelength.

4.34 Determination of Band Gap from absorption characteristics of solution

The band gap of the CdTe II nano-particles from its solution can be determined by the Taucs' Law method for direct band gap semiconductors given by:

$$(\alpha h\nu)^2 = (h\nu - E_g)\ldots\ldots\ldots\ldots\ldots\ldots\ldots\ldots\ldots\ldots\ldots\ldots(4.1)$$

where α is the absorption coefficient at an energy hν, hν is the energy of the wavelength, and E_g is the band gap energy of the semiconductor. α can be further determined for each wavelength by measuring the optical absorption, A, of a colloidal suspension of stabilized CdTe II particles, by means of the relation developed by J.I Pankove [32] and J.H. Fendler [33].

$$\alpha = \frac{2.303\rho \times 10^{3} \times A}{l \times c \times M} \text{..............................(4.2)}$$

With $\rho = 5.86$ g cm^{-3} the density of thiol capped CdTe, *l* the optical path length (1 cm), *c* the molar concentration of CdTe (10^{-07} M), and *M* the molecular weight of CdTe II (240).

From equation 4.2 the absorption coefficient α was calculated for each wavelength and a graph between $(\alpha\, h\, \nu)^{2}$ and h ν was plotted. The extrapolation of the curve onto the x axis determines the value of band gap as it corresponds to the point h ν = Eg.

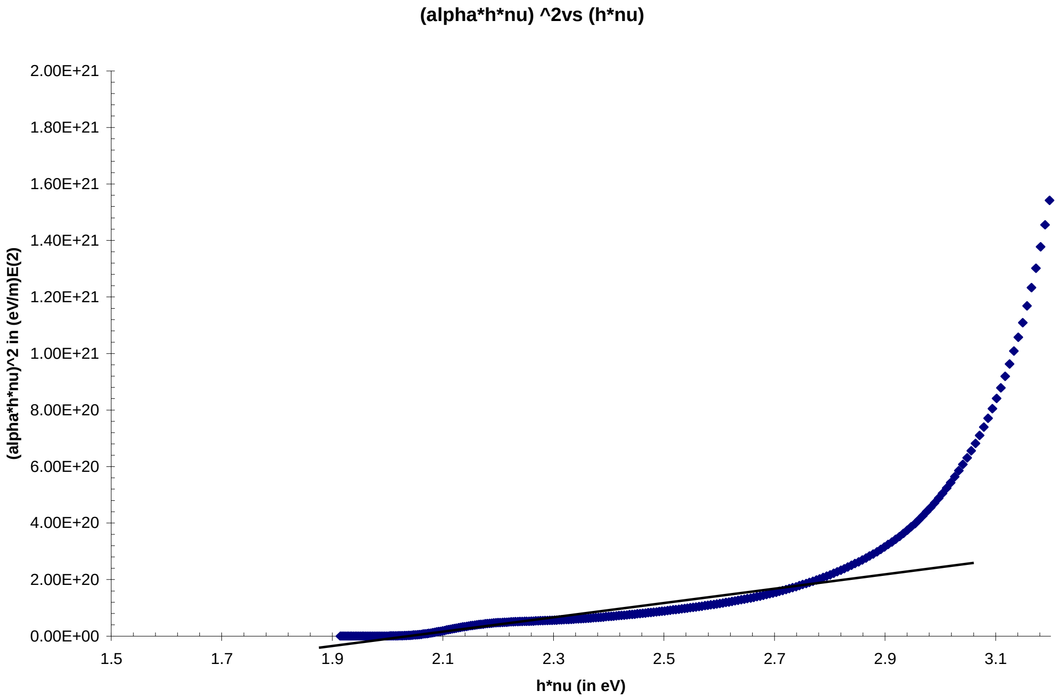

Figure 4. 9 Calculation of band gap from solution

From the graph above it can be seen that the calculated band gap for nano CdTe II particles from their solution is 2.1 eV. As discussed before the increase in the band gap of CdTe II nanoparticles can be attributed to 3D quantum confinement effects in nano-crystals.

4.35 Determination of Band Gap from absorption characteristics of films

The band gap of the nano-particles in films was calculated using Tauc’s law [34] given in equation 4.3,

$$(\alpha h\nu)^2 = (h\nu - E_g)\text{.......................................}(4.3)$$

where E_g is the effective band gap of the semiconductor. When the L.H.S of equation 4.3 becomes zero, then the energy of incident photon becomes equal to the effective band gap of the semiconductor. The absorption coefficient α can be determined from the fact that, if I_o be the intensity of light incident on the sample, I(x) the intensity at a distance x in the sample, δI the decrement in intensity at a small elemental volume δx at x, then δI depends on the intensity at x (or) I(x) and thickness of elemental volume δx, implying

$$\delta I = -\alpha I(x)\delta x \text{...} (4.4)$$

The proportionality constant α is defined as the coefficient of absorption and it depends on the material and photon wavelength, but not on the sample thickness. α has dimensions cm^{-1}.

Integrating 4.4 yields

$$I(x) = I_o \exp(-\alpha x) \text{.................................} (4.5)$$

Therefore at a sample thickness t,

$$I(x = t) = I_o \exp(-\alpha t) \text{....................................} (4.6)$$

$$or$$

$$I_t = I_o \exp(-\alpha t) \text{..} (4.7)$$

From equation 4.7 α can be determined to be

$$\alpha = (1/t)\ln(I_o / I_t) \text{......................................} (4.8)$$

The spectrophotometer used for optical absorption calculates k x $\log_{10}(I_o/I_t)$ for every wavelength of the spectral range used in the test, where the value of k was found to be nearly 0.01. As a result, the value of α is determined from the equation 4.8 on knowing the thickness of the sample (t).

Figure 4.10 is a plot of $(\alpha h\nu)^2$ against hν for the nano-crystal film. E_g was calculated by extrapolating α to zero [35].

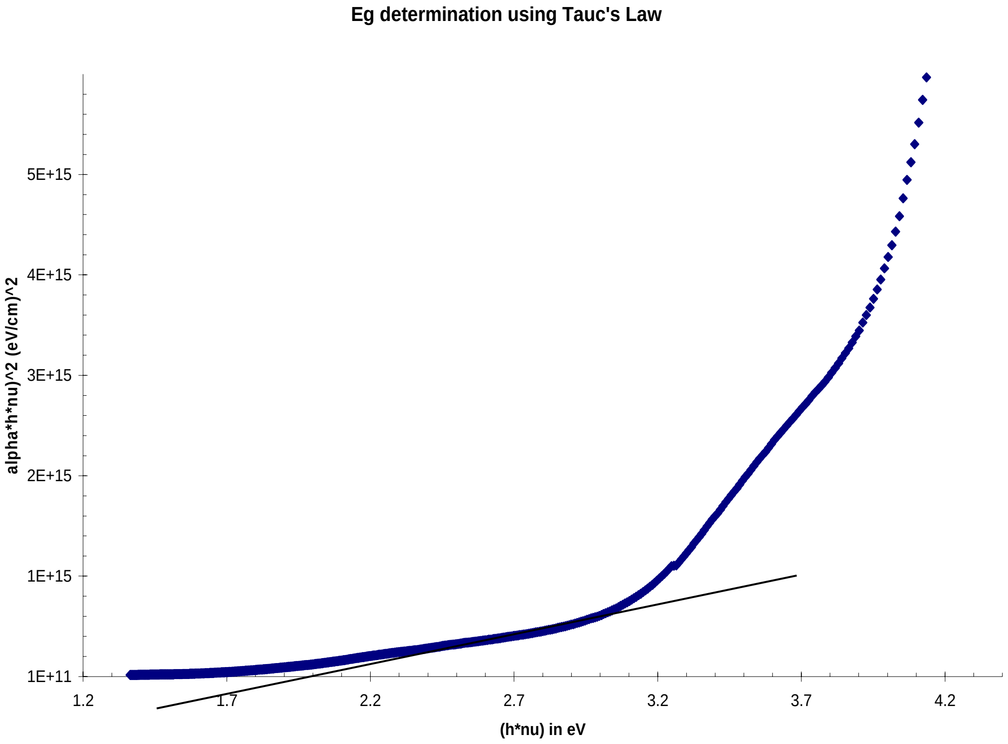

Figure 4. 10 Determination of Band gap using Tauc's Law

The band gap of the nano-particles in film was found out to be 2eV which is slightly lesser than the value of 2.1eV (for nano-particles in solutions). This could be due to the clustering effect of nano-particles in films.

4.36 Photoluminescence Measurement

4.36 a. Analysis of Phosphorescence from the film and solution

The photoluminescence measurements were done for different excitation wavelengths 365 nm and 412 nm. As the set up of fluorometer here was inherently built for measuring photoluminescence of solutions, PL spectral measurements were taken for the pure CdTe II solutions but could not be measured for the CdTe II films. The film prepared exhibited high level of phosphorescence which was captured using a Canon A 80 digital camera.

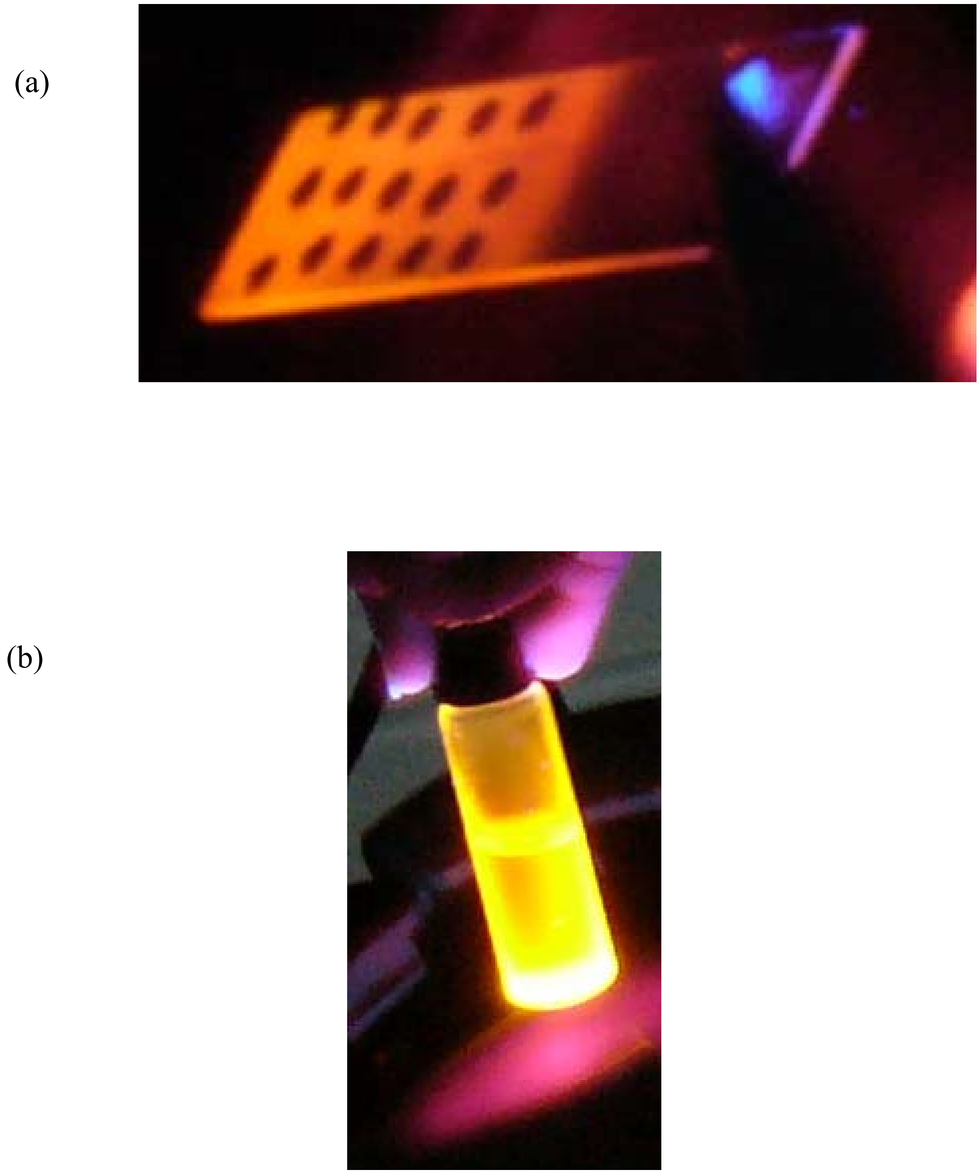

Figure 4. 11 Phosphorescence of (a.) film (b.) solution under the influence of a 365nm light source.

From figure 4.11 it can be seen that the film had orange luminescence while the solution exhibited yellow luminescence, indicating that the nano-particles in the film were bigger than that in solution. This red shift in luminescence was previously observed and reported by Dr. Rogach [36]. The reason for the shift in the luminescence was attributed to agglomeration of nano-particles in films.

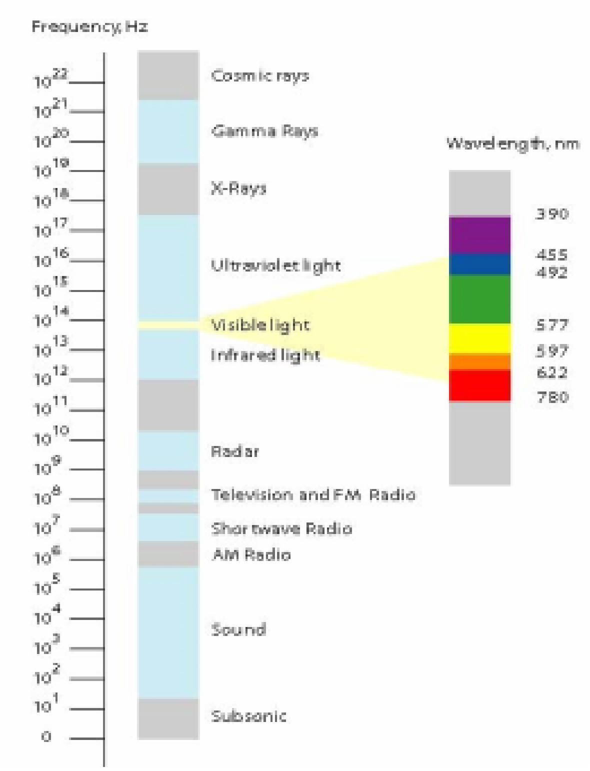

Figure 4. 12 Wavelength and frequency spectrum of visible light

From figure 4.11 and 4.12 it can be seen that the PL wavelength of the film was in the range of 597 nm to 622 nm, and that of the solution was in the range of 577-597 nm. From sections 4.34 and 4.35, the band gap of nano-particles in the film was found to be 2 eV (which corresponds to a wavelength of 620.35 nm) and the band gap of nano-particles in solution was found to be 2.1 eV (which corresponds to a wavelength of 590.8 nm). This is in accordance to the expected values for wavelength given in figure 4.12.

4.36 b. Measurement of PL spectrum

The PL spectrum for the CdTe II solution for excitation wavelengths of 365 nm and 412 nm are plotted below in figure 4.13.

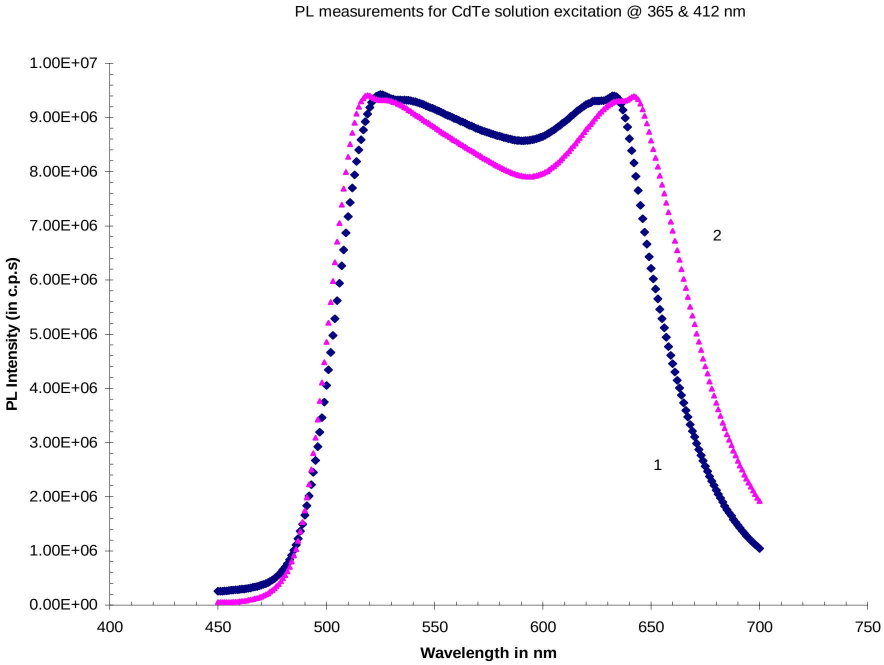

Figure 4. 13 PL spectrum of CdTe solution for an excitation wavelength of 1. 365 nm and 2. 412 nm.

Figure 4.13 shows a plateau like appearance in the PL spectrum reflecting almost equal emission intensity over a wide range of wavelengths from 500 nm to 700 nm, for excitation wavelengths of 365 nm and 412 nm respectively. The PL spectrums for the two excitation wavelengths were identical, but the one at 412nm had lesser intensity which could be due to the lesser energy of excitation light. Such plateau like appearance was observed by Kotov et al. [37] for CdTe II films prepared on ITO. The primary reason for a wide PL spectrum was attributed to the presence of traps (interstates), as electrons from conduction band before recombining with the holes in the valence band could fall into interfacial traps and then fall from the traps to its ground state releasing energy corresponding to the energy level of the traps [38]. The contribution of traps in luminescence of display devices has been analyzed in detail by Singh et al. [38].

5. Electrical Characterization

5.1 J-V Characteristics

The J-V characteristics of the devices were measured by applying a voltage across the device, with positive polarity to the Indium Tin Oxide (ITO) electrode and negative polarity to aluminum (Al) electrode. The J-V characteristics of various device structures that were fabricated are discussed below. Sections 5.11 to 5.13 discuss the J-V characteristics for uncapped CdTe nano-particles while sections 5.2 to 5.29 discuss the J-V characteristics for capped CdTe nano-particles.

5.11 Device Structure ITO/ CdTe I / Al

The first device structure consisted of nano-uncapped CdTe (or CdTe I) deposited through dip coating [40] on a clean ITO substrate and aluminum as the top electrode.

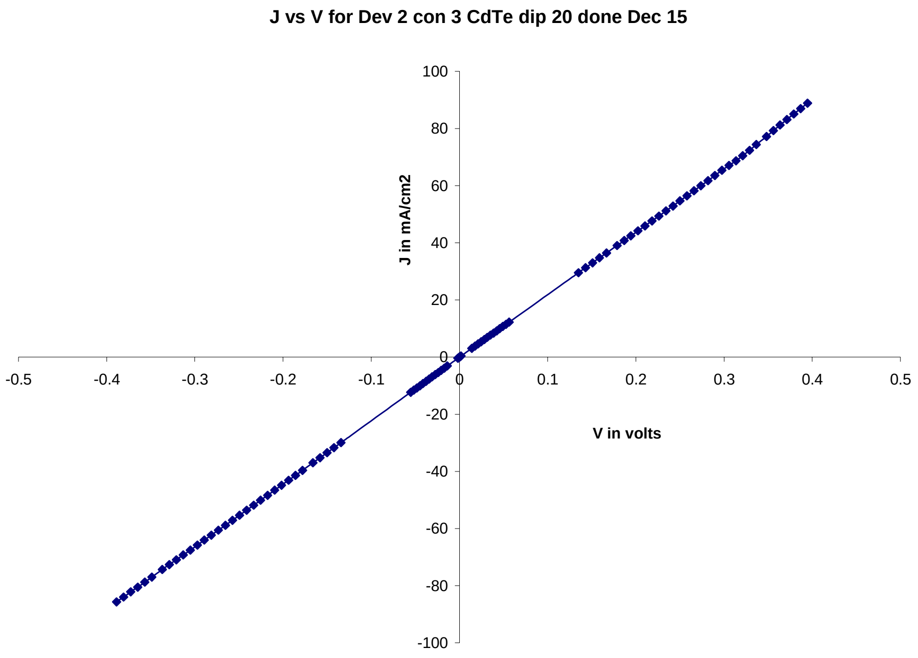

Figure 5. 1 J-V curves for the device structure ITO/CdTe I/Al

From figure 5.1 it can be seen that CdTe I formed a resistive contact with aluminum. This can be accounted due to the fact that CdTe I did not adhere to the ITO substrate when deposited directly. From the graph above the vertical resistance per unit area of the film was found to be nearly 5 Ω/cm^2. In order to make a good diode from the nano-particles a good adhesive layer was required. So, organic polycations PDDA (poly diallyl dimethyl ammonium chloride solution) and PEI (Polyethylenimine) [39] were used for this purpose. The advantages of using the organic layers were, they caused the nano-particles to adhere to the ITO substrate and they were conducting with a resistance of nearly 10^5 Ω/ cm^2 when their concentrations were 1 mg/ml.

5.12 Device Structure ITO/PEI/(CdTe I /PDDA)*10/Al

The J-V characteristics of ITO/PEI/(CdTe I /PDDA)*n/Al were studied in detail by varying the number of bilayers of CdTe and PDDA (n) and the concentrations of the organic layers. PEI was used as the organic polycation on the substrate because of its adherence to ITO [refer chapter 2]. The organic polycations concentrations were chosen to be around 10 mg/ml, while the nano-particle solution had a concentration of 1 mg/ml. The resultant J-V curves for a 10 bilayer device are shown in Fig 5.2. It can be seen that the device structure exhibits a good diode behavior, but the currents were in the order of 0.1mA/cm^2. The values were much lower than the theoretical values of nearly 10 mA/cm^2 [39]. One of the main reasons could be due to the high concentrations of the organic layers which made the film more resistive.

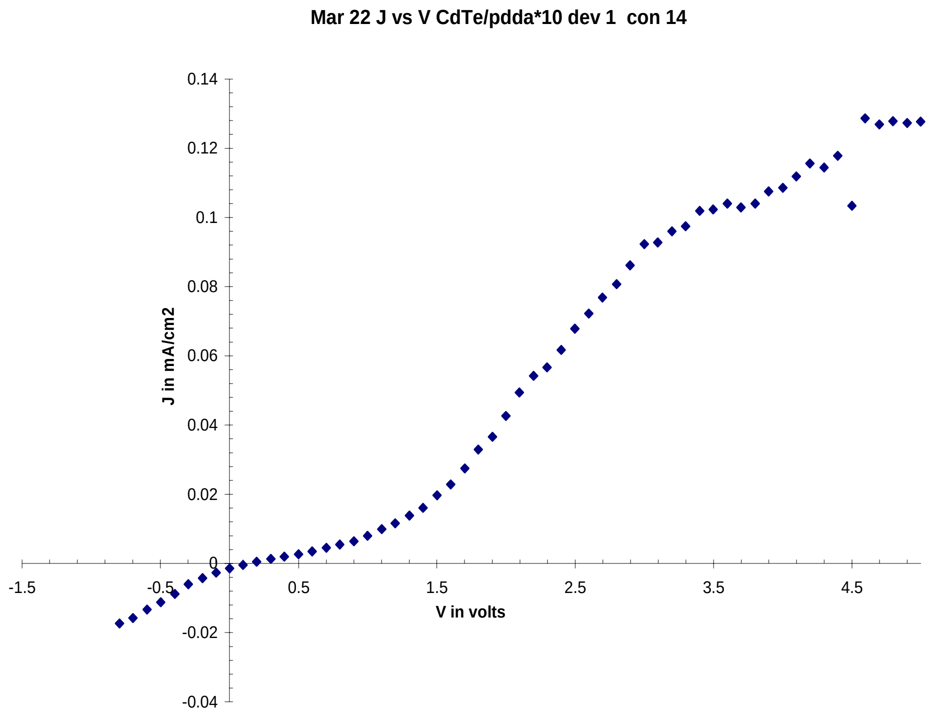

Figure 5. 2 J-V curves for the device structure ITO/PEI/(CdTe I /PDDA)*10/Al

From fig 5.2, it can be seen that the turn on voltage for the diode was nearly 1.5 V. In order to improve the current the organic concentrations were reduced to 1 mg/ml for the following devices.

5.13 Effect of concentration of the organic polycations on the J-V curves of Uncapped CdTe thin film devices.

Using the same device structure (ITO/PEI/(CdTe I /PDDA)*10/Al) new devices were fabricated using the layer-by-layer technique but with concentrations of the organic polycations reduced to 1 mg/ml. The effect of resistance per unit area for the organic polycations increased by a factor of 45 as the concentration was increased by a factor of 10. This could be inferred from the fact that a 1 mg/ml of PDDA deposited on a substrate had a resistance of 10^{3} Ω/cm^{2} while a 10 mg/ml of PDDA had a resistance of $4.5\text{x}10^{4}$ Ω/ cm^{2}.

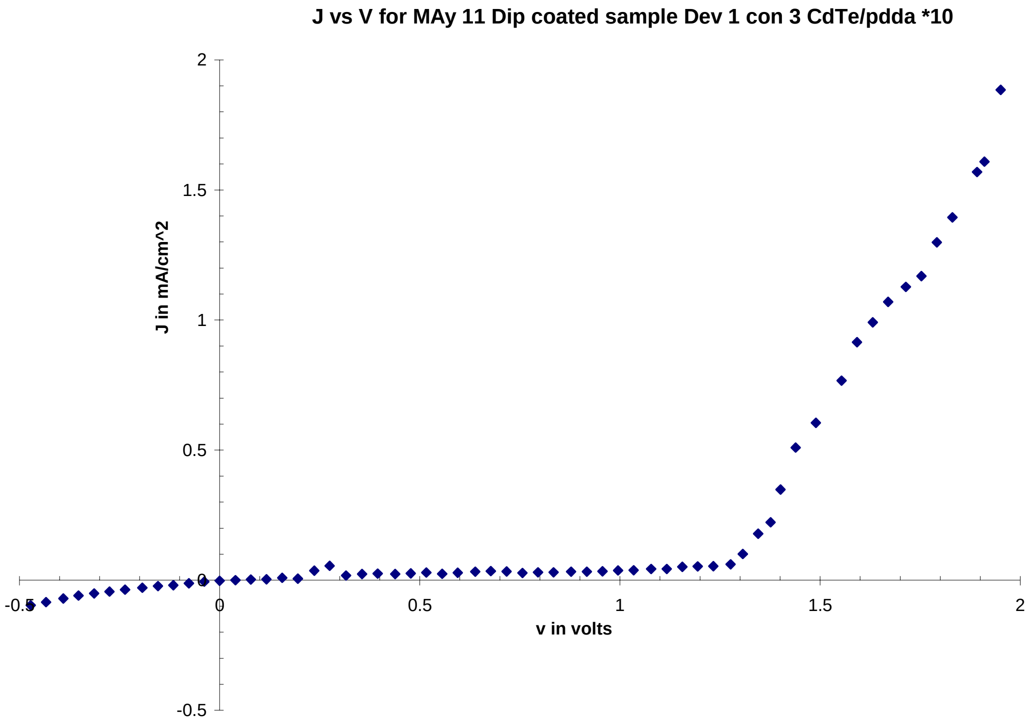

Figure 5. 3 J-V curves for the device structure ITO/PEI/(CdTe I /PDDA)*10/Al, when the concentration of the organic polycations were reduced to 1 mg/ml.

It can be seen clearly that the current density for the new device has increased by a factor of fifty, by reducing the concentration of the organic polycations (PEI, PDDA). Also a small shoulder in current is seen at 0.28 V which could be attributed to the presence of traps in the devices. The possible electron transport mechanisms in these devices could be tunneling, thermionic or Schottky, all the three possible mechanisms are discussed later in Section 5.25.

5.14 Effect of number of bilayers on Uncapped CdTe thin film devices.

The number of bilayers of CdTe and PDDA were increased from 10 to 15 and the resultant J-V characteristics were measured [figure 5.4]. There was a slight increase in current density when compared to the device with 10 bilayers.

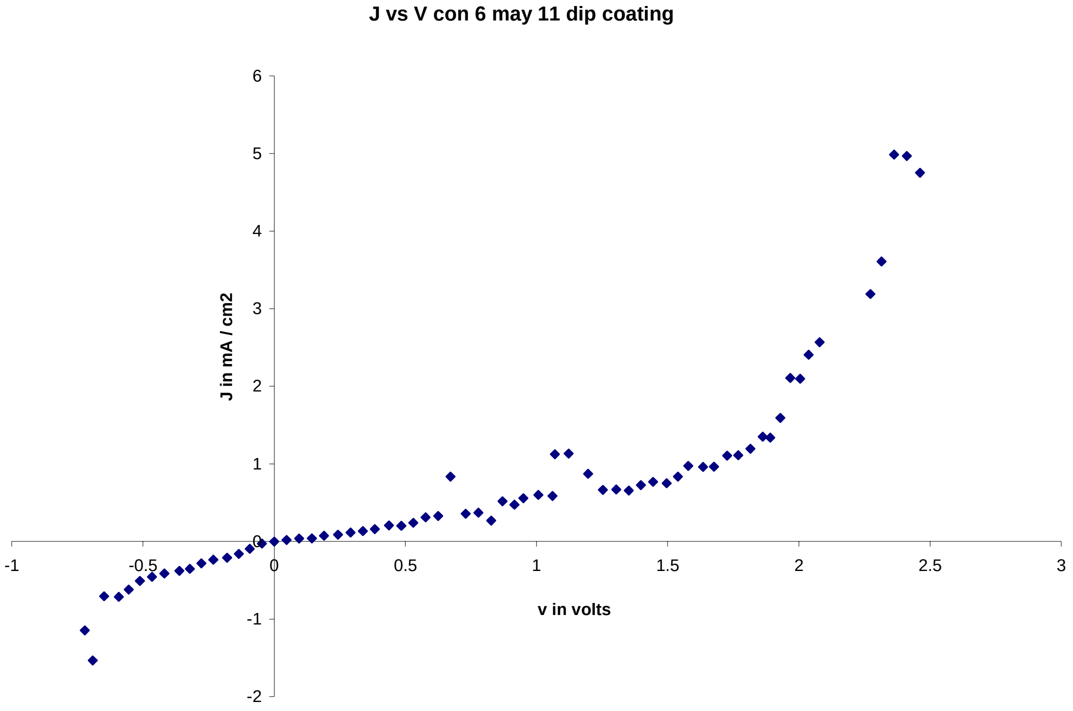

Figure 5. 4 J-V curves for the device structure ITO/PEI/(CdTe I /PDDA)*15/Al

For instance when the applied voltage was 1.5 V, the current density for a 10 bilayer device was 0.5mA/cm^2 [figure 5.3], while it was 1 mA/cm^2 [figure 5.4] for a 15 bilayer device. This indicates that as the number of bilayers of CdTe and PDDA were increased, the current density increased. Though adding more number of organic layers would tend to make the film more resistive, the current density increased, suggesting that the current mechanism was dominated by addition of nano-particles in the films.

The following sections discuss the J-V and C-V characteristics of thiol-capped CdTe devices and the mathematical modeling of electron transport in them. These devices exhibited good photoluminescence and could also be used to make electroluminescent devices.

5.2 J-V Analysis for thiol Capped CdTe Devices

5.21 Forward Current Analysis of thiol capped devices

The analysis of J-V, C-V characteristics and modeling the device through these characteristics is the crux of this thesis work. A typical device with 12 bilayers would have the device structure of ITO/PEI/(CdTe II /PDDA)*12/Al, where CdTe II indicates that the CdTe nano-particles are thiol capped nano-particles. To understand the working of device better, the forward and reverse characteristics are analyzed separately.

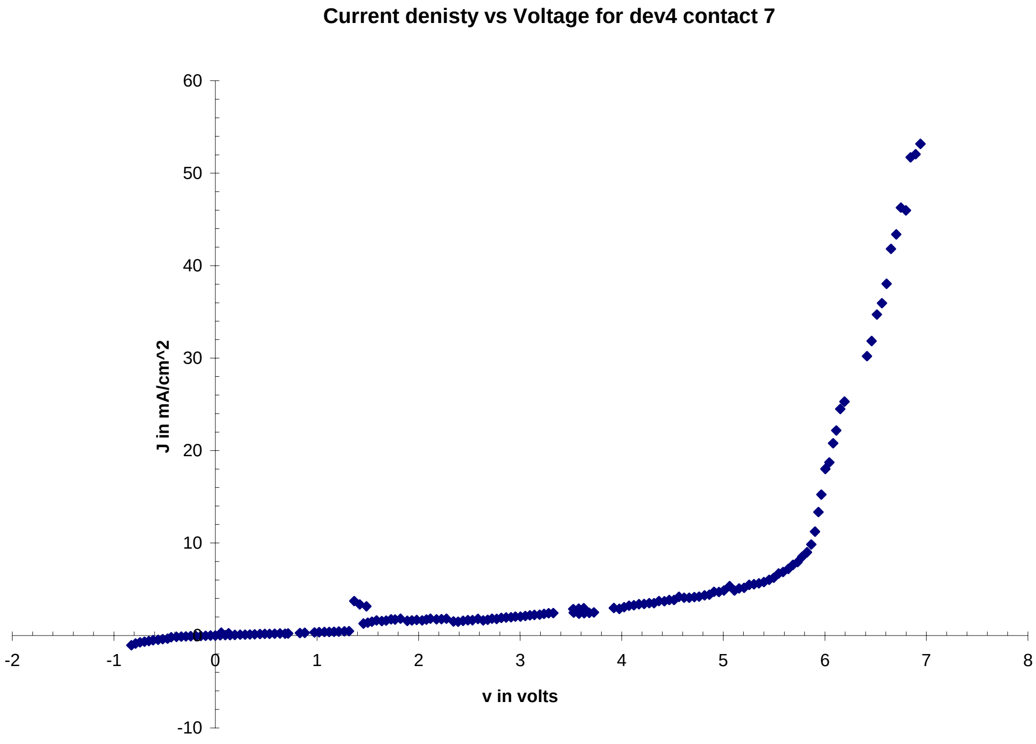

Figure 5. 5 J-V curves for the device structure ITO/PEI/(CdTe II /PDDA)*12/Al

From figure 5.5, it can be clearly seen that the current density has increased by ten times compared to the devices made with uncapped CdTe particles [figures 5.1, 5.2 & 5.3]. This shows that the thiol capped CdTe is much more useful for making diodes with high current density. There is a shoulder seen in the current at 1.5 V. The possible reason for the shoulder could be presence of the traps in the device. Electrons from the interface states probably tunnel through the barrier between CdTe II and ITO. Also the turn on voltage for thiol capped CdTe II devices are higher than the non thiol capped CdTe I devices. The turn on voltages varied from 3-6 V for all thiol capped CdTe devices.

5.22 Effect of Number of Bilayers on Forward Current

When the analysis of effect of bilayers on current density was done, an interesting phenomenon was observed. The current density increased as the number of bilayers increased until a certain limit, but when the number of bilayers increased beyond a certain limit the current density decreased as opposed to the expected increase with the number of bilayers.

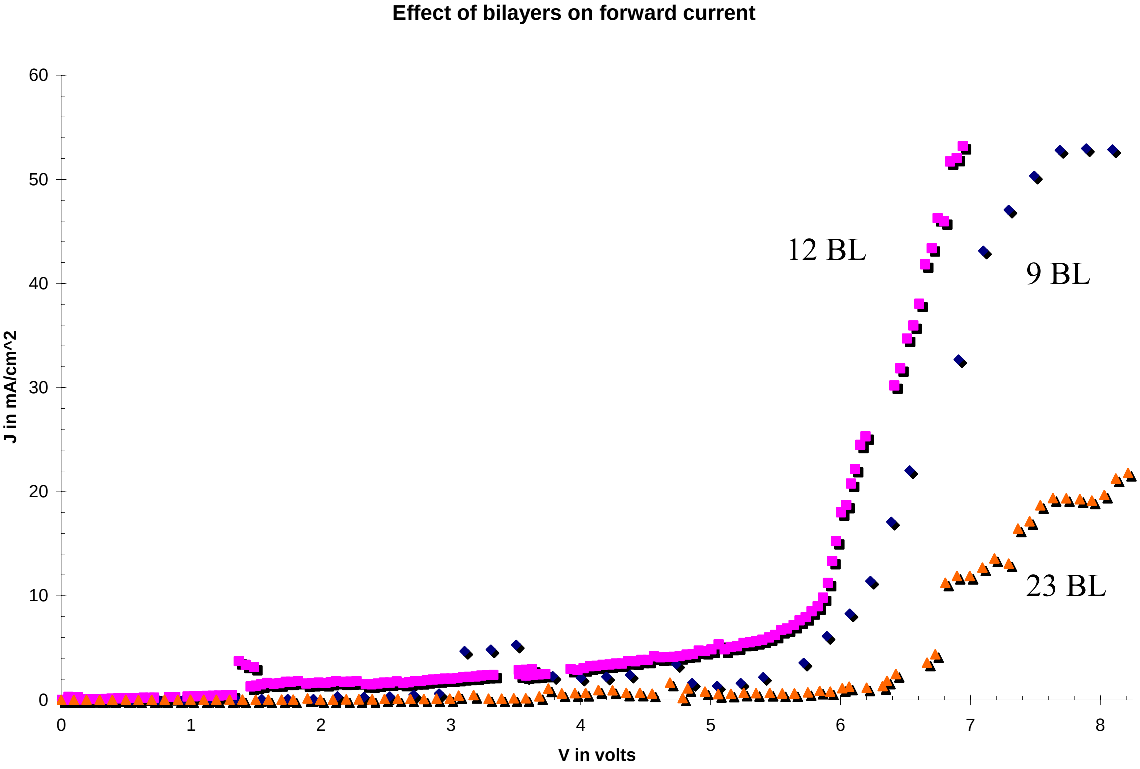

Figure 5. 6 J-V curves for 12, 9 and 23 bilayer devices

Figure 5.6 shows that the current density for a 12 bilayer device is higher than the 9 bilayer device but a 23 bilayer device had a lower current density than the 9 bilayer device. This phenomenon was observed and reported by Dr. Rogach et al., in his work on CdTe II devices [39]. In order to explain this anomaly, current density was plotted as a function of electric field [Figure 5.7].

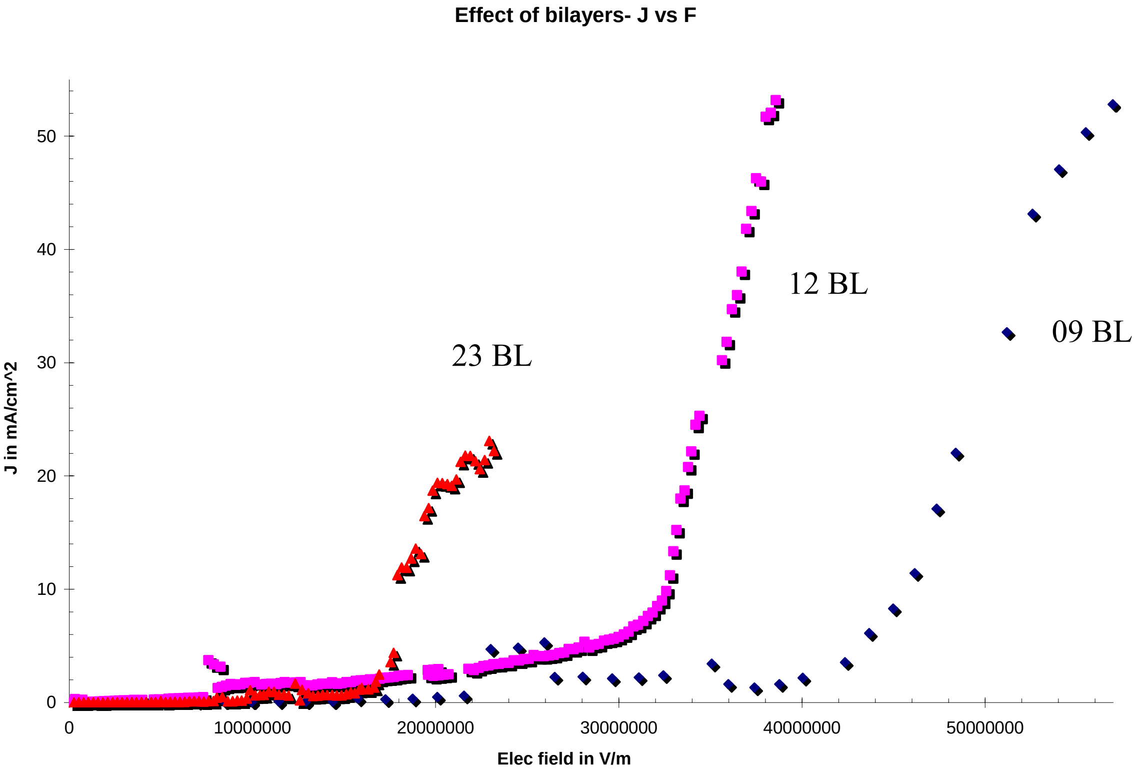

Figure 5. 7 Current Density vs. Electric Field for 23, 12 and 9 bilayer devices

When plotted as a function of electric field, it can be seen clearly that the turn on voltage increases as the number of bilayer increases but the current density for a 23 bilayer was much less than the 12 and 9 bilayer films. This could be attributed the fact that as the number of bilayers increases, the number of organic layers increases consequently making the film more resistive thus giving lower currents for thick films. A field dependent current is evident from figure 5.7, as the number of bilayers increased the turn on field decreased proportionately, suggesting an inverse relation between them (unlike the J vs. V curves, where a clear relationship between the number of bilayers and turn on voltage could not be seen).

5.23 Effect of Time on Forward Current

The effect of time on the forward current was done by measuring the current vs. voltage on the first, second and third day after the device was fabricated. It was seen that the current density decreased with time, while the turn on voltage increased with time.

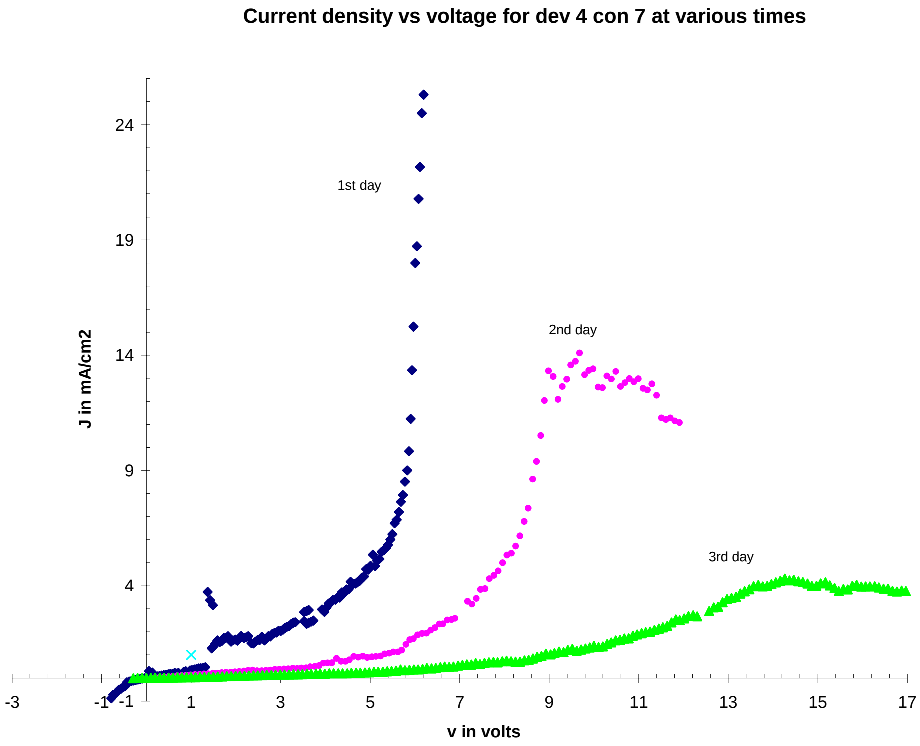

Figure 5. 8 Effect of time on Current Density (J in mA/cm^2) for a 12 bilayer device

Figure 5.8 shows clearly that the device resistance increases with time, thus leading to a decrease in current density. The device on prolonged exposure to air degraded because of the oxidation of the nano-particles, making the film more resistive [41]. Films made of the polycations alone did not show much change in their resistance, when measured on the first, second and third day after fabrication, implying that the increase in resistance of our devices was primarily from the degradation of nano-particles.

5.24 Effect of UV light on Forward Current

To study the effect of UV light, a 365nm (3.4 eV) - "Blak Ray Long Wave Ultra Violet Lamp Model B 100 AP" light source was incident on the device. The measurement was performed at dark with the UV source as the only source of excitation.

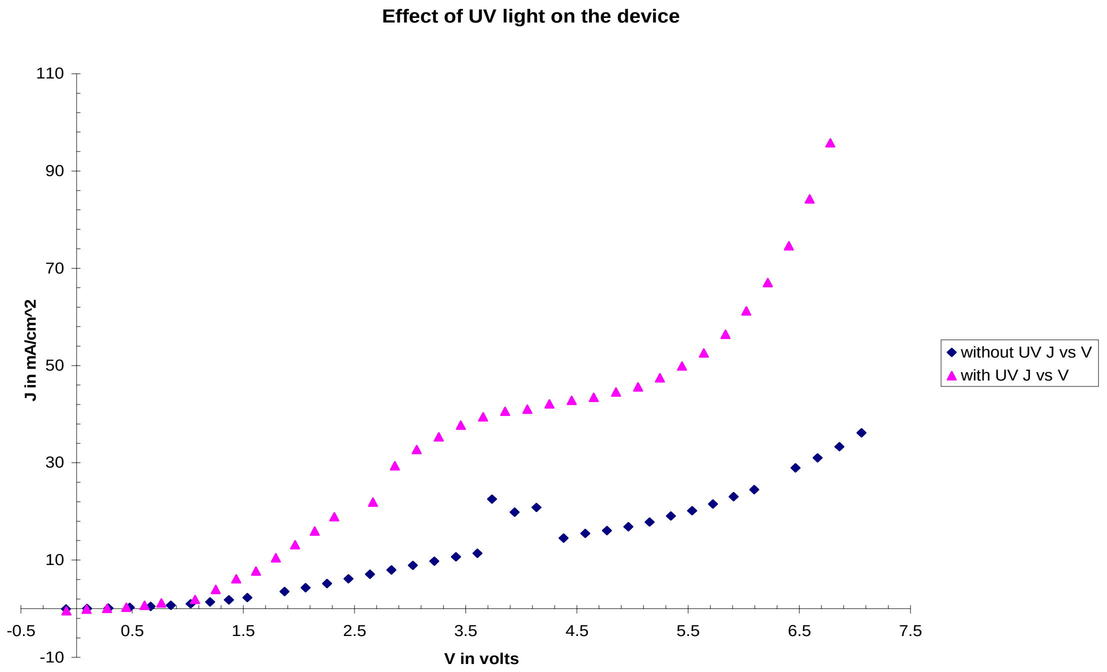

Figure 5. 9 Effect of UV light on forward current

From figure 5.9, it can be seen that there was a greater flow of current under the influence of UV light. This could be attributed to the fact that, under the influence of light more electrons were excited from the ground state to the conduction band of the nano-particles [48]. Then the increase in current could possibly be due to two mechanisms, either more electrons from the nano-particles crossed over a Schottky barrier formed between the nano-particles and ITO (metal) or they tunneled through a triangular barrier (formed between the nano-particles and the organic polycations) into the metal (discussed in detail in section 5.3).

5.25 Reverse Current Analysis of thiol capped devices

The analysis of reverse current was done by applying a negative voltage at the ITO electrode and keeping the aluminum electrode at zero potential. It was surprising to see that the device exhibited rectifying behavior even in the reverse direction and the values of currents were very similar to the currents obtained in forward direction. Similar characteristics where rectifying behavior was seen both in forward and reverse directions were reported for CdSe based devices by Dabbousi et. al. [50].

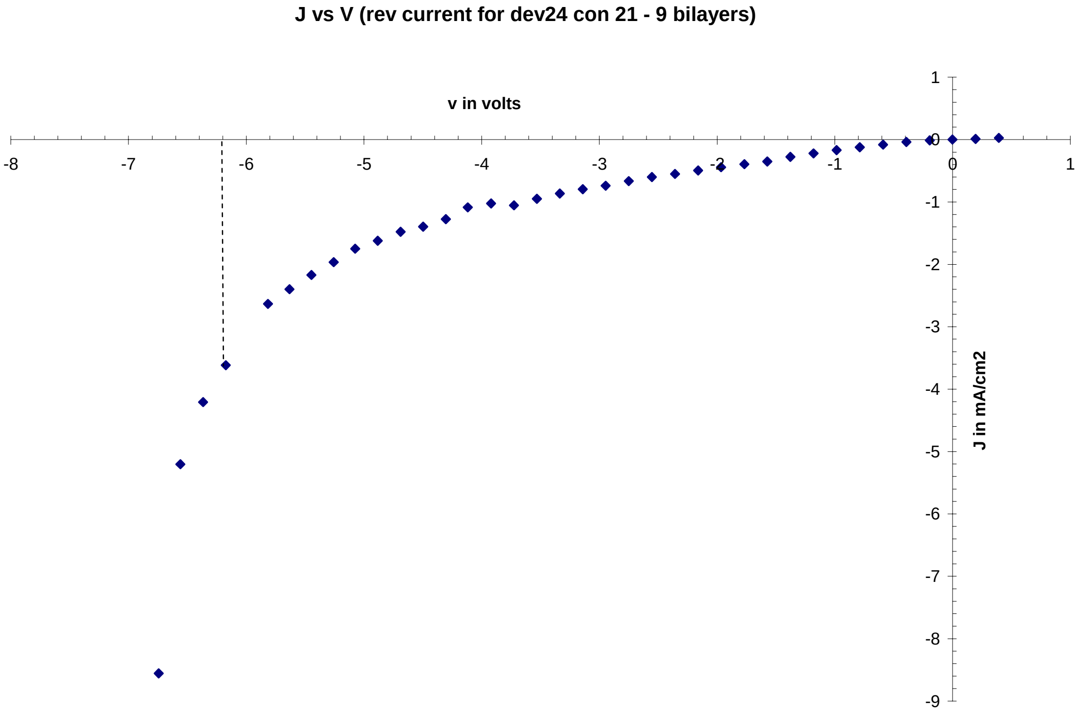

Figure 5. 10 Reverse current characteristics of ITO/PEI/(CdTe II /PDDA)*9/Al

For all of the devices the reverse current increased slowly until a certain voltage, but a steep increase was observed beyond a certain voltage. That voltage beyond which the current shoots up can be defined as the "reverse turn on voltage". The mechanism of electron transport for reverse current is explained in detail in section 5.30, the possibility of a Schottky mechanism or a tunneling mechanism is considered.

5.26 Effect of number of bilayers for reverse current

The effect of bilayers on the reverse current was studied by measuring current density vs. voltage for various devices with different number of bilayers.

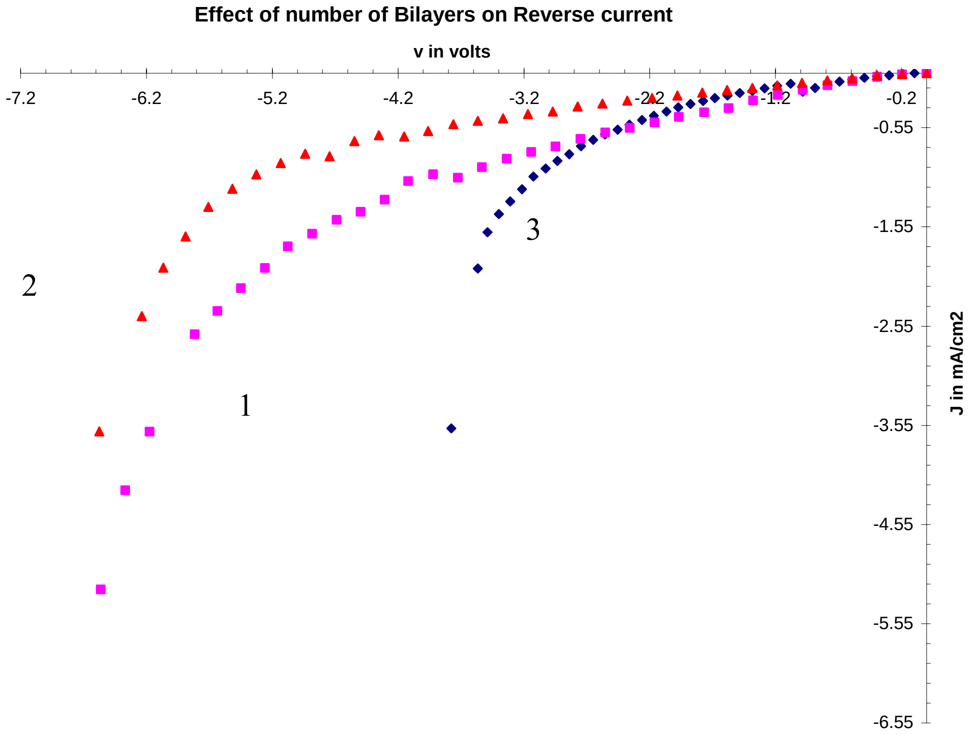

Figure 5. 11 Effect of bilayers on reverse current as function of voltage, where 1 represents a device with 9 bilayers of CdTe and PDDA, 2 with 12 bilayers of CdTe and PDDA and 3 with 23 bilayers of CdTe and PDDA

From figure 5.11 it can be seen that the device with 9 bilayers had a greater current density than a 12 bilayer device but a 23 bilayer device had a much greater current density than the 9 and 12 bilayer devices. This was very much identical to the effect of bilayers on forward current clearly indicating that the mechanism of electron transport in both directions could be the same. In order to understand the impact of bilayers on current the current was plotted as a function of electric field.

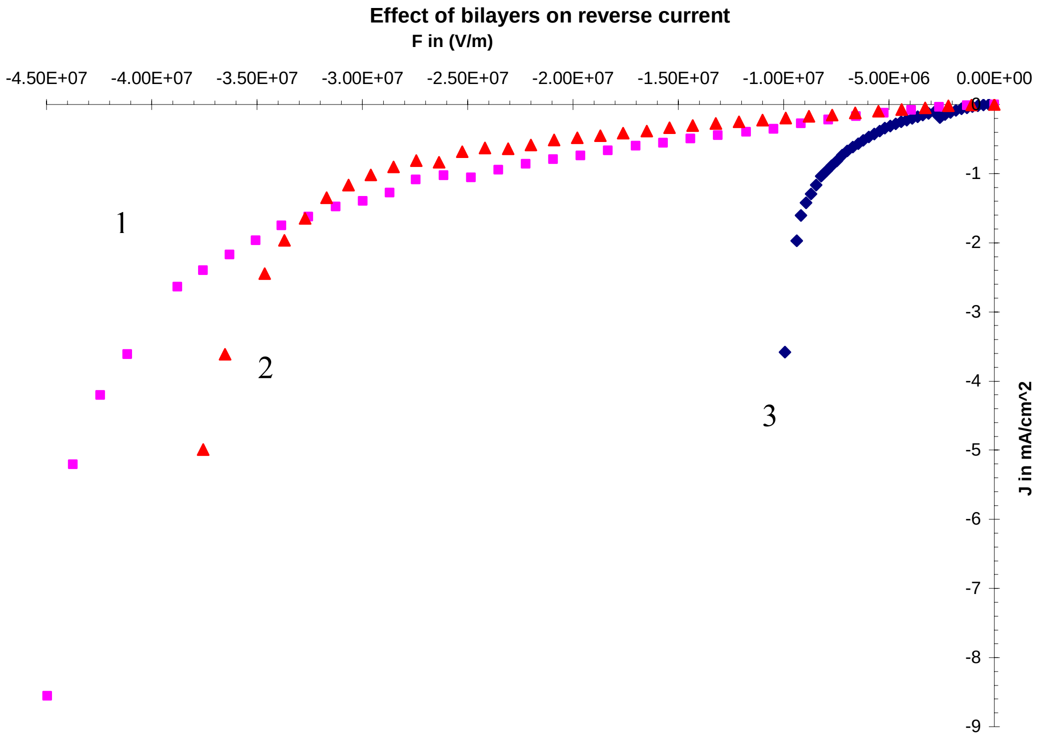

Figure 5. 12 Effect of bilayers on reverse current as function of electric field, where 1 represents a device with 9 bilayers, 2 with 12 bilayers and 3 with 23 bilayers

Identical to figure 5.7, figure 5.12 suggests that as the number of bilayers increased the current density increased, when plotted as a function of electric field. The number of bilayers and the reverse turn on field was found to be inversely proportional to each other suggesting that the barrier between the metal and the nano-particles decreased with number of bilayers. These plots suggest that a field dependent mechanism could be responsible for both forward and reverse currents.

5.27 Effect of UV Light on Reverse Current

When the UV light was incident on the device and when a reverse voltage was applied, a change in the reverse current characteristics were observed. For the same value of voltage a higher current was observed and the device reached its turn on voltage earlier.

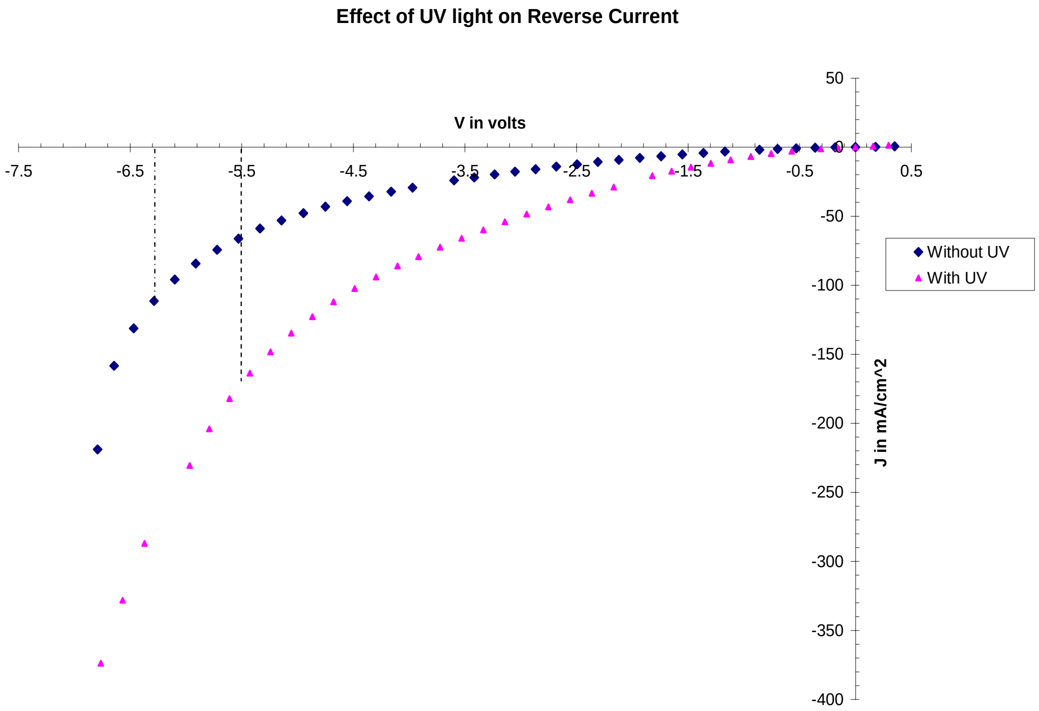

Figure 5. 13 Effect of UV light on reverse current

Figure 5.13 was identical to figure 5.9, as the current increased and the turn on voltage decreased when the UV light was incident on the device. So even in the reverse direction, the barrier between the metal and the nano-particles was lowered [48] causing a decrease in turn on voltage, thereby increasing the current. This once again proves the fact that a similar mechanism was responsible for the electron transport in both the forward and reverse directions.

5.3 Modeling the electron transport mechanism in the device

From the J-V curves discussed so far, it could be seen clearly that the device exhibited diode characteristics. The rectifying behavior could be attributed either to a Schottky conduction [42, 43], where an electric field lowers the barrier to thermal emission of electrons between the metal-semiconductor interface or a tunneling mechanism (direct or Fowler-Nordheim [44, 45]). Direct tunneling occurs when the applied voltage is lesser than the barrier height between the metal and semiconductor, while Fowler-Nordheim tunneling occurs when the applied voltage is greater than the barrier heights so that there is a triangular barrier for tunneling at the metal-semiconductor interface.

5.31 A Schottky Model for current – voltage mechanism

The initial model of the device was developed considering the fact that the organic layers were just resistive in nature and the major contributor of high currents in the device was a schottky barrier between the metal and semiconductor in both forward and reverse directions. In general a schottky contact is governed by the "ideal diode equation" given below in equation 5.1.

$$J = J_o[e^{(qV/nkT)} - 1] \text{..............................} (5.1)$$

where J_o = reverse saturation current density,

q = charge of an electron = 1.6×10^{-19} C.

k = Boltzman constant = 1.38×10^{-23} JK^{-1} and

T = Absolute Temperature in degrees Kelvin.

n = Ideality factor (practical values are usually between 1 to 3)

According to equation 5.1 for an ideal diode,

1. The diffusion (exponential part) and drift ($-J_o$) currents balance at zero bias (V=0), canceling each other and resulting in an absence of net current flow.
2. In forward bias, the barrier decreases, diffusion current increases exponentially and the drift current is unaltered.
3. In reverse bias the barrier increases, diffusion current is negligible and drift current is unaltered [46].

If the device exhibited Schottky characteristics, then the current-voltage relationship should follow the equation given in 5.1. Taking log on both sides of equation 5.1, we have

$$\ln(J) \cong \ln(J_o) + \frac{qV}{nkT} \qquad (5.2)$$

So from equation 5.2, it can be seen that ln(J) vs. V curve would be a straight line with a slope of (q/nkT) since the values of q, k and T are presumed to be known and constant. The value of the ideality factor n can be computed from the slope of the straight line. The value of n gives us a measure of the device "ideality". For an ideal diode the value of n is 1 and the slope of the ln(J) vs. V plot is q/kT. The value of n, however, deviates from 1 in real situations due to additional current generation and suppression process.

For modeling the device, the graph shown in figure 5.5 (device structure ITO/PEI/(CdTe II /PDDA)*12/Al) was considered. Figure 5.9 shows the ln(J) vs. V for the device with 12 bilayers.

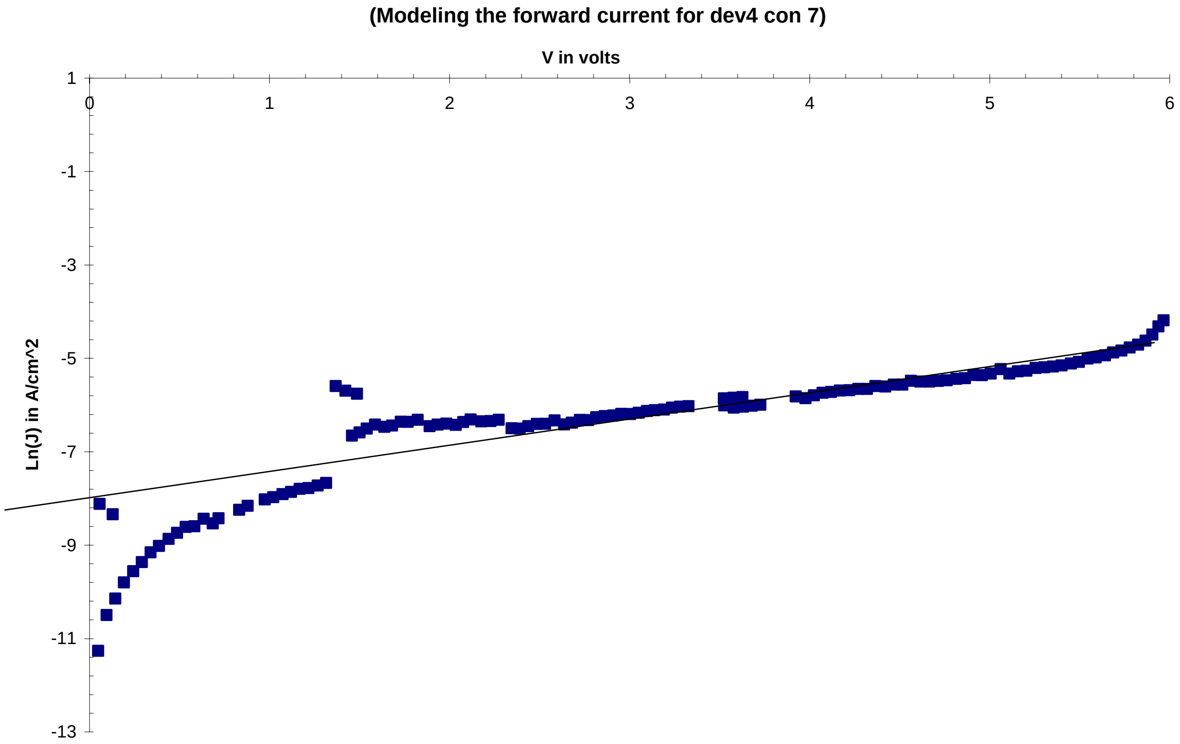

Figure 5. 14 ln(J) vs. V for device with 12 bilayers

From figure 5.14 it could be seen that the device exhibited Schottky characteristics as the ln(J) vs. V plot was linear for a wide range of voltage. The straight line intersects the Y axis at ln(J)= -8 implying when the applied voltage is zero, the log of the corresponding current density is -8. Therefore

$$\ln(J) = -8 (at V = 0V)$$

$$\Rightarrow J(at V = 0) = e^{-8}$$

$$\Rightarrow J_{o\_ITO} = 3.354x10^{-4} A/cm^{2} ....(5.3)$$

So J_{o_ITO} = 3.354 x 10^{-4} A/cm^2 (reverse saturation current density).

Now taking a point *A*, on the curve (figure 5.5), J=15.23 * 10^{-3} A /cm^2 for V = 5.966 V.

From equation (5.1) and substituting the point *A* in the equation we have

$$\Rightarrow 15.23x10^{-3} = 3.354x10^{-4}\left[\exp\left(\frac{5.966}{0.026n}\right)-1\right]\text{...(5.4)}$$

$$\Rightarrow \ln(46.408) = \left(\frac{5.966}{0.026n}\right)\text{...(5.5)}$$

$$\Rightarrow \langle n = 59.742\rangle\text{...(5.6)}$$

Therefore the ideality factor n =59.742 ≈ 60 for modeling the forward current.

So theoretical model for the forward current is

$$\Rightarrow J = 3.354x10^{-4}\left[\exp\left(\frac{V}{0.026x59.742}\right)-1\right]\text{...(5.7)}$$

Using equation (5.7) the theoretical current density was simulated and the corresponding graph for forward current was plotted and compared with the experimental values. This equation describes the possible current voltage mechanism for all 12 bilayer devices.

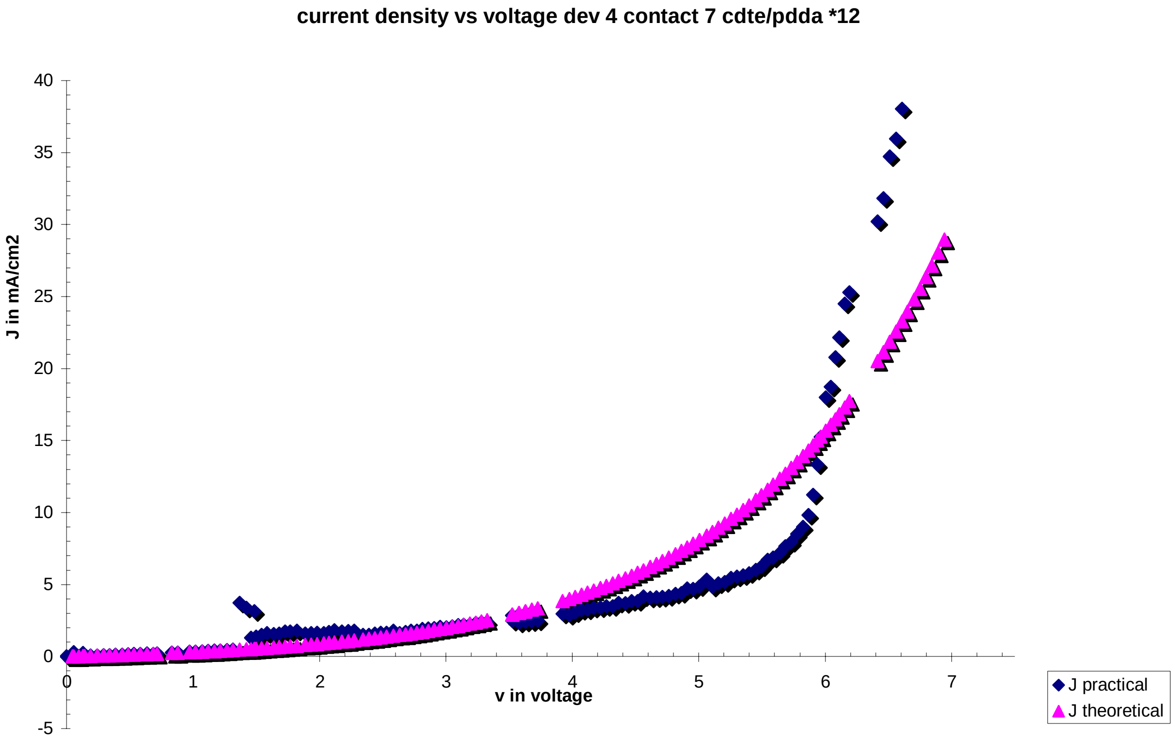

Figure 5. 15 Simulated & Experimental Current for a 12 bilayer device

From figure 5.15 it can be seen that the simulated curve closely followed the experimental curve for lower voltages but for higher voltages the experimental current density was higher than the simulated one. Also the value of ideality factor was much higher than the expected values, indicating that this model could just be used as an approximate one but not an accurate one.

As the device exhibited rectifying behavior in both directions, a Schottky model was developed for the reverse current and the simulated current density was compared with the experimental values. So a ln (J) vs. V was plotted for the reverse current and the Schottky model was developed from that graph.

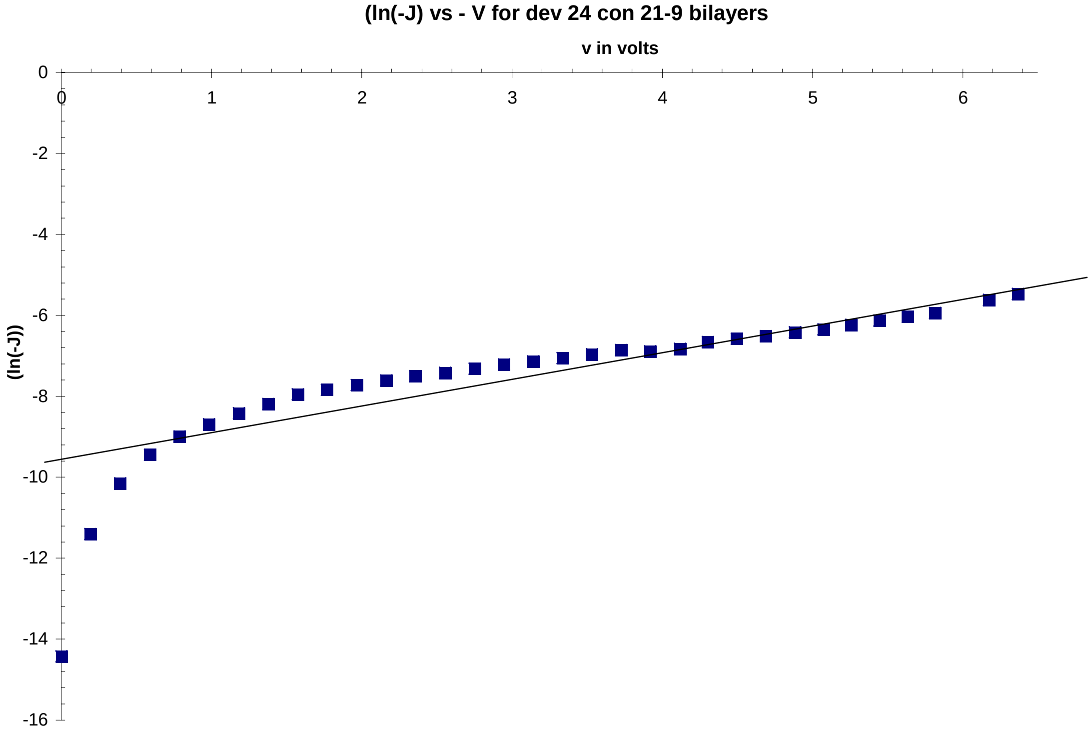

Figure 5. 16 ln (J) vs. V for Reverse current

From figure 5.16 it can be seen that the ln(J) vs. V was a straight line for the reverse current thus indicating that the Schottky model could be used for the reverse current mechanism too. From the device characteristics it can be concluded that the device exhibited Schottky mechanism in both directions, which would be possible if the nano-particles formed a Schottky diode with ITO for positive voltages and with aluminum for reverse voltages.

$$\ln(J) = -9.4 \; at \; V = 0 \Rightarrow J = e^{-9.4} = 8.272x10^{-5} \; A/cm^2 \qquad (5.8)$$

Taking one point on the curve J=3.61 mA/cm^2 for V=6.17 Vand substituting in

$$3.61x10^{-3} = 8.272x10^{-5}\left(\exp\left[\frac{6.17}{0.026n}\right]-1\right) \qquad (5.9)$$

$$n = \left(\frac{6.17}{0.026x\ln(44.6)}\right) \Rightarrow \langle n = 62.48 \rangle \qquad (5.10)$$

$$\Rightarrow J = 8.272x10^{-5}\exp\left[\left(\frac{V}{0.026x62.48}\right)-1\right]\text{..}(5.11)$$

Equation 5.11 gives the theoretical reverse current used for simulation. The simulated and the experimental values of reverse current are plotted in figure 5.11.

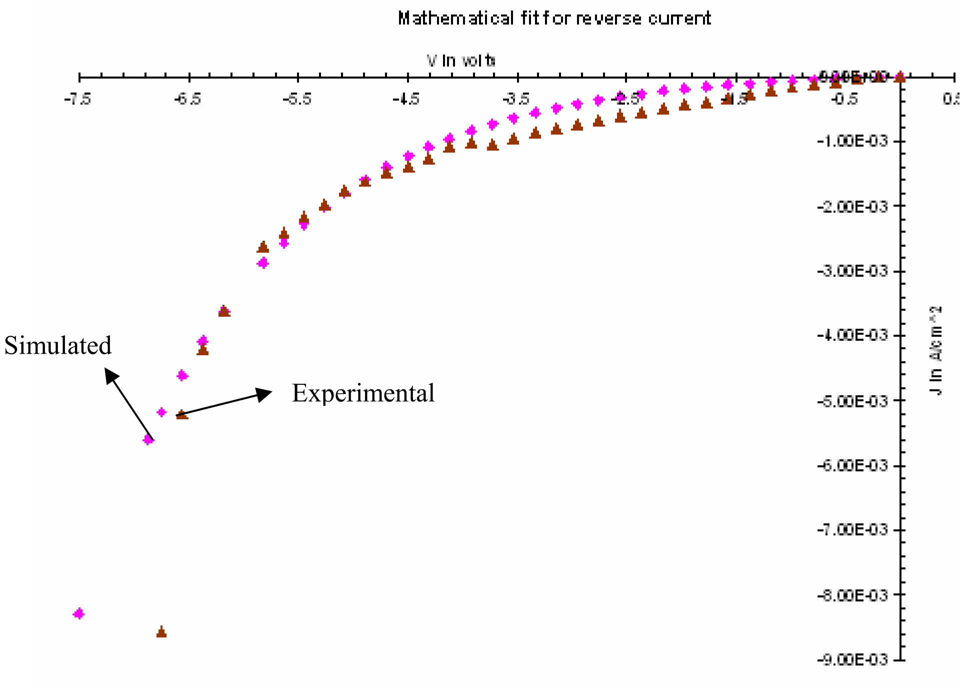

Figure 5. 17 Simulated and Experimental current density for Reverse bias.

Figure 5.17 shows that the theoretical current density followed the experimental values for lower voltages but at higher voltages the experimental values over seeded the simulated values indicating an alternate electron transport mechanism was involved in the device. Also the value of ideality factor was too high compared to the expected values. Using equation 5.11 the barrier potential between the semiconductor and the nano-particles can be calculated as follows.

5.32 Calculation of Barrier Potential from the Schottky Model

For a Schottky diode the reverse saturation current can be determined from the following equation [47],

$$J_o = R^* T^2 \exp\left(\frac{-q\Phi_B}{k_B T}\right) \qquad (5.12)$$

R^* is the Richardson constant approximated to its free electron value (120 A cm^{-2} K^{-2})

Φ_B is the barrier potential between CdTe II and the metal (Al or ITO).

From the previous section J_{o_Al}=8.272 x 10^{-5} A/cm^2 for the barrier between CdTe II and Al and J_{o_ITO} = 3.354 x 10^{-4} A/cm^2 for the barrier between CdTe II and ITO.

Equation 5.12 can be rewritten as,

$$\Rightarrow \exp\left(\frac{-q\Phi_B}{k_B T}\right) = \frac{J_o}{R^* T^2} \qquad (5.13)$$

Substituting the values for the reverse currents, we have

$$\Phi_{B\_Al} = (0.026) \times [\ln(6.38) + (-14)\ln(10)] \qquad (5.14)$$

$$\Rightarrow \Phi_{B\_Al} = 0.789eV \cong 0.79eV \qquad (5.15)$$

Thus the barrier potential between CdTe II and aluminum was found to be *0.79 eV* when the Schottky model was used. From the barrier potential the electron affinity (X) of the nano-particles were determined by using the relation

$$q\Phi_B = q(\Phi_m - \mathrm{X}) \qquad (5.16)$$

Where Φm is the metal work function [48], for aluminum the work function was *4.1 eV.*

$$\Rightarrow 0.79 = 4.1 - X$$

$$\Rightarrow X = 3.31eV \qquad (5.17)$$

So, the electron affinity of the nano-particles was calculated to be *3.31 eV*. Using equation 5.13, 5.17 and using the work function of ITO as *4.6 eV* [55], the barrier potential between the nano-particles and ITO can be calculated as follows:

$$\Phi_{B\_ITO} = (0.026) \times [\ln(31.05) + (-12)\ln(10)] \qquad (5.14)$$

$$\Rightarrow \Phi_{B\_ITO} = 0.629eV \cong 0.63eV$$

Thus the barrier between CdTe II and Al was 0.79eV while the barrier between CdTe II and ITO was determined to be 0.63eV. The expected values of barrier between ITO and CdTe II is (4.9-4.6 = 0.3eV) which is lesser than the calculated value of 0.63eV.

5.33 Validity of the Schottky model

According to the proposed model a rectifying diode is formed between CdTe II and ITO when a positive voltage is applied, while a rectifying diode is formed between CdTe II and Al when a negative voltage is applied. This model proposes a back-to-back Schottky diode which conducts in either direction, which would be possible only if there were shunt resistances present as shown in figure 5.18.

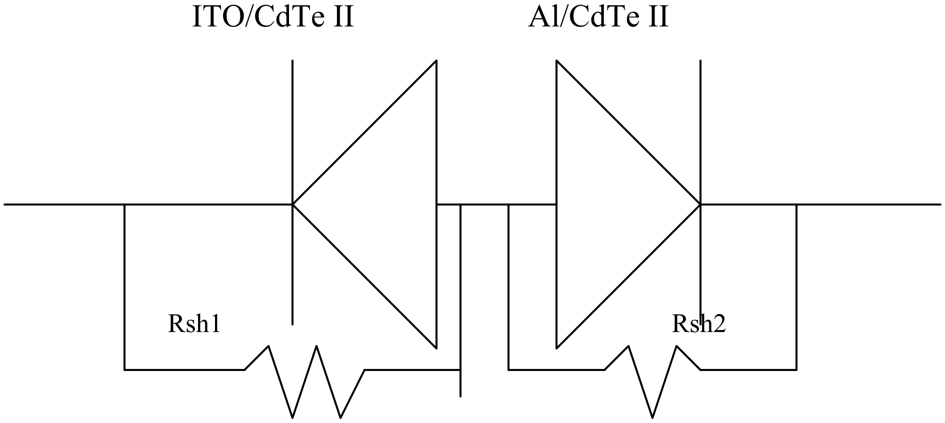

Figure 5. 18 Back-to-Back Schottky diodes with shunt resistances

5.34 Energy Band Diagram based on the Schottky model

Using the values of electron affinity of the nano-particles, work function of Al, and the calculated barrier potentials between CdTe II and Al, the energy band diagram of the contact between CdTe II and Al was drawn and is shown in figure 5.19. The energy band diagram does not show the presence of the shunt resistance which are believed to provide a path for the flow of charges from one metal to the other through the nano-particles. The Schottky contact between CdTe II and ITO could be drawn in a similar way with the corresponding values of work function and barrier potential.

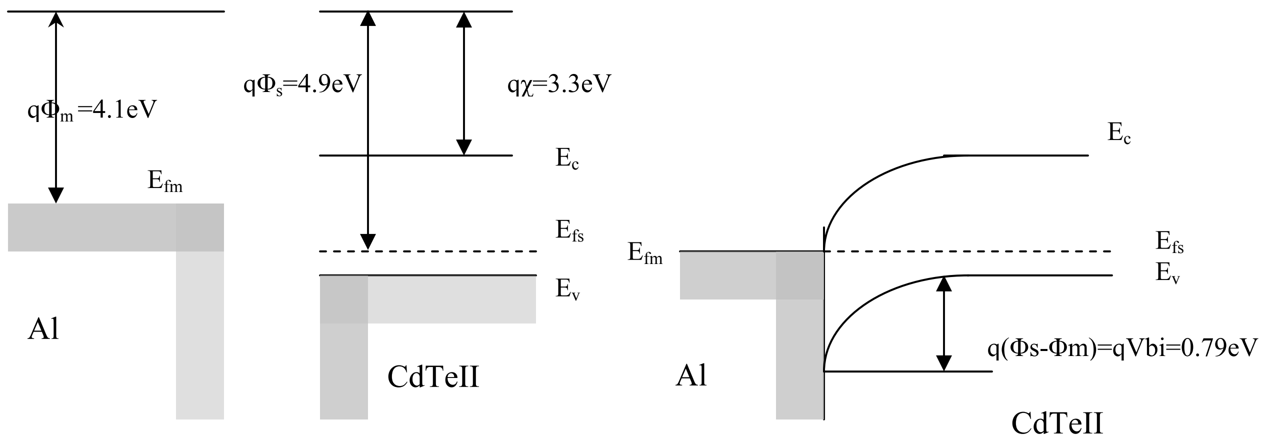

(a) **(b)**

Figure 5. 19 (a) Energy band diagram of Al and CdTeII before contact, (b) after contact at equilibrium

The barrier between ITO and CdTe II has a barrier potential of nearly 1.5 eV while that between CdTe II and Al is nearly 0.8 eV. The junction between Al and CdTe II behaves like a Schottky when a positive voltage is applied while the junction between ITO and CdTe II behaves like a Schottky when a negative voltage is applied.

5.35 Limitations of the Schottky Model

Even though the proposed Schottky model could explain the rectifying nature of the device in both directions, it had a number of limitations which compelled the need for a more elaborate and detailed model for electron transport mechanism in the device. The limitations of this model were:

1. The presence of shunt resistances though sounded feasible, a clear explanation on how it could be accounted for could not be given.
2. If the shunt resistances could be accounted by the presence of the organic polycation layers in the device then there values should be in the range of 10^3 to 10^5 ohms. But in our model the expected values of shunt resistances were in the order of 10^1 ohms.
3. The slope of the experimental current density curves was much higher than the slope of simulated current density curves for voltages greater than 5 volts.
4. The values of the ideality factor (n) were much higher than the expected values of 1 or 2, indicating another mechanism of charge transport could be taking place in the device.
5. The presence of traps which could possibly account for shoulder in currents (figure 5.5) has not been taken into account.
6. A field dependent electron transport mechanism could also be possible, (as shown figure 5.7), however more analysis had to be done to verify this.

5.36 A new Model based on "Tunneling" mechanism

This section discusses a field dependent tunneling model for the electron transport mechanism in the device. In general when a field dependent tunneling mechanism is present, the current-voltage relationship is given by equation 5.19 [48],

$$J \propto F^2 \exp\left(\frac{-\kappa}{F}\right) \ldots\ldots\ldots\ldots\ldots\ldots\ldots\ldots\ldots\ldots\ldots (5.19)$$

Where J is the current density, F is the electric field, κ is a parameter that depends on the barrier across which electron tunnels. For an injected charge tunneling through a triangular barrier at the polymer interfaces, the constant κ is given by equation 5.20,

$$\kappa = \frac{8\pi\sqrt{2m^*}\phi^{3/2}}{3qh} \ldots\ldots\ldots\ldots\ldots\ldots\ldots\ldots\ldots\ldots\ldots (5.20)$$

Where φ is the barrier height, m* is the effective mass of the electrons in the polymer, q is the elementary charge of an electron and h is the Planck's constant (4.1357x10^{-15} eV sec). On evaluating the proportionality constants and substituting, equation 5.19 can be rewritten as

$$J = a\phi^{-1}F^2 \exp\left(\frac{-b\phi^{3/2}}{F}\right) \ldots\ldots\ldots\ldots\ldots\ldots\ldots\ldots\ldots (5.21)$$

where

$$a = \frac{e^3}{4h} = 1.541 \times 10^{-6}\, AeVV^{-2}$$

$$b = \frac{8\pi\sqrt{2m^*}}{3qh} = 6.83 \times 10^{9}\, eV^{-3/2}Vm^{-1}$$

But equation 5.21 (also known as "Generalized Fowler-Nordheim Equation") is valid only under ideal circumstances [49] where the following assumptions have been taken. The metal

1. Has a free electron band structure.
2. Has electrons obeying Fermi-Dirac statistics.

3. Is at zero temperature.
4. Has a smooth flat surface.
5. Has a work function that is uniform across the emitting surface and is independent of the external electric field.
6. There is a uniform electric field outside the metal surface
7. The exchange and correlation relation interaction between the emitted electron and the surface can be neglected.
8. Barrier penetration coefficients may be evaluated using the JKWB approximation.

So when any of the assumptions mentioned above is relaxed (as observed in experimental devices) equation 5.21 is altered to,

$$J = \lambda a \phi^{-1} F^{2} \exp\left(\frac{-\mu b \phi^{3/2}}{F}\right) \text{......................................} (5.22)$$

(*also known as Forbes equation*)

Where λ and μ are generalized correction factors, whose values depend upon the assumptions and approximations made. Both λ and μ may be functions of φ, F and other quantities.

5.37 Verifying Tunneling in the device

This section discusses the possibilities of tunneling mechanism in the nano-particle/polymer device structure. If there was a tunneling mechanism present in the device then the current density vs. voltage will follow the relationship given below in equation 5.23. Taking log on both sides of equation 5.19,

$$\ln\left(\frac{J}{F^{2}}\right) \propto \left(\frac{-1}{F}\right) \text{..} (5.23)$$

So from 5.23, it can be seen that the plot of ln(J/F^2) vs. (1/F) would be a straight line with a negative slope if the device exhibited a Fowler-Nordheim tunneling mechanism for electron transport. The ln(J/F^2) vs. (1/F) for reverse and forward current density are shown below.

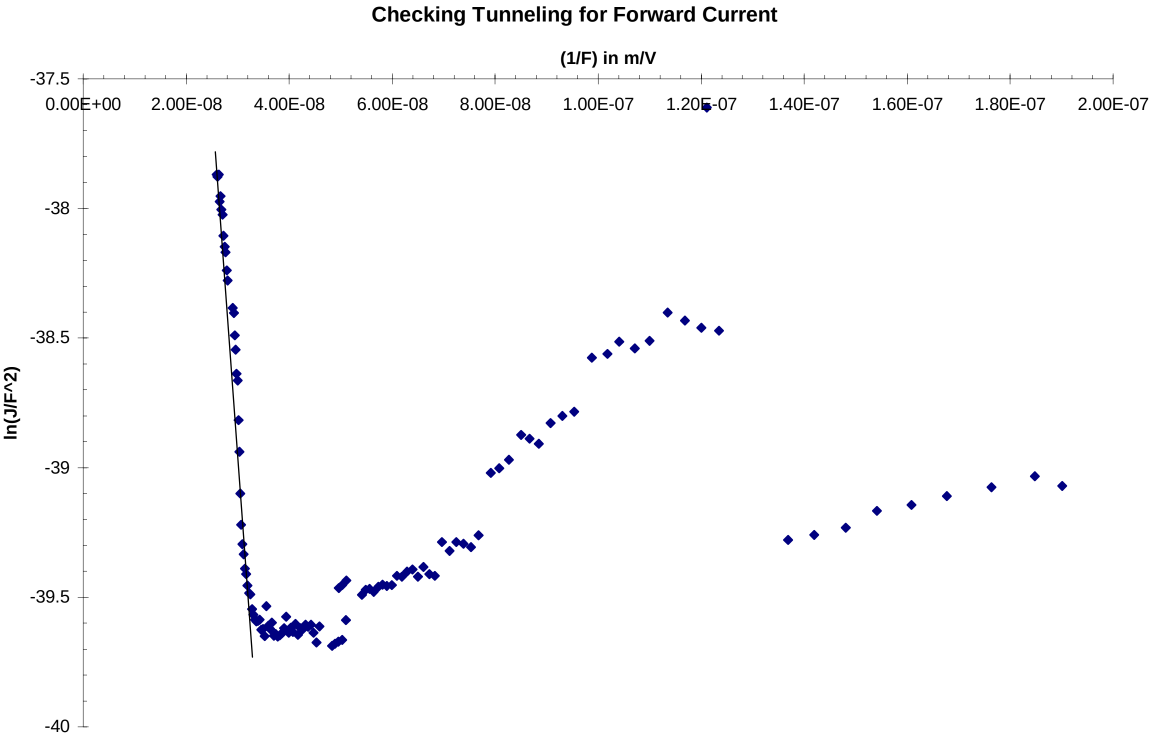

Figure 5. 20 Verifying F-N tunneling mechanism for forward current

It can be seen clearly from figure 5.20 that ln(J/F^2) vs. (1/F) was a straight line for higher electric field, while at lower fields the characteristics were not linear. This suggests that F-N (Fowler-Nordheim) tunneling mechanism could be the dominant mechanism of electron transport at higher electric fields (or consequently higher voltages) while another mechanism was prevalent at lower electric fields.

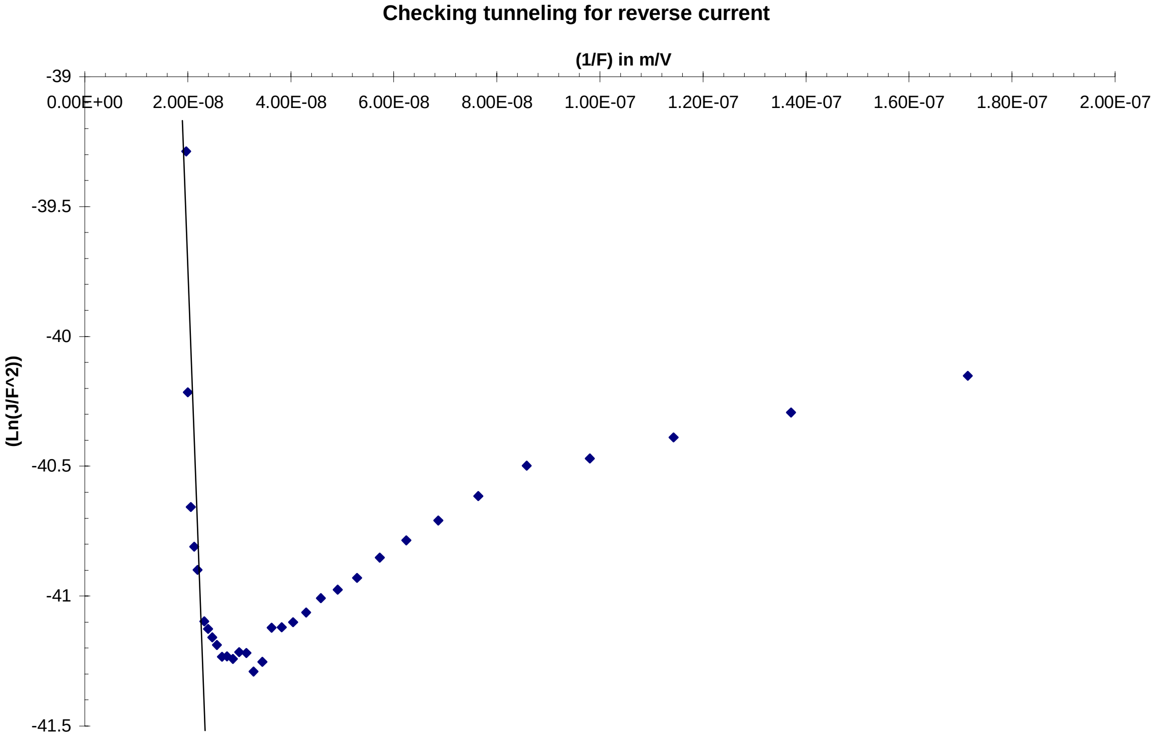

Figure 5. 21 Verifying F-N tunneling mechanism for reverse current

Figure 5.21 yielded a similar graph like 5.14, where a linear plot was observed for higher fields while at lower fields a logarithmic plot was observed. The slope of the straight line at higher fields was used for modeling the device characteristics (later in section 5.38). When the method of curve fitting was used, the plot $\ln(J/F^2)$ vs. (1/F) showed a logarithmic relationship suggesting that current density J was directly proportional to electric field F (or voltage V) indicating a resistive behavior at lower fields. Thus by using the slope and a point on the straight line in the $\ln(J/F^2)$ vs. (1/F) plot, the equation of the straight line was calculated and then the current density as a function of electric field was obtained.

5.38 Simulating the current density using the tunneling model

The equation of the forward and reverse current were evaluated as follows. For the forward current, taking two points A (2.59x10^{-8},-37.86) and B (3.049x10^{-8},-39.1) on the straight line in figure 5.14, the slope can be evaluated as,

$$m = \frac{y2 - y1}{x2 - x1} = \frac{(-39.1 - (-37.86))}{(3.049 \times 10^{-8} - (2.59 \times 10^{-8}))} = -2.7 \times 10^{8} \text{..................................}(5.24)$$

$$also\ (y - y1) = m(x - x1)$$

$$\Rightarrow (y - (-37.86)) = -2.7 \times 10^{8} (x - 2.59 \times 10^{-8})$$

$$\Rightarrow y = -2.7 \times 10^{8} x - 30.87 \text{...}(5.25)$$

$$or\ \ln\left(\frac{J}{F^2}\right) = -2.7 \times 10^{8} \left(\frac{1}{F}\right) - 30.87$$

$$or\ J = F^2 \exp\left(\frac{-2.7 \times 10^{8}}{F} - 30.87\right) \text{...}(5.26)$$

Equation 5.26 gives the tunneling current for the device during forward bias. Thus the tunneling mechanism was responsible for the rectifying nature of the device in the forward direction. From graph 5.5 it can be seen that the J-V curve was linear for voltages less than 5 volts, indicating that the device was resistive in nature. This is further confirmed from figure 5.16, where the simulated current density was plotted when tunneling alone was present and when tunneling and a resistive current were present together.

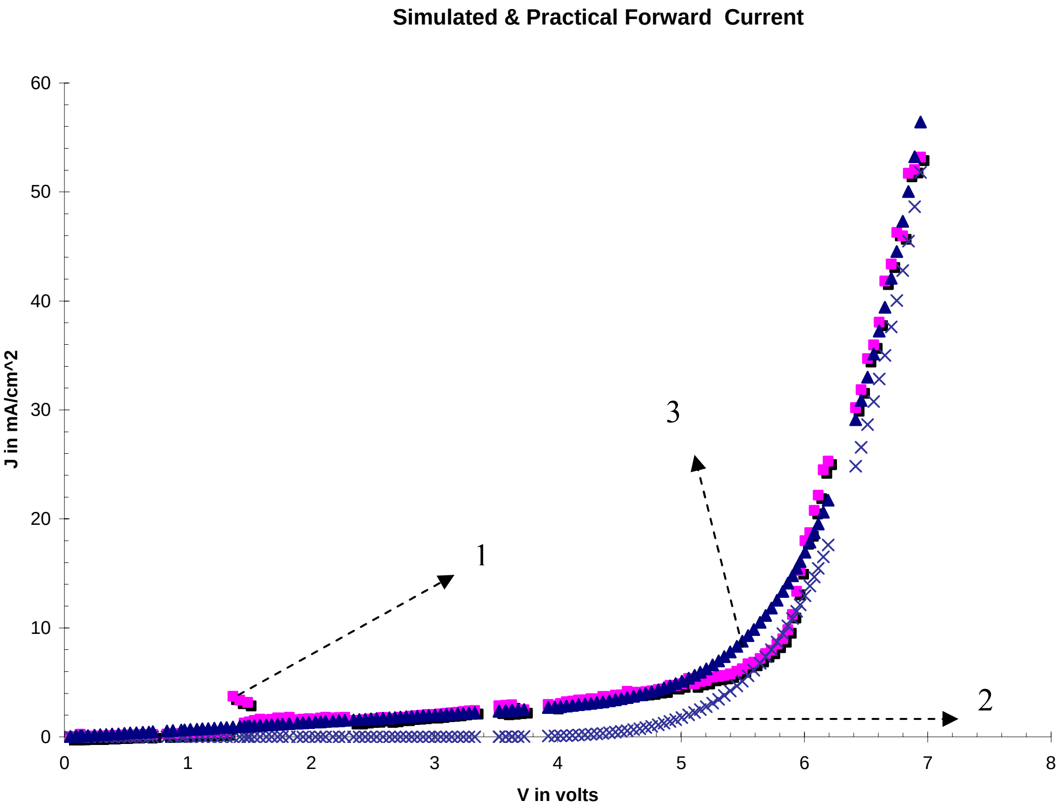

Figure 5. 22 Simulated and experimental forward current density, 1.Experimental current density 2.Tunneling component of simulated current and 3. Tunneling and resistive component of simulated current

From the figure above, it can be seen that the simulated values merges with the experimental current density for almost all the values, clearly suggesting that both the resistive and tunneling component contribute to the final current density. The final equation used for simulation of the current density in figure 5.16 was,

$$J_{fwd} = \left(\frac{1.457}{2.177 \times 10^{3}}\right)V + F^{2} \exp\left(\frac{-2.7 \times 10^{8}}{F} - 30.87\right) \qquad (5.27)$$

Using the same principle mentioned above, the tunneling component for the reverse current was evaluated. Taking two points A1 ($2.186\text{x}10^{-8}$,-40.89) and B1 ($1.965\text{x}10^{-8}$,-39.28) on the curve in figure 5.15, the slope was evaluated as,

$$m = \frac{y2 - y1}{x2 - x1} = \frac{(-39.28 - (-40.89))}{(1.965 \times 10^{-8} - (2.186 \times 10^{-8}))} = -7.285 \times 10^{8}.$$

And the equation for the tunneling component was found to be,

$$J = F^2 \exp\left(\frac{-7.285 \times 10^8}{F} - 24.97 \right) \ldots\ldots\ldots\ldots\ldots\ldots\ldots\ldots\ldots (5.28)$$

Equation 5.27 gives the tunneling current for the device during reverse bias. The sum of the tunneling component (using 5.27) a linear (resistive) component was used to determine the final simulated reverse current, given below in equation 5.28 and the plot of it is shown below in figure 5.17.

$$J = \left(\frac{1.08}{3.919 \times 10^3} \right) V + F^2 \exp\left(\frac{-7.285 \times 10^8}{F} - 24.97 \right) \ldots\ldots\ldots\ldots\ldots\ldots\ldots\ldots (5.29)$$

The first part in equation 5.29 is the resistive part which is caused due to the organic layers present in the device, while the second component is due to the electrons injected from the metal to the nano-particle by tunneling across the organic layer.

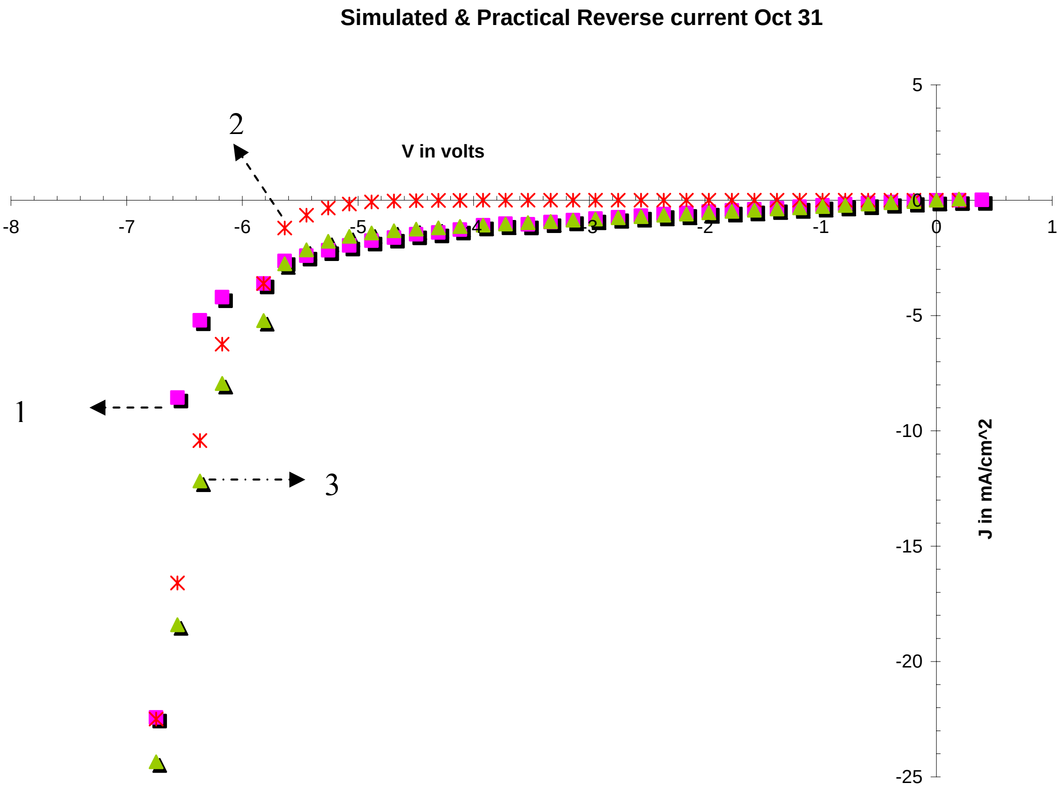

Figure 5. 23 Simulated and experimental reverse current, 1. Experimental current density 2. Tunneling component of simulated current, and 3. Tunneling and resistive component of simulated current

Similar to the forward current, it can be seen that a similar mechanism drives the reverse current too. From figure 5.23 it can be inferred that tunneling alone is not responsible for the current but a resistance offered by the organic layers also play a part in it.

Though the tunneling equations (5.26, 5.28) were determined separately for the forward and reverse current, there were some difficulties in the determination of barrier potential (Φ). Rewriting equation 5.26 in the "Forbe's equation" format we have,

$$J = F^2 \exp\left(\frac{-2.7\times10^8}{F}\right)\times\exp(-30.87)\text{....................................}(5.30)$$

comparing equation 5.30 *to Forbes equation, we have*

$$\lambda\, a\, \phi^{-1} = \exp(-30.87)$$

$$or \quad \lambda\, \phi^{-1} = \left(\frac{\exp(-30.87)}{1.541\times10^{-6}}\right)\text{...}(5.31)$$

$$and \quad -\mu\, b\, \phi^{3/2} = -2.7\times10^8$$

$$or \quad \mu\, \phi^{3/2} = \left(\frac{2.7\times10^8}{6.83\times10^9}\right)\text{...}(5.32)$$

From equations 5.31 and 5.32, it can be seen that there are 3 variables (λ, μ, and φ) but only 2 equations, making it difficult to evaluate the exact values of all the 3 variables. Thus the value of the barrier potential was assumed to be equal to 0.79 eV for forward bias and 1.49 eV for reverse bias, the values when a Schottky barrier was assumed in both directions, which was in turn used in drawing the energy band diagram of the device.

The possibility of a tunneling mechanism and Schottky mechanism coexisting were also explored and the resultant curves for forward current are shown below. The equation used for the Schottky component was obtained similar to the one discussed in section 5.31, but the maximum current was taken as 10 mA/cm^2 instead of 55 mA/cm^2 which was taken from graph 5.15, when the current was evaluated only as result of a Schottky barrier. The tunneling component was used from equation 5.26.

Thus the Schottky component was:

$$J = 3.354 \times 10^{-4}\left[\exp\left(\frac{V}{0.026 \times 51.81}\right) - 1\right] \text{..(5.33)}$$

and the tunneling component was

$$J = F^2 \exp\left(\frac{-2.7 \times 10^8}{F} - 30.87\right) \text{..} \textit{from eqn } 5.26$$

The sum of equation 5.26 and 5.33 was used to obtain the resultant current density shown below in figure 5.24.

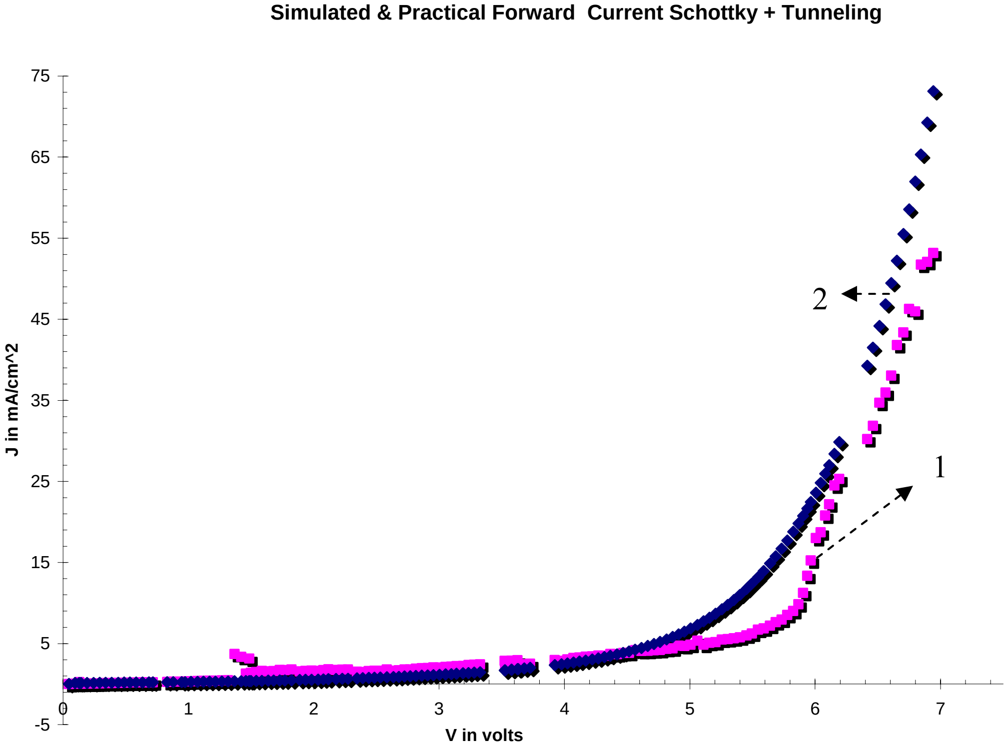

Figure 5. 24 Simulated and experimental forward current density, 1. Experimental current density and 2. Tunneling + Schottky component of simulated current

The graph above confirms the point that if the Schottky and the tunneling component were present together, then the resultant current would be much higher than the experimental values of current, unlike in ITO/MEH-PPV/Al devices where both Schottky and tunneling currents were reported [52]. A similar approach could be done for the reverse component of current and it can be proved that the sum of the simulated resistive and tunneling current would yield a closer match than the sum of simulated Schottky and tunneling component.

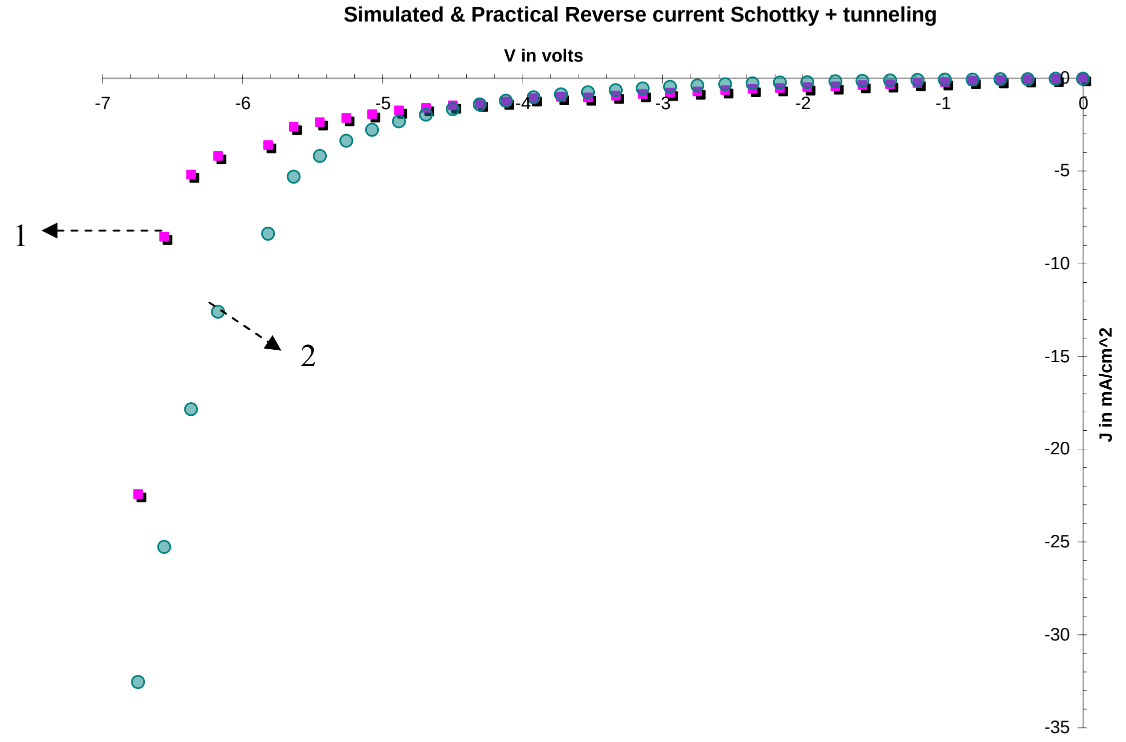

Figure 5. 25 Simulated and experimental reverse current density,

1. Experimental current density and 2. Tunneling + Schottky component of simulated current

Figure 5.25 proves that the resistive current could be a more plausible mechanism happening at lower voltages in both reverse and forward directions than a Schottky mechanism. So it can be concluded that there are two parallel paths provided by the organic polycations and the CdTe II nano-particles for electron transport in both the reverse and forward direction.

5.39 Tunneling Model -Validity

From the simulations above it can be seen that the tunneling model suggests two parallel mechanisms for current transport, one a resistive component between the metals and the organic polymers and the other a tunneling component between the nano-particles and the metals. Depending on the applied bias voltage, the tunneling takes place between CdTe II and ITO or CdTe II and Al. So this model suggests that there are two back to back Zener (tunneling) diodes with shunt resistances as shown in figure 5.26 below.

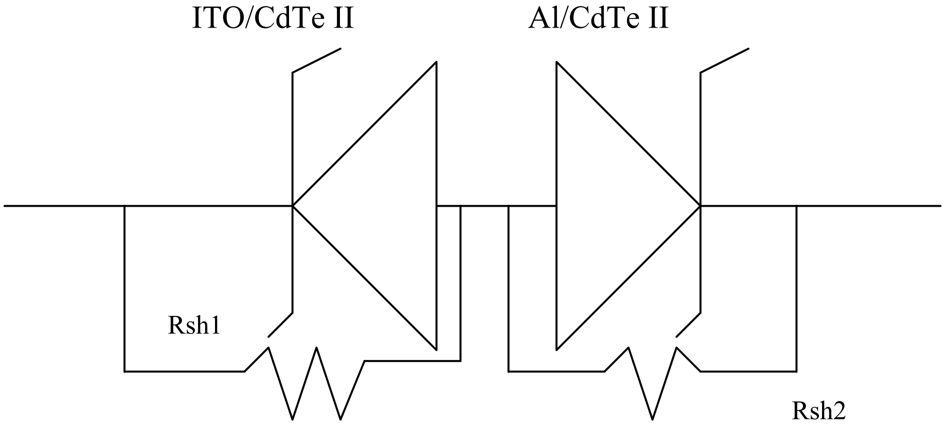

Figure 5. 26 Back-to-back Zener diodes with shunt resistances

Also the values of the shunt resistances corresponded to the values of resistances measured for the organic polymers, which were in the order of 10^3 ohms. Thus this model could clearly explain the current transport mechanism taking place in the fabricated devices.

5.40 Energy Band Diagram based on the Tunneling model

In order to draw the energy band diagram for the electron transport in the device, it should be first understood that due to the interpenetration between the nano-particles and the organic layers [54, 8] there are two separate parallel paths for current. The organic layers provide a resistive path where the resistance varies from 10^3 ohms to 10^5 ohms, depending on the concentration of the organic solution used for deposition, while the charges (electrons or holes) tunnel through the barrier between the metal and CdTe II nano-particles when the applied field is in the order of 10^7 V/m. The energy band diagram below just represents the tunneling mechanism through the nano-particles and does not show the transport of electrons through the polymer layers.

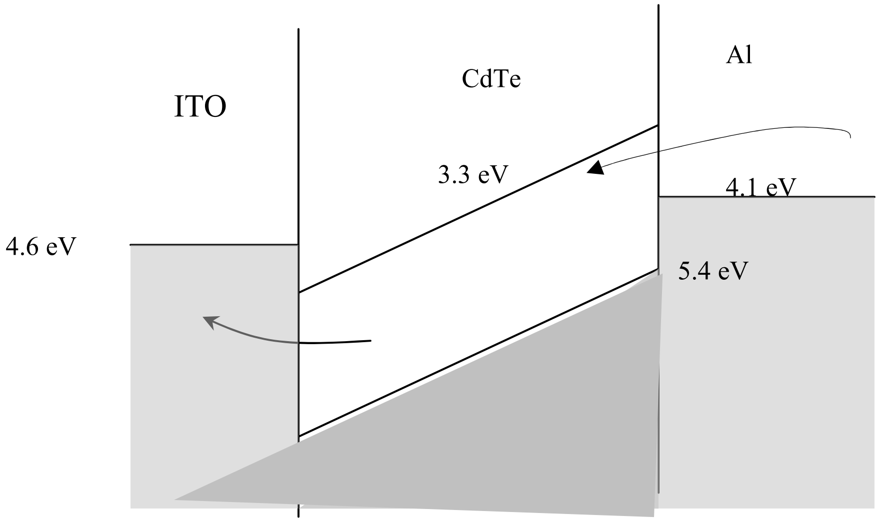

Figure 5. 267 Energy band diagram for forward voltage – tunneling model

Figure 5.27 shows electrons tunneling across the barrier between aluminum and CdTe II (p type) and to the ITO layer. Similar band diagram could be drawn for reverse bias where electrons tunnel from the ITO layer and reach the aluminum layer. This model was drawn using the tunneling model developed for ITO/MEH-PPV/Al devices [48]. It could be seen that the energy band diagram of the device shown in Figure 5.26 is significantly different from conventional tunneling diodes [55], because of the mechanism of charge transport involved within nano-particles. The nano-particles closer to the ITO electrode are at a greater positive potential than those close to Al electrode, when a positive voltage is applied across ITO. So, the nano-particles closer to the ITO electrode, have a lower electron energy level compared to those closer to the Al electrode. Also, the transfer of charges from one nano-particle to the other takes place through a hopping mechanism (field assisted ionization) [49, 51], which has not been considered here for the overall current transport in the device.

5.41 Analysis of Capacitance vs. Frequency

Figure 5.28 shows the variation of capacitance and conductance as a function of frequency for CdTe II/Polymer diodes under a forward bias of 1V.

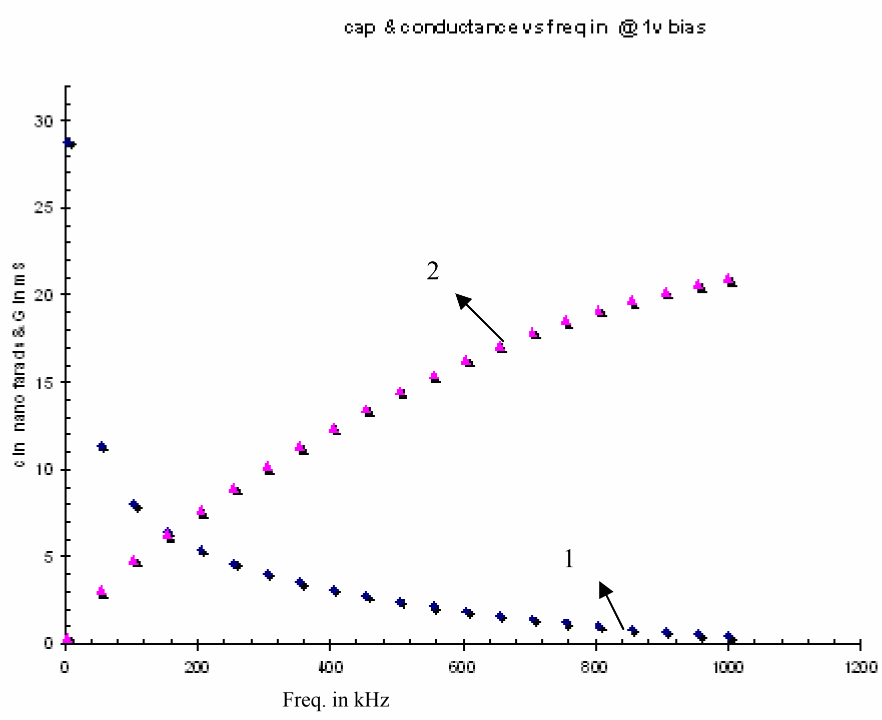

Figure 5. 27 Variation of 1. Capacitance as a function of frequency and 2. Conductance as a function of frequency

From the graph above it can be seen that capacitance (C) decays exponentially with frequency while conductance (G) rises exponentially with frequency. A theoretical model for capacitance and conductance was developed from the above graph and was modeled as:

$$C = C_o \times \exp(-2\pi f T) \text{..}(5.34)$$

$$and\ G = G_\infty \times [1 - \exp(-2\pi f T)] \text{.....................................}(5.35)$$

Where C_o= capacitance at zero frequency, G_∞ = Conductance at infinite frequency, and

T = time constant of the device.

Taking log of the capacitance and using a linear approximation model to the log curve, the values of C_o, G_∞ and T were calculated and were found to be 28.046 nF, 17.416 mS and 0.000723 s respectively for the device shown above. Therefore the capacitance and conductance as a function of frequency were evaluated as:

$$C = 28.046 \times [\exp(-2\pi f(0.000723))] \ldots\ldots\ldots\ldots\ldots\ldots\ldots\ldots\ldots\ldots\ldots (5.36)$$

$$and\ G = 17.416 \times [1 - \exp(-2\pi f(0.000723))] \ldots\ldots\ldots\ldots\ldots\ldots\ldots\ldots\ldots (5.37)$$

The resultant C vs. F and G vs. F are shown below.

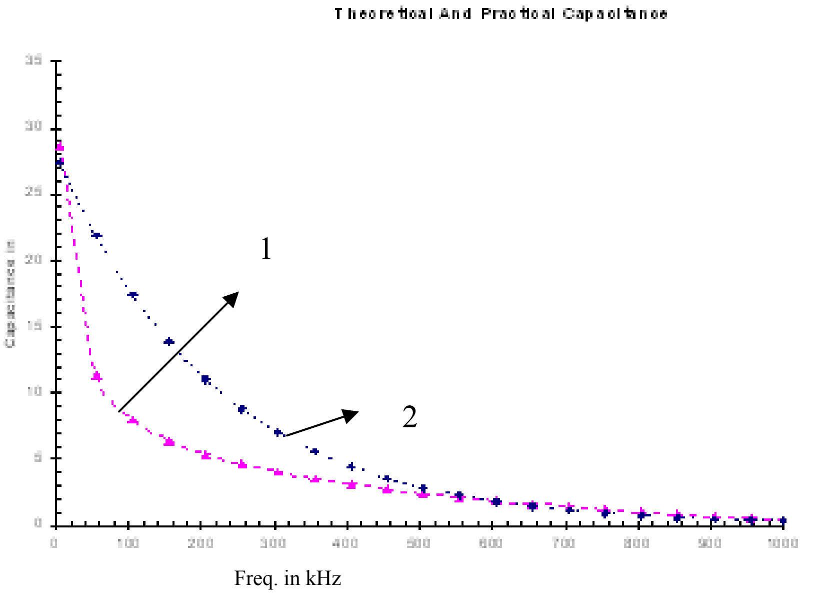

Figure 5. 289 Capacitance as a function of frequency, 1. Experimental Capacitance and 2. Simulated Capacitance

Thus from graph 5.29, it can be concluded that the exponential model can be treated as a good approximation to the variation in capacitance vs. frequency, giving an idea of the device's inbuilt capacitance.

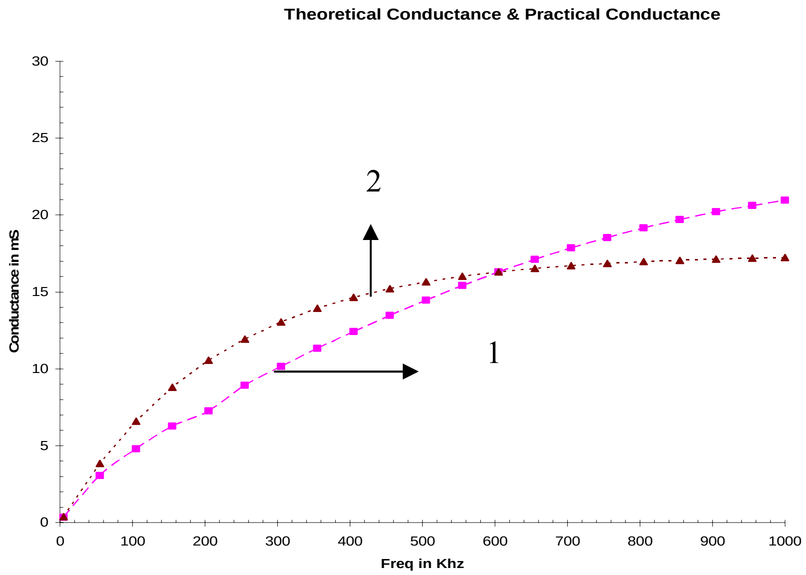

Figure 5. 29 Conductance as a function of frequency 1. Experimental and 2. Simulated

Thus it can be concluded that the theoretical model for capacitance and conductance was not totally accurate but was very useful in understanding the variation of capacitance and conductance with frequency. It can be seen in figure 5.30 that the theoretical model reached the value of G_∞ much earlier than the experimental conductance. One of the reason could be attributed to the fact that the time constant T was computed as 0.000723 s from the capacitance curve and not from the conductance curve. So the deviation in the conductance curve was slightly more than that in the capacitance curve.

5.42 Analysis of Capacitance vs. Voltage

Figure 5.31 shows the C-V measurements of CdTe/polymer devices. In general, the C-V measurements provide a good estimation of the built in potential (V_{bi}), carrier density (N_D) and depletion width (w). However the V_{bi} values calculated by C-V measurements could be unreliable sometimes due to the strong influence of the defects in the diode.

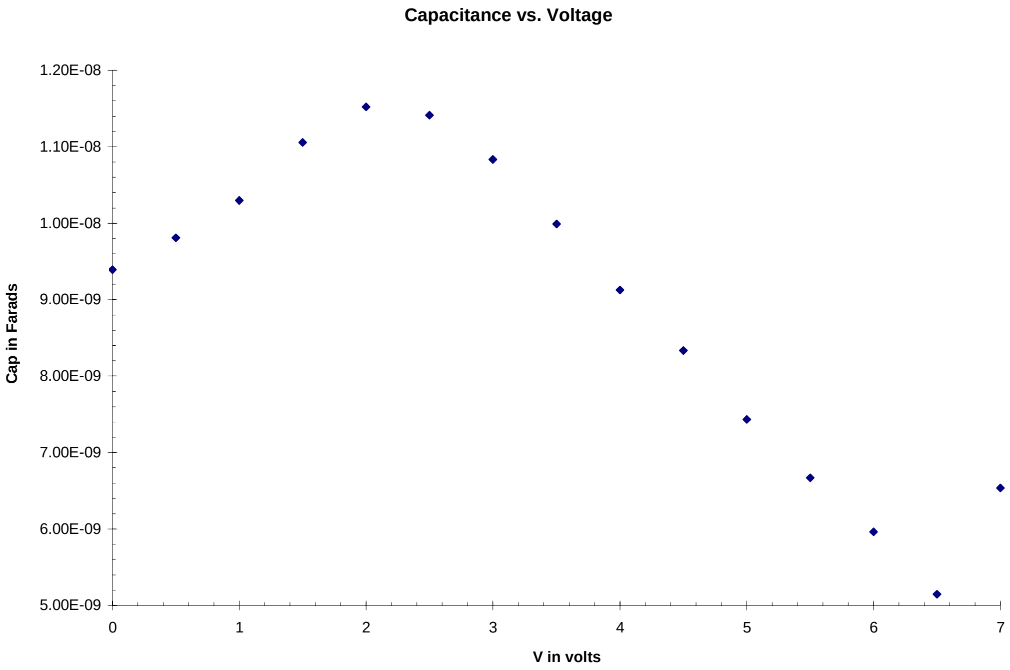

Figure 5. 30 Measured Capacitance as a function of voltage

From figure 5.31 it can be seen that the measured capacitance first increases with bias voltage then decreases as the bias voltage is increased further and significant charge injection begins. Exactly identical C vs. V was reported for ITO/MEH-PPV/Al devices by Campbell et al. [54]. The observed C vs. V curves was qualitatively different from conventional Schottky or p-n junction diodes, which could be attributed to the presence of organic polymers in the device. These devices are basically metal-insulator-semiconductor structures which makes them different from the conventional diodes. In ITO/MEH-PPV/Al devices [54] the increase in capacitance with increasing forward bias was attributed to charging defect induced trap states and/or intrinsic states in the polymer such as bipolarons, near the metal contacts. A similar treatment could be used for CdTe II/polymer devices used in this thesis. Thus the determination of built in potential (V_{bi}), doping concentration (N_D) could not be done as in the case of conventional diodes. Modeling the impedance curves requires a further understanding of the device and more experiments need to be done for that purpose as it would be an extensive project on its own. Unlike the ITO/MEH-PPV/Al devices [5.17], the conductance G for CdTe II/polymer diodes (shown below in figure 5.32) was independent of voltage, thus preventing us to use the same model for impedance as in MEH-PPV devices. Also a similar C vs. V curve was observed for reverse voltage but the mountain like appearance on the capacitance was observed at much higher voltages.

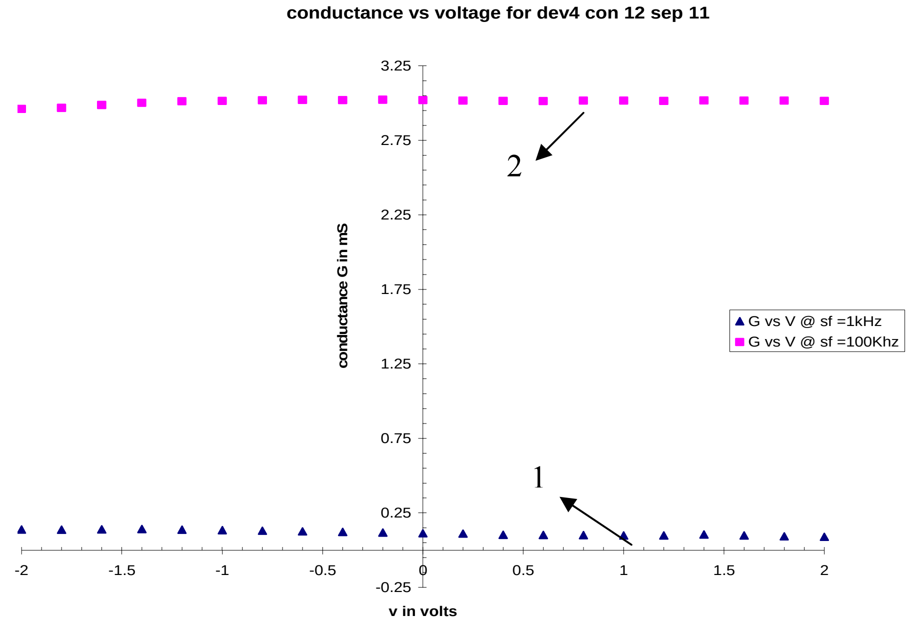

Figure 5. 31 Conductance vs. voltage at 1. 1kHz and 2. 100kHz.

The J vs. V and C vs. V characteristics reported here are typical for the devices analyzed. Of the devices fabricated about 60% were successful while the rest of them had shorts due to pinholes in the films. Some of the devices were also damaged during J-V measurements as, sometimes the probe of the multimeter used for measurements pierced the top contact making the device non functional.

6. Conclusions

Thus CdTe/polymer (CdTe II and CdTe I) thin films with thicknesses from 150 nm to 380 nm were fabricated using the method of layer-by-layer self assembly. The XRD results on the film indicated a cubic crystalline structure for the nano-CdTe II particles. From the current vs. voltage and photoluminescence measurements, it could be seen that thiol capped CdTe based diodes exhibited higher currents and photoluminescence than the uncapped CdTe diodes.

The optical absorption characteristics revealed a red shift in luminescence for the CdTe II particles in film than that of the corresponding solution. The onset of absorption for CdTe II particles in solution to be at 600 nm, while the onset was not well defined for the film (lied between 620-680 nm). The band gap of CdTe II particles were evaluated to be 2.1 eV (or λ=597 nm) for the solution and 2 eV (λ=622 nm) for the films, which was further confirmed by the PL measurements as the solution exhibited a yellow luminescence while the film exhibited orange luminescence. The red shift in luminescence was attributed to the agglomeration of nano-particles in films. The PL spectrum for the solution revealed a broad spectrum from 500-700 nm which was attributed to the presence of interfacial traps.

Thin film diodes were fabricated with a structure of (ITO/PEI/(CdTe/PDDA)*n/Al), where the number of bilayers (n) was varied from 9 to 23. The J vs. V curves revealed that the diodes exhibited rectifying behavior in both the forward and reverse biasing. The effect of number of bilayers, time, UV light on the forward and reverse currents were identical, suggesting a similar mechanism was involved in both directions. From these studies, two possible charge transport mechanism in the device were proposed. The first method involved two back-to-back Schottky diodes (between CdTe II - Al and CdTe II - ITO) with parallel resistors in the order of 10^1 ohms providing a path for the electrons when one of the diodes was off. Though this model could explain the rectifying behavior for forward and reverse voltages, the limitations of this model were that the ideality factor was in the order of 50-70 and the presence of such low parallel resistors could not be accounted for. After additional analysis, another model based on the mechanism of tunneling was devised. Through this model the current vs. voltage could be simulated accurately to four orders of magnitude. From this model it could be concluded that tunneling between the metal and the nano-particle was the predominant mechanism for charge transport, while the organic layers provided a parallel resistive path in the order of 10^3 ohms (in accordance with the value of resistances measured for organic films).

The impedance measurements as a function of frequency and voltage were also performed. The capacitance vs. frequency and conductance vs. frequency curves were modeled using an exponential rise and decay model. The capacitances vs. voltage curves were identical to that of ITO/MEH-PPV/Al devices, where tunneling was reported as the predominant mechanism for charge transport. The accurate modeling of impedance requires more analysis like the study of interfacial traps and thin oxide layers in films and could be treated as a part of future work on this project.

References:

1. Sumit Chaudhary, Mihrimah Ozkan and Warren C. W. Chan, Trilayer hybrid polymer-quantum dot light-emitting diodes, Applied Physics Letters, Vol. 84, No. 15, April 2004, 2924-2926.
2. B. O. Dabbousi, Fabrication and characterization of hybrid organic/inorganic electroluminescent devices based on CdSe nanocrystallites, PhD dissertation, MIT, Feb 1997.
3. T. Cassagneau, T. E. Mallouk, and J. H. Fendler, Layer-by-Layer Assembly of Thin Film Zener Diodes from Conducting Polymers and CdSe Nanoparticles, Journal of American Chemical Society, 1998**,** Vol. 120, 7848-7859
4. W. Chen, D. Grouquist, and J. Roark, Voltage Tunable Electroluminescence of CdTe Nanoparticle Light-Emitting Diodes, Journal of Nanoscience and Nanotechnology, Vol. 2, No. 1, 2002, 47-53.
5. Wing-Keung-Woo, Fabrication and characterization of quantum-confined optoelectronic devices based on CdSe nano-crystals, PhD dissertation, 2002.
6. Stephen A .Empedocles, Detection and spectroscopy of single CdSe nano-crystallite quantum dots, PhD dissertation, 1999.
7. A.A.Mamedov, Layer-By-Layer Assembled Thin Films of Nanocolloids, PhD dissertation, 2002.
8. N.A. Kotov, Thin Films – Polyelectrolyte Multilayers and Related Multicomposites, Wiley-VCH Verlag GmbH & Co. KGaA, Weinheim, Germany, 2003, 207-243.
9. G.Decher, Science 1997, 277, 1232-1237.
10. M.T. Crisp and N.A.Kotov Preparation of Nanoparticle Coatings on Surfaces of Complex geometry, Nano Letters, Vol. 3, No. 2, 2003, 173-177.

11. N.P. Gaponik, D.V. Talapina, A.L. Rogach, A light-emitting device based on a CdTe nanocrystal/polyaniline composite, Physical Chemistry Chemical Physics, Vol. 1, 1999, 1787-1789.
12. M.Gao, B. Richter, S. Kirstein, and H. Mohwald, Electroluminescence Studies on Self-Assembled Films of PPV and CdSe Nanoparticles, Journal of Physical Chemistry B, Vol. 102, 1998, 4096-4103.
13. S. Coe-Sullivan, W.K. Woo, J.B. Steckel, M. Bawendi, V. Bulovi, Tuning the performance of hybrid organic/inorganic quantum dot light-emitting devices, Organic Electronics, Vol. 4, 2003, 123-130.
14. W. Chen, D. Grouquist, J. Roark, Voltage Tunable Electroluminescence of CdTe Nano-particle Light Emitting Diodes, Journal of Nanoscience and Nanotechnology, Vol. 2, No. 1, 2002, 47-53.
15. L.I. Halaoui, Layer-By-Layer of Polyacrylate-Capped CdS Nanoparticles in Poly-(diallyldimetyl ammonium chloride) on Solid Surfaces, Langmuir, Vol. 17, 2001, 7130-7136.
16. T.P. Cassagneau, B. Sweryda-Krawiec, and J.H. Fendler, Rectifying Self-Assembled Ultra Thin Films, MRS Bulletin, September 2000, 40-46.
17. K. C. Sanagapalli, Electro-optical characterization and analysis of Schotkky diodes based on nano-crystalline CdS, Masters Thesis, University of Kentucky, 2004.
18. R.S. Muller, T. I. Kamins, Device Electronics for Integrated Circuits, 3rd Edition, 2003.
19. Zhiyong Tang, Ying Wang and Nicholas A. Kotov, Semiconductor Nanoparticles on Solid Substrates: Film Structure, Intermolecular Interactions and Polyelectrolyte Effects, Langmuir, 18, 2002, 7035-7040.

20. M. A. Martinez, C. Guillen, J. Herrero, Applied Surface Science, 136, 1998, 8-16.

21. R. G. Duncan, Electro-Optic Properties of Self-Assembled Non-Linear Optical Polymers, Masters Thesis, Virginia Polytechnic Institute and State University, April 30, 2002.

22. C. Lesser, M. Gao, S. Kirstein, Highly luminescent thin films from alternating deposition of CdTe nanoparticles and polycations, Materials Science and Engineering, C 8–9, 1999, 159–162.

23. A. L. Rogach, A. Kornowski, A. Eychmu1ler, H. Weller, M. Gao, S. Kirstein, and H.Mo1hwald, Strongly Photoluminescent CdTe Nanocrystals by Proper Surface Modification, Journal of Physics Chemistry B 1998, 102, 8360-8363

24. Basics of X-Ray Diffraction, Thermo ARL, ARL Applied Research Laboratories. http://www.thermo.com/com/cda/home

25. Ben G. Streetman, Sanjay Banerjee, Solid State Electronic Devices, Chapter 4, 5, 6 and 10, 5th edition.

26. Dr. Glagovich, Central Connecticut State University, http://www.chemistry.ccsu.edu/glagovich/teaching/472/uvvis/measure.html

27. The Chemistry Hypermedia Project, http://www.chem.vt.edu/chem-ed/spec/uv-vis/dualbeam.html

28. N. Gaponik, D. V. Talapin, A. L. Rogach, K. Hoppe, E. V. Shevchenko, A. Kornowski, A.Eychmulller and H. Weller, thiol capping of CdTe Nanocrystals: An alternative to organometallic synthesis, Journal of Physical Chemistry B, 106, 2002, 7177 – 7185.

29. V.P. Singh, O.M. Erickson, J.H. Chao, Analysis of contact degradation at the CdTe electrode interface in thin film CdTe-CdS solar cells, Journal of Applied Physics, Volume 78, Issue 7, October 1995, 4538-4542.
30. Ruppin, R., Optical Absorption by Excitons in Microcrystals, Journal of Physics and Chemistry of solids, Vol. 50, No. 9, pp. 877-882, 1989.
31. N.A. Kotov, Layer-by-Layer assembly of nanoparticles and nanocolloids: Intermolecular interactions, structure and Materials Perspective, Multilayer thin films: Sequential assembly of nanocomposite materials, Chapter 8, 2003, 207-243.
32. J.I. Pankove, Optical processes in semiconductors, Chapter 3, Publisher Dover: New York, 1971.
33. T.Cassagneau, J.H. Fendler, T.E. Mallouk, Optical and Electrical characterizations of thin films self-assembled from 11-Aminoundecanoic acid capped TiO2 nanoparticles and Polyallylamine Hydrochloride, Langmuir, Volume 16, 2000, pp. 241 -246.
34. J. Tauc, in F. Abeles (ed.), The optical properties of solids, North-Holland, Amsterdam, 1972, 277.
35. R. K. Sharma, Kiran Jain, and A. C. Rastogi, *Curr. Appl. Phys.* 3, 199, (2003).
36. A. L. Rogach, Nanocrystalline CdTe and CdTe(S) particles: wet chemical preparation, size-dependent optical properties and perspectives of optoelectronic applications, Materials Science and Engineering B, 69–70, 2000, 435–440.
37. A. A. Mamedov, A. Belov, M. Giersig, N. N. Mamedova, and N. A. Kotov, Nanorainbows: Graded Semiconductor Films from Quantum Dots, Journal of American Chemical Society, 2001**,** 123, 7738-7739.
38. V. P. Singh, P. Sivakumar, A. Aguilera, D. C. Morton, and E. Forsythe, An Analytical Model for Electron Transport and Luminance in SrS:Cu,Ag ACTFEL

Display Devices, IEEE Transactions on electron devices, Vol. 51, NO. 3, March 2004, 357-363

39. M. Gao, C. Lesser, S. Kirstein, H. Mo¨hwald, A. L. Rogach and H. Weller, Electroluminescence of different colors from polycation/CdTe self assembled films, Journal of Applied Physics, Vol. 87, No. 5, 2000, 2297-2232.
40. S. Mahendra, Characterization Studies on Nano-crystalline cadmium telluride (CdTe) for Applications in Optoelectronic Devices, Master's Project Report, November, 2003.
41. S. K. Mandal, A. B. Maity, J. Dutta, R. Pal, S. Chaudhuri, and A. K. Pal, phys. stat. sol. (a) 163, 433 (1997).
42. A. K. Jonscher, Electronic properties of amorphous dielectric films, Thin Solid Films, Volume 1, 1967, 213-234.
43. J. G. Simmons, Poole-Frenkel Effect and Schottky Effect in Metal-Insulator-Metal Systems**,** Physical Review**,** Volume 155, 1967, 657-660.
44. R. G. Forbes, Field Emission : New Theory for the Derivation of emission area from a Fowler-Nordheim Plot, Journal of Vacuum Science & Technology B, Vol.17, Issue.2, 1999, 526-533.
45. T. W.Hickmott, Polarization and Fowler-Nordheim tunneling in Al-AL2O3-Au diodes, Journal of Applied Physics, Vol. 87, No. 11, 2000, 7903-7912.
46. J. Todd Hastings, Chapter 16-Class Notes, EE 661: Solid State Electronics, Spring 2004,University of Kentucky, http://www.engr.uky.edu/~hastings/Courses/EE661/index.html
47. T. Cassagneau, J. H. Fendler and T. E. Mallouk, Optical and electrical characterizations of ultrathin films self-assembled from 11-Aminoundecanoic acid

capped TiO2 nanoparticles and polyallylamine hydrochloride, Langmuir, Issue 16, 2000, 241-246.

48. I. D. Parker, Carrier Tunneling and device characteristics in polymer light-emitting diodes, Journal of Applied Physics, Vol. 75, No. 3, 1994, 1656-1667.
49. R. G. Forbes, Field Emission: New theory for the derivation of emission area from a Fowler-Nordheim plot, Issue 17, No. 2, Mar 1999, 526-534.
50. B. O. Dabbousi, Fabrication and Characterization of hybrid organic/inorganic electroluminescent devices based on cadmium selenide nanocrystallites, PhD dissertation, M.I.T, June 1997.
51. N. A. Kotov, Private communication.
52. I. H. Campbell, P. S. Davis, D. L. Smith, N. N. Barashkov, and J. P. Ferraris, The Schottky energy barrier dependence of charge injection in organic light-emitting diodes, Applied Physics Letters, Vol. 72, No. 15, April 1998, 1863-1865.
53. J. W. Ostrander, A. A. Mamedov, and N. A. Kotov, Two Modes of linear Layer-by-Layer growth of nanoparticle-polylectrolyte multilayers and different interactions in the Layer-by-layer Deposition, Journal of American Chemical Society, 2001**,** 123, 1101-1110
54. I. H. Campbell, D. L. Smith, and J. P. Ferraris, Electrical impedance measurements of polymer light-emitting diodes, Applied Physics Letters, Vol. 66, Issue 22, 1995, 3030-3032.
55. B. Wessling, Progress in Science and Technology of Polyaniline and Poly-ethylenedioxythiophene, http://www2.ormecon.de/Research/ICSM2002/vortrag_wessling.htm.

Vita

Vignesh Ramachandran was born in Chennai, Tamil Nadu, India on December 25, 1979. He received his Bachelor of Engineering degree in Electronics and Communications in 2001 from the University of Madras. He worked as a Research Assistant from 2002 - 2004 in the Electronic Devices Research Group at the University of Kentucky, Lexington, Kentucky, USA.

(Vignesh Ramachandran)